Multiscale Modeling and Uncertainty Quantification of Multiphase Flow and Mass Transfer Processes

Adam Armido Donato

Dissertation submitted to the Faculty of the
Virginia Polytechnic Institute and State University
in partial fulfillment of the requirements for the degree of

Doctor of Philosophy
In
Mechanical Engineering

Ranga Pitchumani, Chair
Scott T. Huxtable
Srinath V. Ekkad
Danesh K. Tafti
Luke E. K. Achenie

December 4, 2014
Blacksburg, Virginia

Multiphase Transport Phenomena, Adsorption Separation, Multiscale Modeling,
Molecular Modeling, Uncertainty Quantification

Multiscale Modeling and Uncertainty Quantification of Multiphase Flow and Mass Transfer Processes

Adam Armido Donato

Abstract

Most engineering systems have some degree of uncertainty in their input and operating parameters. The interaction of these parameters leads to the uncertain nature of the system performance and outputs. In order to quantify this uncertainty in a computational model, it is necessary to include the full range of uncertainty in the model. Currently, there are two major technical barriers to achieving this: (1) in many situations—particularly those involving multiscale phenomena—the stochastic nature of input parameters is not well defined, and is usually approximated by limited experimental data or heuristics; (2) incorporating the full range of uncertainty across all uncertain input and operating parameters via conventional techniques often results in an inordinate number of computational scenarios to be performed, thereby limiting uncertainty analysis to simple or approximate computational models.

This first objective is addressed through combining molecular and macroscale modeling where the molecular modeling is used to quantify the stochastic distribution of parameters that are typically approximated. Specifically, an adsorption separation process is used to demonstrate this computational technique. In this demonstration, stochastic molecular modeling results are validated against a diverse range of experimental data sets. The stochastic molecular-level results are then shown to have a significant role on the macro-scale performance of adsorption systems.

The second portion of this research is focused on reducing the computational burden of performing an uncertainty analysis on practical engineering systems. The state of the art for uncertainty analysis relies on the construction of a meta-model (also known as a surrogate model or reduced order model) which can then be sampled stochastically at a relatively minimal computational burden. Unfortunately these meta-models can be very computationally expensive to construct, and the complexity of construction can scale exponentially with the number of relevant uncertain input parameters. In an effort to dramatically reduce this effort, a novel methodology—QUICKER (Quantifying Uncertainty In Computational Knowledge Engineering Rapidly)—has been developed. Instead of building a meta-model, QUICKER focuses exclusively on the output distributions, which are always one-dimensional. By focusing on one-dimensional

distributions instead of the multiple dimensions analyzed via meta-models, QUICKER is able to handle systems with far more uncertain inputs.

Acknowledgements

I could not have performed the research included in this dissertation without the support and guidance from mentors and advisors. For his advising, I would like to thank Dr. Pitchumani. Both Dr. Gel and Dr. Shahnam from the NETL, have provided endless guidance and support in the development of QUICKER. Dr. Huxtable has gone well above and beyond his role on my committee and supported me as a mentor in both my research and teaching. To the rest of my committee, Dr. Tafti, Dr. Ekkad, and Dr. Achenie, I would like to also thank them for their support in this process.

I could not have persevered through graduate school without the support of my friends and family. With my wife, I have often joked that her effort should earn her an honorary engineering degree, and having her at my side through all of this has been invaluable. For the rest of my family, their support—although sometimes a bit blunt—has helped push me through to the finish line. And through all of this, I have appreciated the support and encouragement of my friends and my co-founders at Card Isle.

Lastly, I would like to acknowledge the support from the Department of Education and the National Energy Technology Laboratory for funding my research.

Table of Contents

List of Figures

List of Tables

Chapter 1: Introduction

This dissertation addresses several fundamental issues pertaining to the computational modeling of uncertainty in engineering systems, specifically as they relate to the modeling of multiscale phenomena in adsorption separation processes. In practice, uncertainty is inherent in engineering systems, but in deterministic computational models of these systems, the uncertainty must be explicitly included. The inclusion of uncertainty brings with it two primary challenges: (1) it is necessary to quantify the specific nature of the uncertainty in the system inputs or operating parameters, and this information is often limited or unknown; (2) it is necessary to account for the full range of possible uncertainty across all uncertain dimensions, but this is often too computationally expensive to perform for practical scenarios. In addition to addressing these two challenges of uncertainty quantification, (3) this dissertation also advances the state of the art for multiscale adsorption modeling by explicitly including the turbulent regions of fixed bed reactors.

This first challenge has been categorized as epistemic uncertainty in the uncertainty analysis literature. Aleatory uncertainty can be described via some stochastic distribution, but epistemic uncertainty—in contrast—is at least partially unknown. The majority of the literature on epistemic uncertainty is focused on how to utilize limited information, or combine conflicting information. In contrast to this conventional approach, this dissertation seeks to reduce epistemic uncertainty to aleatory uncertainty for the class of scenarios where the uncertainty arises from chemical properties. By relying on multiscale modeling, where molecular-level results drive macro-scale simulations, it is possible to include the uncertainty from its source. Specifically in this dissertation, adsorption separation processes are used to demonstrate this methodology.

The second challenge in uncertainty quantification is analyzing the entire range of possible input parameters. For many practical engineering systems, the computational models can take days or weeks to run, and there may be tens or hundreds of uncertain input parameters. For a naïve approach, relying on a full factorial analysis, the number of times that the computational model must be run grows exponentially with the number of uncertain input parameters. The conventional approach, of building a meta-model from the computational model, is substantially faster, but is still intractable for most practical systems. Although meta-models do not requires the full range of samples necessary for a full factorial analysis, the number of samples necessary for a meta-model construction still scales very poorly with the number of uncertain input parameters. This dissertation presents a novel approach—QUICKER—to uncertainty analysis that scales far more efficiently than conventional approaches. Instead of

attempting to create an approximate model that has a dimensionality equal to the number of uncertain input parameters, QUICKER only approximates the output distribution, which is always one-dimensional. By solving a simpler problem, it is possible to perform an uncertainty analysis with far fewer sample points, and far less computational burden.

The third challenge, that of including the turbulent regions of adsorption reactors, must be addressed before the multiscale uncertainty aspect of this dissertation can be explored. The conventional approach to modeling adsorption reactors is to focus exclusively on the adsorbent region and assume plug flow. In practice, there are concerns with jetting and underutilization of the column, and these effects are due to the sections of the columns preceding the adsorbent region. In the following chapter, these effects are analyzed and column geometries optimized to maximize bed performance and minimize pressure drop.

1.1 Basic and Applied Contributions

The primary fundamental contributions of this dissertation are towards improving the accuracy and speed of uncertainty analysis. (1) By performing a multiscale analysis an adsorption separation process, it has been demonstrated that epistemic uncertainty can be reduced to aleatory uncertainty by using molecular modeling results to drive macro scale modeling efforts. (2) By developing a novel means of combining and analyzing the impact of uncertain inputs (i.e. focusing exclusively on the one-dimensional output distribution), the computational burden for uncertainty analysis has been drastically reduced.

The secondary fundamental contribution of this dissertation was necessary to perform the multiscale analysis in an efficient manner. (3) The bed geometry of adsorption separation reactors was optimized to maximize bed utilization and minimize pressure drop.

Chapter 2: Analysis of Pressure Drop and Utilization of Axial and Radial Fixed Bed Reactors

Fixed bed reactors are found in a wide range of industrial applications, due to their ability to provide significant surface interaction between a fixed solid (e.g. an adsorbent or catalyst) and a working fluid. This paper investigates a range of axial- and radial-flow bed geometries on the resulting pressure drop across the bed, the bed utilization and throughput. Based on the studies, optimum bed diameter values are determined for different geometries, as a function of the mass flow rate.

2.1 Introduction

Fixed bed reactors are used to increase surface interaction between a fixed solid with high surface area (e.g. an adsorbent or catalyst) and a working fluid. Applications of these reactors are diverse, including separators, chemical reactors, heat exchangers, adsorptive storage, and nuclear reactors [1]. Design of reactors for these applications requires a careful balance among three competing considerations: (1) reducing pressure drop across the reactor, and (2) increasing bed utilization. The three considerations are highly interdependent (e.g. an increase in flowrate will result in an increase in pressure drop), and the focus of this paper is on exploring the tradeoffs among these considerations for axial- and radial-flow fixed bed reactors.

The majority of fixed bed reactors in industrial applications are axial-flow reactors, where a working fluid flows axially through a bed of solid reactant, as shown in Figure 1. Due to their widespread application, there is a plethora of experimental analyses [2-8], computational studies [9-12], and textbooks [13-15] that are focused on axial reactors.

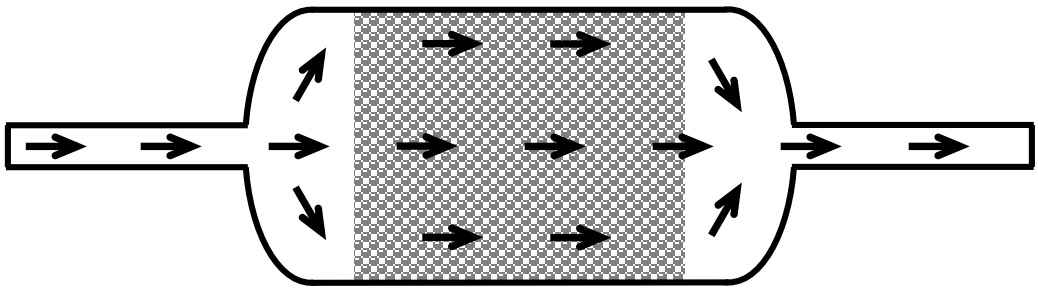

Figure 1: Schematic of axial-flow fixed bed reactor.

In spite of the wide range of work on axial fixed bed reactors, there is limited attention to the how the bed geometry—specifically the open expansions and contractions bounding the adsorbent region of the flow—affects interactions between pressure drop and bed utilization, and

how the bed design can be optimized with regard to these considerations for the different operating conditions. Pesansky et al. [8] performed an experimental parametric study on the effect of various substrate designs on the pressure drop across a commercially available catalytic converter under specified loads. By relying on a commercial product, this experimental analysis inherently accounts for the effects of practical bed geometries. The other experimental works referenced here—representative of more typical experimental work in the field—are focused on isolating the effects of the adsorbent region and mitigating the effects of the bed geometry. In order to achieve this isolation, these experimental columns have length to diameter ratios ranging from 11.4 to 35.1. This emphasis on the adsorbent region is also common in the computational realm. Zheng et al. [12], one of the few computational analyses addressing the open regions, developed a computational model that incorporated pressure drop across an axial bed for laminar flow scenarios, but all other computational studies referenced here are focused exclusively on the adsorbent region.

In contrast to axial-flow reactors there is far less published work regarding radial-flow reactors, shown schematically in Figure 2, in which the gaseous flow is primarily in the radial direction across the porous adsorbent bed. One of the primary motivations to utilize a radial reactor in place of axial reactors is the potential to reduce pressure drop and improve bed utilization [16], and accordingly much of the published literature has been in this regard. The work on radial fixed bed reactors includes comparing various flow configurations [16], analyzing multi-layered radial beds [17, 18], and tapering the bed in an attempt to improve performance [19]. Of this work, only Singh [19] accounted for turbulence in the open regions of the reactor and reactivity of the given solid. Singh's model assumes an isothermal flow and an idealized bed geometry.

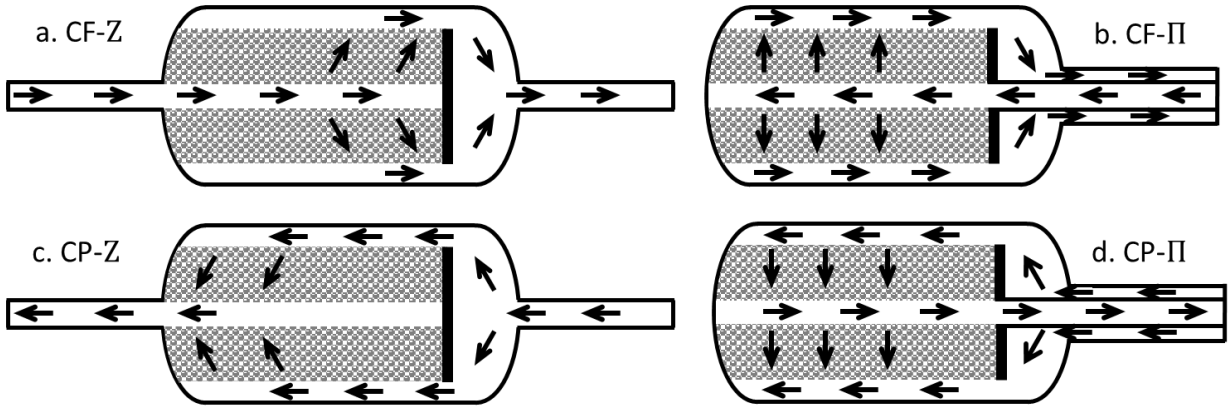

Figure 2: Schematic of different radial-flow fixed bed reactors.

This paper builds off of the previous work on systematically examining the performance of fixed bed reactors. Both axial- and radial-flow reactors are analyzed considering axisymmetric, turbulent flow conditions that are described using the re-normalization group (RNG) turbulence model. The reaction kinetics, using adsorption as a representative reaction, is simulated via a nonadiabatic, nonisothermal, bidispersed, linear driving force reaction model. A systematic parametric study of multiple axial and radial fixed bed reactors is performed to understand the effects of the reactor geometry and mas flow rate on the pressure drop and bed utilization. Based on the studies, optimum bed geometry is determined in terms of the mass flow rate.

The paper is organized as follows: the computational model is presented in Section 2, and includes the details of the axial and radial modeling. Section 3 presents a validation of the computational model, and discusses results of the parametric analysis. Section 4 concludes the paper and includes a description of which flow configuration will work best in different situations.

2.2 Computational Modeling

Two different flow arrangements have been analyzed: axial-flow reactors, as shown in Figure 1, and radial-flow reactors, as illustrated in Figure 2. For each of these configurations, the reactors are divided into two regions: one comprising of the porous, reactive solid, and the other as the open inlet and outlet on either side of the porous solid. The region with the solid is modeled as a reactive, laminar, porous region, and the open spaces are simulated via the re-normalization group (RNG) turbulence model.

When parametrically modeling the axial reactors, the bed radius and length is varied so that the volume of the reactive region remains constant (e.g. in a configuration with a larger radius, the overall bed length will be shorter). The geometry for the open regions follows the industrial standard of relying on a 2:1 elliptical dished tank-head to provide a more accurate representation of the flow within this region, and all of the bed diameters follow standard schedule 40 pipe dimensions.

The radial flow reactors have been divided into four different flow configurations based on the flow path of the working fluid. Centrifugal (CF) flow is used to describe flow that moves outwards radially—as is shown in Figure 2a and b--and centripetal (CP) flow is used to describe flow that moves inward—as in Figure 2c and d. The "Z" configuration has the exit flow moving in the same direction as the inlet flow—as in Figure 2a and c--and the "Π" configuration has the exit flow moving in the same direction as the inlet flow—as in Figure 2b and d. While parametrically varying the geometry of the radial bed, the volume of the reactive region is held constant at the same volume as is used in the axial scenarios.

The reactive region is modeled as a laminar, two-dimensional, nonadiabatic, nonisothermal, bidispered, linear driving force adsorptive system. Specifically, a mixture of propylene and nitrogen flowing through a bed of Zeolite 13X, where propylene is adsorbed and nitrogen passes through. The flow is assumed to be laminar based off of the low Reynolds number of the flow through the porous medium, assumed to be two-dimensional based off of axisymmetric geometry of the cylindrical bed, assumed to be nonadiabatic on account of external heat transfer from the wall of the reactor, nonisothermal because adsorption is an exothermic process [14], bidispersed because zeolite pellets are composed of a diffusive, non-reactive binder and adsorptive zeolite crystals [14], and the linear driving force assumption is used because it has been shown to accurately model adsorption in fixed beds while providing significant computational savings [15]. It is also assumed that the gases behave as ideal gases, and the solid and gas phases are in thermal equilibrium. The specific formulation of the model used for the reactive region is provided in Table 1, the initial and boundary conditions are provide in Table 2, and the specific parameters used in this demonstration are provided in Table 3. Within this region, the "active" gas is the gas that is more strongly adsorbed (e.g. propylene in this paper) and the carrier gas is the unadsorbed (e.g. nitrogen in this paper).

The active gas can exist in three distinct phases—bulk phase when it is outside of the adsorbent, interphase phase when it is inside the zeolite pellet but not adsorbed, and adsorbed phase while it is adsorbed—but the carrier gas is always in the bulk phase. Outside of any zeolite pellet the active gas is mixed with the carrier gas in the bulk phase, and within the bulk phase, the gases are modeled as flowing through a porous medium, with pressure drop modeled via the Ergun equation and a source term in the bulk continuity equation that represents the transport of the active gas from the bulk phase into the intrapellet phase. Since zeolite pellets are a composite of adsorptive zeolite crystals held together by an inert, structural, porous binder, the active gas must first diffuse through the inert binder before it can adsorb on the zeolite crystals. While diffusing through the inert binder to the crystals, the active gas is in the intrapellet phase. Once the active gas has diffused through the binder—the intrapellet phase—it then adsorbs onto the zeolite crystals. While in this adsorbed phase, the maximum loading of active gas on the adsorbent is determined by the isotherm model. It should be noted that the active gas can also move from the adsorbed phase to the intrapellet phase and then to the bulk phase; the rate and direction of movement of the active gas is determined by the linear driving force equations. Finally, adsorption is an exothermic reaction, and the final equation describes the energy transport of the reactive region.

Table 1: Mathematical model for a laminar, two-dimensional, nonadiabatic, nonisothermal, bidispered, linear driving force adsorptive system.

Bulk Continuity of Active Gas:

$$\frac{\partial y_b}{\partial t}+\frac{\partial v_r y_b}{\partial r}+\frac{\partial v_z y_b}{\partial z}=D\left(\frac{\partial^2 y_b}{\partial z^2}+\frac{1}{r}\frac{\partial}{\partial r}\left(r\frac{\partial y_b}{\partial r}\right)\right)+\frac{1-\varepsilon_b}{\varepsilon_b}3\frac{k_f}{r_p}\frac{1}{\frac{r_p k_f}{5\varepsilon_p D_p}+1}\left(y_b-\bar{y}_p\right)$$

Ergun Equation:

$$\frac{\partial P}{\partial r}=v_r\left(\frac{150\mu(1-\varepsilon_b)^2}{4r_p^2\varepsilon_b^3}+\frac{1.75\rho_g}{r_p}\frac{1-\varepsilon_b}{\varepsilon_b}v_r\right)$$

$$\frac{\partial P}{\partial z}=v_z\left(\frac{150\mu(1-\varepsilon_b)^2}{4r_p^2\varepsilon_b^3}+\frac{1.75\rho_g}{r_p}\frac{1-\varepsilon_b}{\varepsilon_b}v_z\right)$$

Linear Driving Force of Intrapellet Phase for Active Gas:

$$\varepsilon_p\frac{\partial\overline{y_p}}{\partial t}=\varepsilon_p 3\frac{k_f}{r_p}\frac{1}{\frac{r_p k_f}{5\varepsilon_p D_p}+1}\left(y_b-\bar{y}_p\right)-\frac{15D_c}{\varepsilon_p r_c^2}\frac{\rho_p RT}{P}\left(\bar{q}_s-\bar{q}\right)$$

Linear Driving Force of Adsorbed Phase for Active Gas:

$$\frac{\partial\bar{q}}{\partial t}=\frac{15D_c}{\varepsilon_p r_c^2}\left(\bar{q}_s-\bar{q}\right)$$

Loading Rate Correlation Isotherm Model:

$$\bar{q}_s=\frac{A_i exp\left(\frac{B_i}{T}\right)C_i exp\left(\frac{D_i}{T}\right)P_i X_i}{1+C_i exp\left(\frac{D_i}{T}\right)P_i X_i}$$

Constitutive relationships:

$$\lambda=k_g\left(7+0.5\left(\frac{2\,r_p\,\rho_g v_z\,\varepsilon_b}{\mu}\right)\left(\frac{C_{p,t}\,\mu}{k_g}\right)\right)$$

Energy Balance for Both Gases and Pellets:

$$\frac{\partial}{\partial t}\left(T\left(y_b C_P+y_c C_{P,c}\right)\right)+\frac{1-\varepsilon_b}{\varepsilon_b}\frac{\partial}{\partial t}\left(T\left(C_P\bar{y}_p+\frac{\bar{q}\rho_p RT}{P}C_P+\frac{C_{P,s}\rho_p RT}{P}\right)\right)+C_{P,c}\left[\frac{\partial(v_z y_c T)}{\partial z}+\frac{\partial(v_r y_c T)}{\partial r}\right]+$$
$$C_P\left[\frac{\partial(v_z y_b T)}{\partial z}+\frac{\partial(v_r y_b T)}{\partial r}\right]=\lambda\frac{RT}{P}\left[\frac{\partial^2 T}{\partial z^2}+\frac{1}{r}\frac{\partial}{\partial r}\left(r\frac{\partial T}{\partial r}\right)\right]+\frac{1-\varepsilon_b}{\varepsilon_b}(-\Delta H)\frac{\rho_p RT}{P}\frac{\partial\bar{q}}{\partial t}$$

Table 2: Initial conditions and boundary conditions for simulation.

Initial conditions:	
$y_b\|_{t=0} = 0$	$\bar{q}\|_{t=0} = 0$
$\bar{y}_p\|_{t=0} = 0$	$T\|_{t=0} = 296\ K$
$y_c\|_{t=0} = 0$	
General boundary conditions:	
$\frac{\partial y_b}{\partial r}\|_{r=0} = 0$	$\frac{\partial v_r}{\partial r}\|_{r=0} = 0$
$\frac{\partial y_b}{\partial r}\|_{r=R_0} = 0$	$\frac{\partial v_z}{\partial r}\|_{z=0} = 0$
$\frac{\partial P}{\partial r}\|_{r=0} = 0$	$\frac{\partial T}{\partial z}\|_{z=0} = 0$
$\frac{\partial T}{\partial r}\|_{r=0} = 0$	$y_b\|_{z=0} = 0.015$
$\frac{\partial T}{\partial r}\|_{r=R_0} = \frac{h}{\lambda}\left[T_\infty - T\|_{r=R_0}\right]$	

Table 3: Parameters used in simulations.

$A_i = 1.31$ mol/kg	$k_f = 0.0398$ m/s
$B_i = 170.7$ K	$k_g = 0.02$ W/mK
$C_i = 6.437\ 10^{-5}$ kPa^{-1}	$P = 269$ kPa
$C_{P,s} = 920$ J/kgK	$r_p = 0.0016$ m
$D = 0.0000064$ m^2/s	$r_c = 0.000001$ m
$D_c = 3.73 * 10^{-12}$ m^2/s	$\rho_p = 1140$ kg/m^3
$D_i = 2895.5$ K	$\varepsilon_b = 0.395$
$D_p = 0.0000032$ m^2/s	$\varepsilon_p = 0.27$
$h = 20$ W/m^{2}K	$V_b = 0.005815$ m^3
$-\Delta H = 52777$ J/mol	$\chi_i = 13.6$
$\dot{m} = 0.005, 0.00728, 0.01, 0.015$ kg/s	
$r_b = 0.078, 0.102, 0.154, 0.203, 0.334, 0.477$ m	

In Table 1, the bulk continuity of the active gas addresses the conservation of mass of the active gas residing outside of the adsorbent pellets, where y_b is the bulk mole fraction of active gas, t is time, v_r is the radial flow velocity, v_z is the axial flow velocity, r is the radial distance, z is the axial distance, D is the bulk diffusivity, D_p is the intrapellet diffusivity, ε_b is the bed porosity, ε_p is the pellet porosity, k_f is the mass transfer resistance, r_p is the pellet radius, and $\bar{y}_p$ is the average interphase mole fraction of active gas. The bulk continuity equation includes a source term representing movement of the active gas between the bulk phase and intrapellet phase. Also in the bulk phase, the Ergun equations are used to address conservation of momentum, where P is the total pressure, μ is the bulk phase viscosity, and ρ_g is the density of gas from source at adsorption pressure. These equations address pressure drop across a porous medium, and increase as the flow velocity increases or the pellet radii decrease.

Within the adsorbent pellets, the two linear driving force equations describe how the active gas is transported between the adsorbed phase, intrapellet phase, and bulk phase. In these equations, D_c is the diffusivity in the adsorbed phase, ρ_p is the density of adsorbent pellets, R is the universal gas constant, T is the temperature, r_c is the adsorbent crystal radius, $\bar{q}_s$ is the saturation limit of adsorbed phase concentration per pellet mass, and $\bar{q}$ is the average adsorbed phase concentration per pellet mass. The adsorption saturation limit is a function of temperature and pressure, and is represented via the Loading Rate Correlation Isotherm Model, where A_i, B_i, C_i, D_i, and X_i are all empirically determined from adsorption data.

Adsorption is an exothermic process, and the conservation of energy is represented via the energy balance equation and the constitutive relationship for heat transfer, where λ is the constitutive heat transfer coefficient, k_g is the gas conductivity, $C_{p,t}$ is the average specific heat of the bulk gas mixture, C_P is the active gas heat capacity, y_c is the bulk mole fraction of carrier gas, $C_{P,c}$ is the carrier gas heat capacity, and ΔH is the isosteric heat of adsorption.

Initial and boundary conditions are provided in Table 2. Initially, the entire adsorption column and adsorbent are void of propylene gas and the column is at 296 K. The column is filled with inert nitrogen. Once the simulation begins, the inlet mole fraction of propylene is 0.015. The column is assumed to be axisymmetric, and external heat transfer exists via natural convection.

The open region is simulated using the re-normalization group (RNG) k-ε turbulence model. A turbulence model is used in place of a large eddy simulation or direct numerical simulation to save computational time. This specific turbulence model was selected via comparison with large eddy simulation results, and the details of this comparison will be described in Section 3.

2.3 Results and Discussion

In the open literature on axial- and radial-flow fixed bed reactors, no computational model has been presented that addresses both the turbulences in the open regions of a column and the heat and mass transfer of the reacting region. In order to evaluate the performance of adsorption columns across a range of different operating parameters, it is necessary to include all of these effects.

As there is no single source in the open literature for validating fluid flow through an axisymmetric adsorption column while accounting for the entrance and exit effects, three separate validation results are presented, each focusing on different aspects of the modeling effort in this paper. The axisymmetric effects, which account for diffusion in addition to convection, are validated against an axisymmetric nonreactive experiment. Adsorption phenomena are validated against a quasi-one-dimensional experimental adsorption column, and turbulence effects are validated against multiple large eddy simulations.

The two-dimensional effects of flow through a porous region were validated against experimental data from Fahien and Smith [20], as presented in Figure 3a. In their experiment, as depicted in the inset in Figure 3a, air was pumped through a porous bed of inert glass beads. A small pitot tube was then used to inject carbon dioxide into the center of the porous bed, and the concentration of carbon dioxide was measured at multiple axial and radial locations downstream. The reported axial distance was measured from the tip of the Pitot tube, and the concentration (C) has been nondimensionalized with respect to the initial carbon dioxide concentration (C_0). Due to the combined effects of convection and diffusion, the concentration profile spreads increasingly outwards radially as the axial distance increases, and the simulation results shown by the solid lines are seen to match very closely with the experimental data (shown by markers) in Figure 3a.

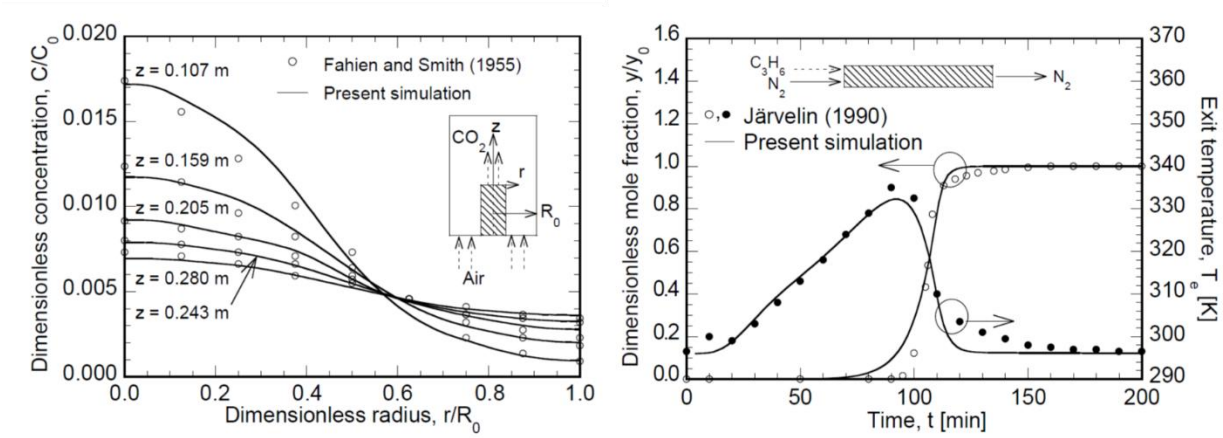

Figure 3: Validation of adsorption model: (a) comparison of two-dimensional flow characteristics against experiment and (b) comparison of breakthrough curves against experiment.

The adsorption model was validated against the experimental work of Järvelin [7], in which, a bed of Zeolite 13X pellets was initially pressurized with pure nitrogen. At time zero, a mixture of nitrogen and propylene was injected into the inlet of the bed. The mole fraction of propylene and the temperature of the exiting mixture were measured at the outlet from time zero until after the inlet concentration of propylene was seen at the exit. Figure 3b presents the comparison in terms of a nondimensionalized mole fraction relative to the inlet mole fraction. It can be seen in the figure that until approximately 5,500 seconds, there is no propylene exiting the columns. This long time lag, far longer than would be observed over an inert bed of the same dimensions, is on account of the fact that the propylene within the column is being adsorbed. Once the Zeolite 13X is saturated, the mole fraction of propylene rapidly increases to the inlet fraction. It can also be

seen in Figure 3b that the temperature climbs during the exothermic adsorption process, and then falls back down to the inlet temperature shortly after the Zeolite 13X has been saturated with propylene and no more adsorption is taking place. The present simulation closely matches both the temperature and mole fractions measured by Järvelin [21].

Due to the lack of detailed experimental data for the turbulent flow within the open regions of the reactor column, multiple Large Eddy Simulations (LES) with a Smagorinsky-Lilly subgrid-scale model were used as a benchmark. Specifically, the pressure drop between the column inlet and outlet for axial flow (Figure 1) along a nominally 6-inch column with a flowrate of 0.01 kg/s was used as a benchmark to compare various turbulence models and the LES. Due to the significant computational time required for an LES run, the simulations were carried out just long enough to reach a quasi-equilibrium, and the simulation was refined until grid convergence was achieved. Figure 4 compares the resultant pressure drop from using the standard k-ε, standard k-ω, realizable k-ε, and re-normalization (RNG) k-ε turbulence models, a laminar simulation, and the LES. As can be seen from this figure, there is initially a very high pressure necessary to start the flow, which is an artifact of simulating an instantaneous initial velocity. Once the pressure

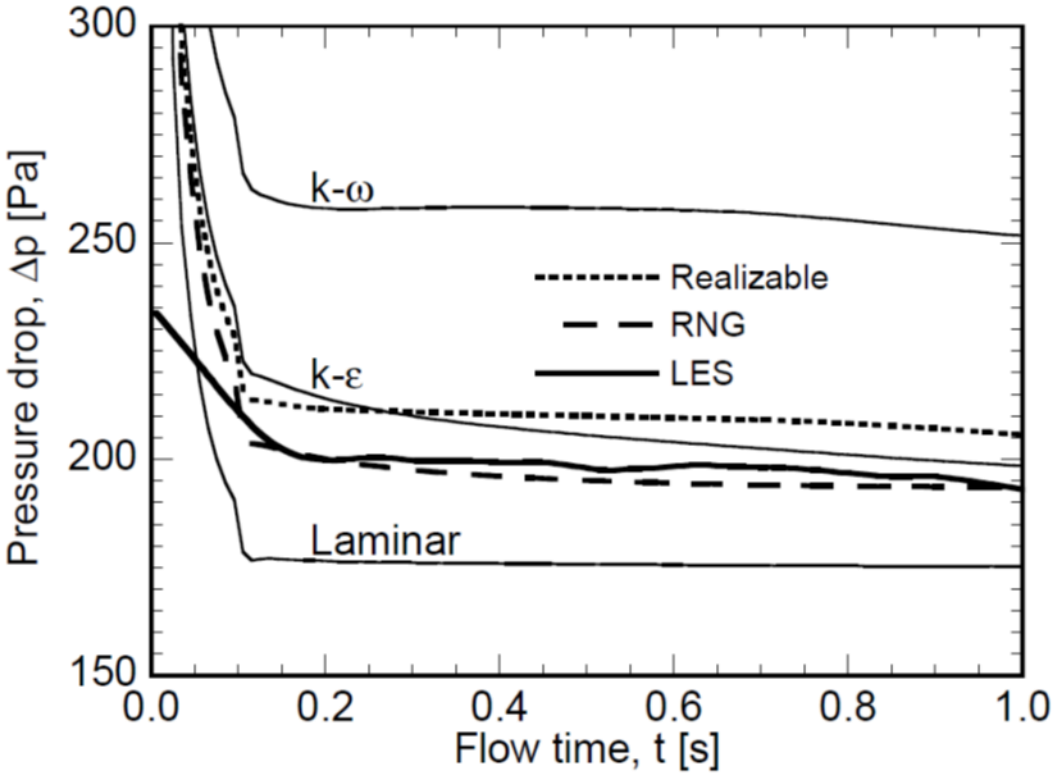

Figure 4: Comparison of a Large Eddy Simulation with various turbulence models for axial-flow fixed bed reactor.

settles to quasi-equilibrium, it is readily seen that the RNG turbulence model provides the closest fit.

Similarly, turbulent flows in the radial-flow configurations were validated by simulating the pressure drop from column inlet to outlet for all four radial geometries in Figure 2 with a nominal 6-inch diameter, and a flow rate of 0.015 kg/s for all but the CF-Z configuration; due to significant maldistribution in the flow path, the flow rate in the case of the CF-Z geometry was reduced to 0.00728 kg/s. The variations of the pressure drop with flow time for the CF-Z, CF-Π, CP-Z, and CP-Π configurations are presented in Figure 5a, b, c, and d, respectively. In Figure 5a, the pressure drop across the CF-Z flow configuration is seen to be lower than that in the other configurations (Figure 5b, c, and d), owing to the reduced flow rate considered in this case. Among the other three flow configurations, the CF-Π geometry exhibits a lower pressure drop (Figure 5b) than either of the CP scenarios in Figure 5c or d, which will be discussed in more detail later in this section. Of the turbulence models considered in Figure 5a and b, the RNG and realizable models provide the closest values to the large eddy simulation based turbulence modeling. For the two CP scenarios, shown in Figure 5c and d, the RNG is shown to provide the closest comparison to LES, noticeably better than the realizable turbulence model. Based on these

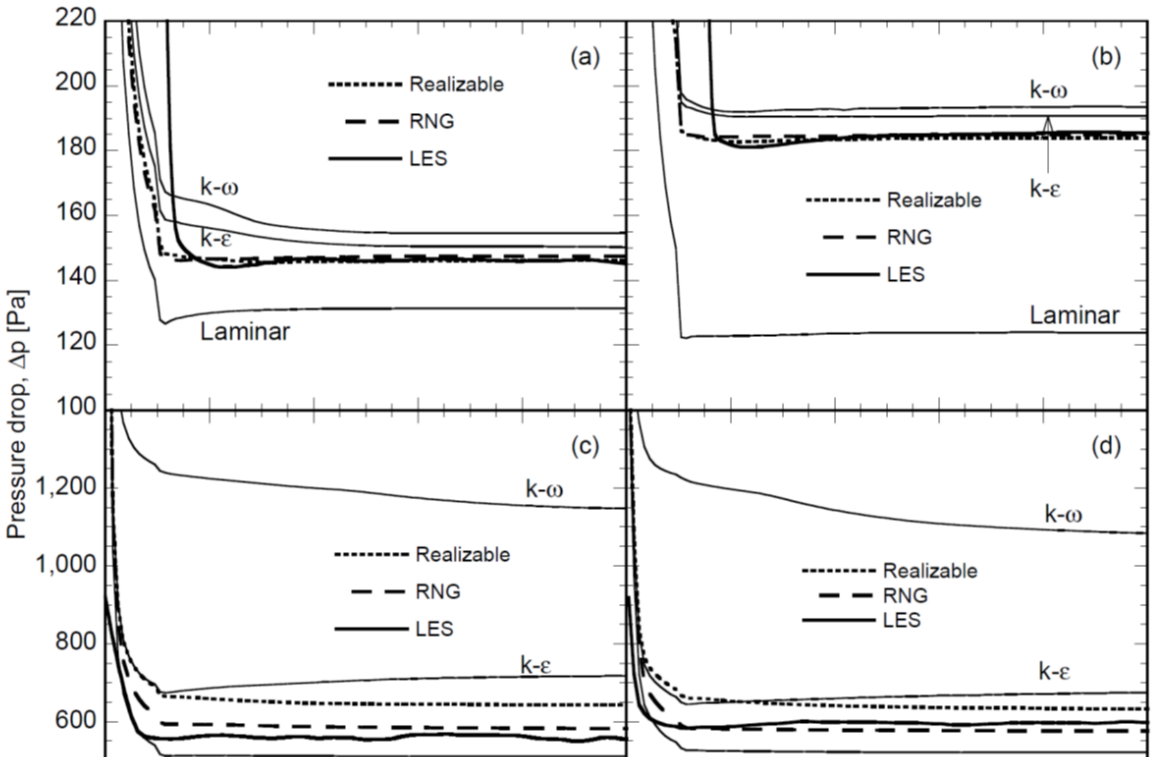

Figure 5: Comparison of a Large Eddy Simulation with various turbulence models for different radial-flow fixed bed reactor.

results, the RNG turbulence model was used for the simulations of all the axial and radial flow configurations in the study.

The flows through the axial and radial beds are analyzed in terms of the two performance parameters, bed utilization and pressure drop. From a bed design point of view, the utilization is sought to be maximized while minimizing pressure drop. The effects of the mass flow rate as the operating parameter and the bed diameter as the bed geometric parameter on the bed utilization and the pressure drop are examined in the discussion below for axial and radial flow configurations.

The utilization (i.e. the amount of the adsorption column that is fully saturated) of the bed for a range of axial-flow geometries is presented qualitatively in Figure 6a and b for the adsorption of propylene from a mixture of propylene and nitrogen by a bed composed of Zeolite 13X. For all columns, the adsorbent bed extends the length of the straight section of the column, as is shown in Figure 1, and the mass flow rate was held at a constant 0.01 kg/s. Column geometries were varied to maintain a constant volume of adsorbent for the range of specified bed diameters. In Figure 6a, the mole fraction of propylene in the bulk phase after 20 minutes of operation is shown for all geometries, with the mole fraction ranging from the inlet value of fully saturated (black) to zero mole fraction (white). In Figure 6b, the concentration of propylene in the adsorbed phase after 20 minutes of operation is shown, with a saturation level of propylene shown in black, an

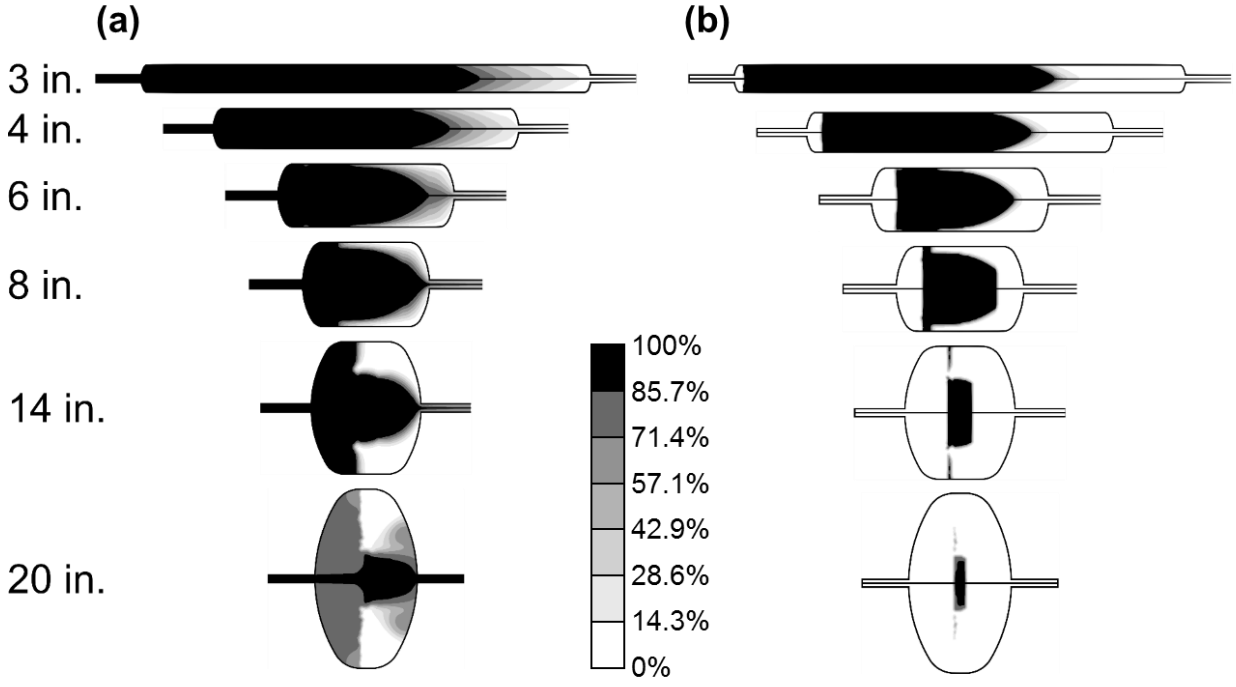

Figure 6: Bed utilization for axial-flow reactors: (a) mole fraction in bulk phase and (b) saturation level in adsorbed phase.

absence of propylene in white, and gradients between these extremes shown in gray. A set time of 20 minutes was chosen to evaluate the bed utilization in order to provide a consistent benchmark for comparison: all bed geometries will eventually reach complete utilization through diffusion. For both parts of this figure, flow is from left to right.

As would be expected, the 3 inch scenario most closely approximates plug flow, and has the greatest utilization, but the performance starts to drop rapidly as the diameters are increased further. This performance drop is most vividly apparent for the 20 inch scenario, where only a small fraction of the adsorbent is utilized. Instead of distributing the mixture of propylene and nitrogen throughout the bed, the mixture travels as a jet through the center of the bed.

The qualitative utilization results from Figure 6 are quantified in Figure 7, taking the ratio of amount of adsorbent saturated over the total capacity of the adsorbent. Additionally, the tradeoffs between pressure drop and flow rate for the different bed geometries. As can be seen in Figure 7, the pressure drop and bed utilization are directly correlated, with an increase in utilization resulting in an increase in pressure drop: improving the bed utilization performance reduces the pressure drop performance, and vice versa. This tradeoff is due to the fact that a small bed diameter, which facilitates high utilization, increases the length of the bed and thus increases the distance that the fluid must travel through the porous bed. Additionally, it can be seen that flowrate is inversely correlated with pressure drop, where an increased flowrate—and thus increased system performance—also increases the pressure drop. The relationship between flowrate and utilization is more complicated. For small bed diameters, an increase in flowrate improves bed utilization because the fluid can travel a greater distance through the bed in a given amount of time. In contrast, for larger diameters the increased flowrate results in the fluid forming more of a jet through the adsorbent bed, and the outer regions of the bed are left underutilized.

In order to compare the overall system performance of different bed geometries at various flowrates, an overall performance metric has been developed and is presented in the equation below:

$$P_M = \frac{\tilde{U}}{\widetilde{\Delta p}} \tag{1}$$

In this equation, P_M is the overall performance metric, U is the bed utilization, $\dot{m}$ is the mass flowrate, Δp is the pressure drop, and the factor of 1,000 is used to scale the result into moderate ranges. The results of applying this metric to the axial flow geometries can be seen in Figure 8. As would be expected, the smaller diameter beds perform poorly on account of the high pressure drop inherent in these beds and the larger diameter beds suffer from poor utilization. Overall, the best performance is seen for the 14 inch geometry at 0.005 kg/s, the lowest flowrate. The success of this scenario is due to the low pressure drop of the short column combined with the

decent utilization from a relatively low flowrate—creating a flow that is affected by diffusion in addition to convection. But for practical purposes, higher flowrates may be necessary, at which point the utilization of the 14 inch column drops off rapidly. For all but the lowest flowrates, the 8 inch column provides the best overall performance, and would be recommended for the majority of operating conditions.

In contrast to axial-flow reactors, radial-flow reactors are appealing because of their potential to reduce pressure drop [16]. This reduction is due to the shorter distance between the high

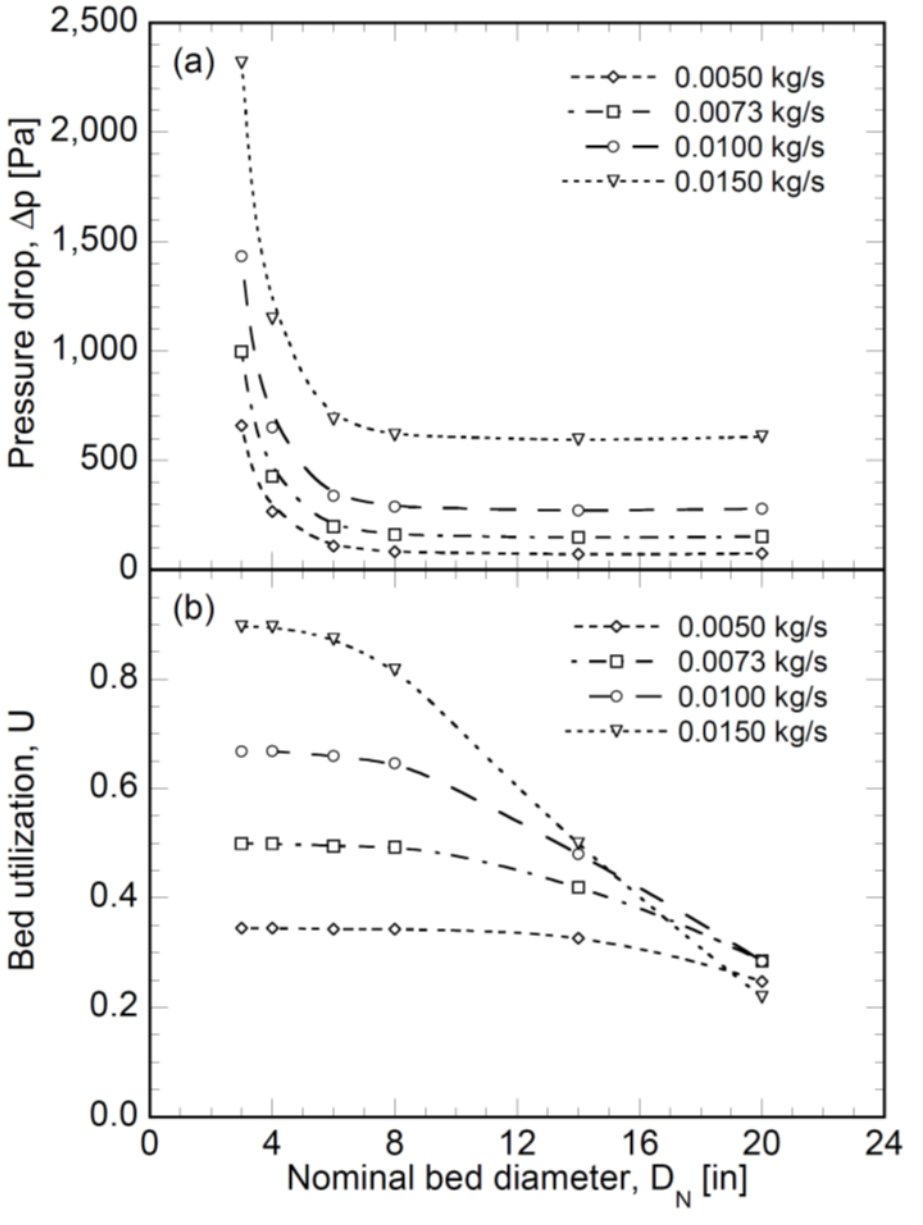

Figure 7: Operating parameters as a function of bed diameter for axial-flow fixed bed reactors.

pressure side of the reaction zone and the low pressure side when compared against axial bed. But this benefit is traded for greater flow maldistribution than typical axial scenarios, and large portions of the bed may remain underutilized.

The qualitative bed utilization for radial-flow geometries are presented in Figure 9a and b. A shorter range of bed diameters is analyzed in the radial flow scenarios compared to the axial scenarios due to geometrical limitations. As with the axial flow scenarios, Figure 9a presents the mole fraction of propylene in the bulk phase after 20 minutes of operation with the inlet mole fraction shown in black, a zero mole fraction shown in white, and gradients shown in shades of gray. Figure 9b presents the adsorbed concentration of propylene, with black representing a fully saturated adsorbent, white an empty adsorbent, and grays for the gradient between these extremes. For all scenarios the flow paths are described via the arrows in Figure 2.

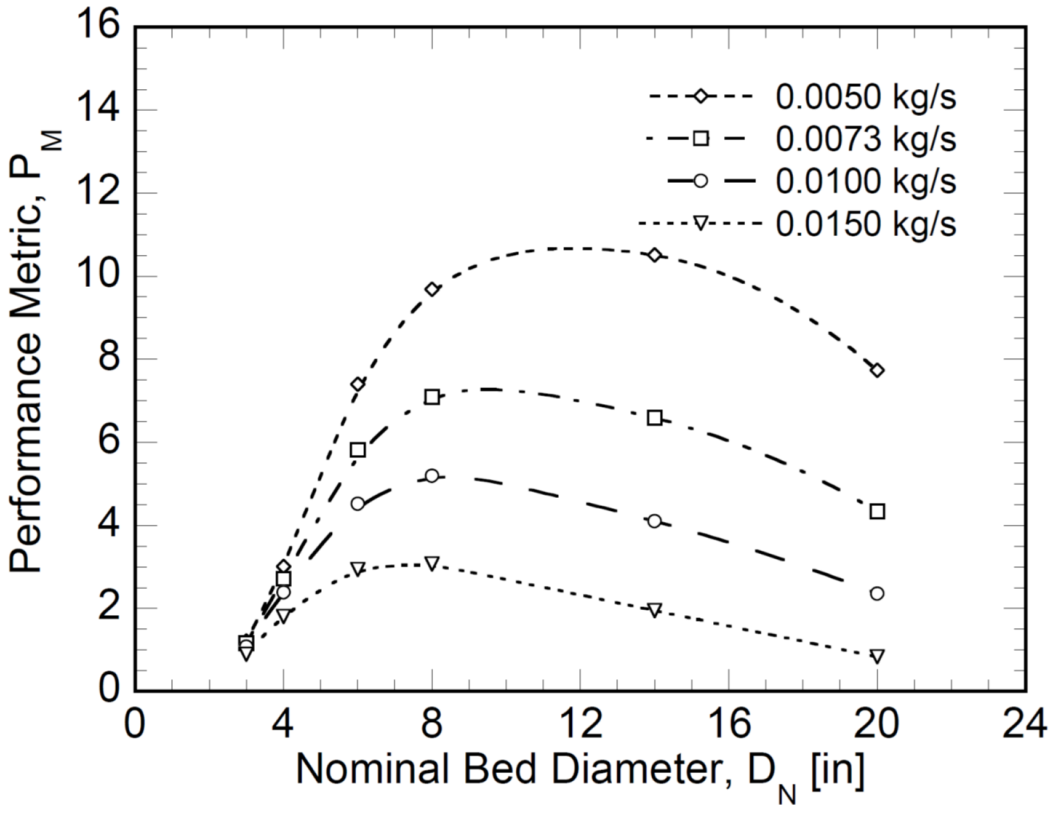

Figure 8: Performance metric as a function of bed diameter for axial-flow fixed bed reactors.

Bed utilization is a concern with radial flow scenarios, primarily due to the inertia of the inlet fluid. As can be seen with both of the CF scenarios, where the fluid flows from the center of the column outwards radially to the annulus outside of the adsorbent region, the bulk of the flow

and adsorption is biased towards the plate at the end of the adsorbent region. In the CP scenarios, the bulk of the flow is biased towards the end wall of the column. This biasing is evident in all four radial flow scenarios, but is least severe for the beds with the largest diameters. This increased utilization is similar in nature to the increased utilization seen for small diameter axial flow scenarios: in both cases, the fluid must travel a longer distance through the adsorbent region while being relatively contained from significant dispersion. In the axial scenarios, the primary flow direction is axial, and a small radius limits dispersion in the radial direction. In the radial scenario, the primary flow direction is radial, and a small axial length limits axial dispersion.

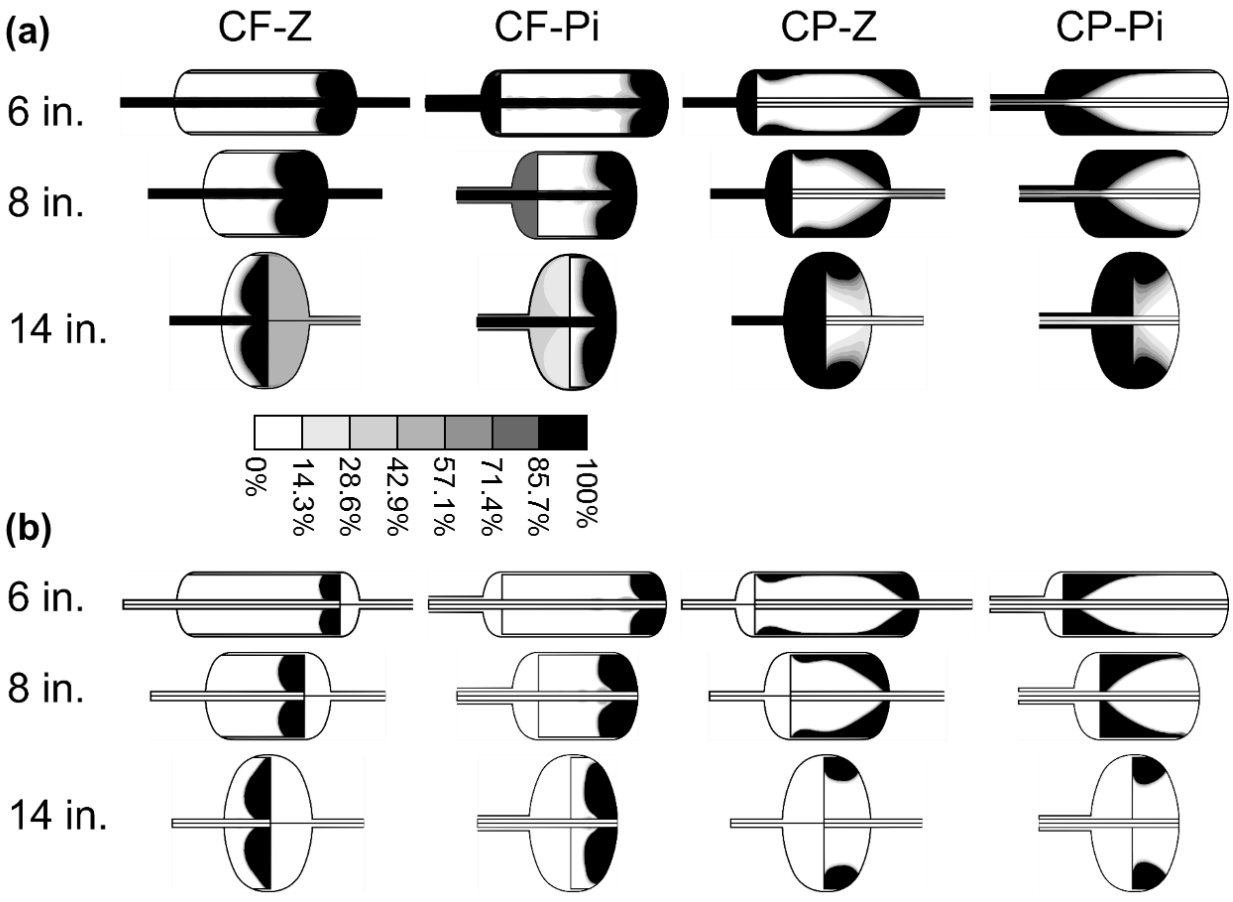

Figure 9: Bed utilization for radial-flow reactors: (a) mole fraction in bulk phase and (b) saturation level in adsorbed phase.

A summary of performance results for all radial flow scenarios is shown in Figure 10, with a-d presenting pressure drop and e-h bed utilization. Figure 10a and e are for the CF-Z scenarios, 10b and f for CF-Π, 10c and g for CP-Z, and 10d and h for CP-Π. As can be readily seen from this

figure, the pressure drop is significantly lower than for comparable axial flow scenarios, but this benefit comes at the expense of a small reduction in bed utilization.

For the CF-Z and CF-Π radial flow scenarios, as is shown in Figure 10a and e, an increase in bed utilization comes with an increase in pressure drop. Additionally, there is a strong correlation between the flow rate and pressure drop: an increase in flowrate drives an increase in pressure drop. The relationship between flowrate and bed utilization is more complex, but abides by similar phenomena to the same relationship for axial flow scenarios: where flow maldistribution is particularly severe, high flowrates exacerbate the poor maldistribution, but at lower flowrates the fluid is able to diffuse throughout the entire adsorbent region.

The two CP radial flow scenarios behave in a similar manner to the CF scenarios with one notable exception: instead of monotonically increasing bed utilization with bed diameter for all flowrates, multiple simulations with lower flowrates see a drop in bed utilization at greater bed diameters. At these low flowrates for CP scenarios, there is fluid entering the adsorbent column across nearly the entire axial length of the column. And beds with smaller diameters have a larger inlet flow area for the adsorbent region. Therefore, at low flowrates the beds with smaller diameters can take advantage of the increased flow area to achieve a greater bed utilization.

The overall system performance of all radial flow scenarios is analyzed using Equation 1, and the results are shown in Figure 11, with CF-Z in a, CF-Π in b, CP-Z in c, and CP-Π in d. As is immediately apparent from this figure, the radial flow scenarios tend to achieve performance metric ratings that are an order of magnitude better than similar scenarios for axial flow geometries. This large disparity is due to the fact that although radial flow scenarios tend to have a marginally lower bed utilization, the pressure drop is frequently drastically smaller than that seen in axial flow scenarios.

As can be seen in Figure 11, the CF scenarios—in Figure 11a and b—outperformed the CP scenarios—in 11c and 11d—by a small margin. The disparity is due to the slightly smaller pressure drop for the CF scenarios, as is seen in Figure 10. Between the two CF scenarios, the CF-Z scenario performed better for lower flowrates and the CF-Π for higher flowrates.

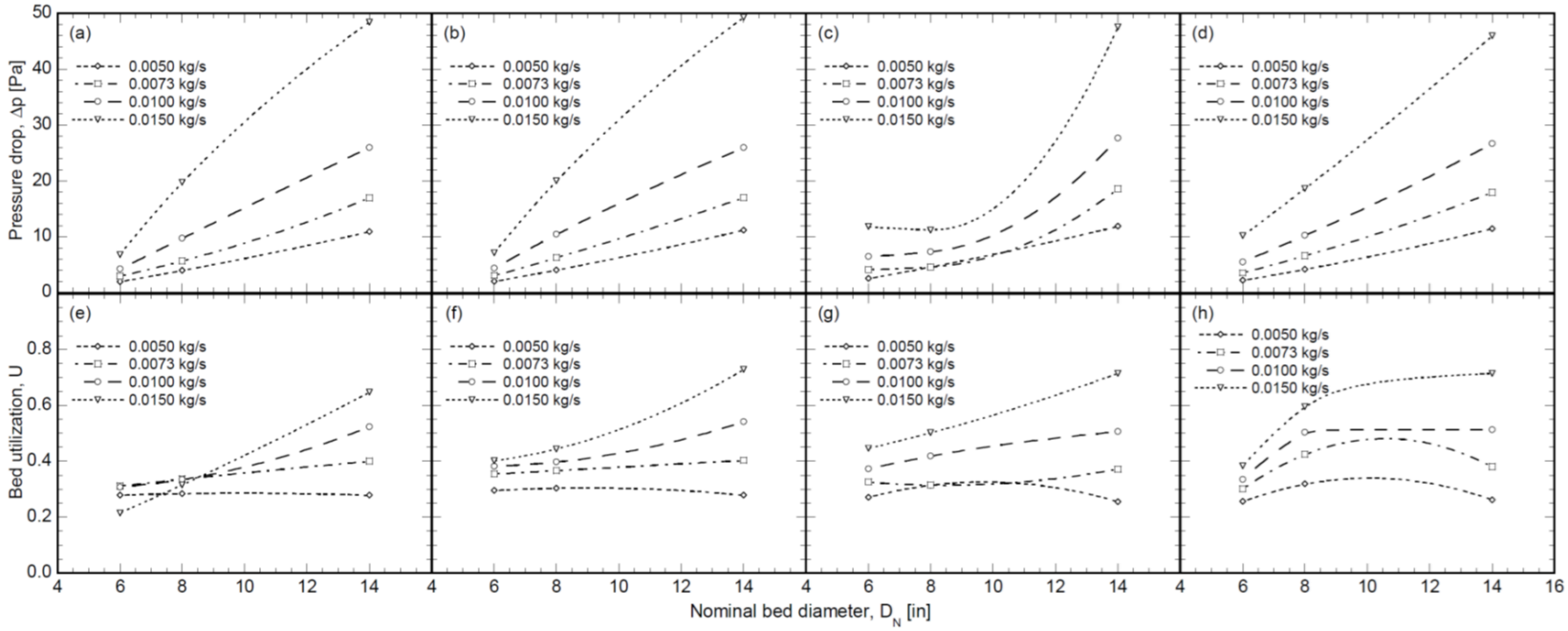

Figure 10: Operating parameters as a function of bed diameter for CP-Π radial-flow fixed bed reactors.

Across all bed geometries analyzed, the 6 inch CF-Π geometry achieved the highest performance metric value. The success of this scenario was due to the drastic reduction in pressure drop achieved: at 0.015 kg/s, the pressure drop for this scenario was 49 Pa, and the lowest axial pressure drop at this flowrate was 594 Pa for the 14 inch scenario. But this order of magnitude reduction in pressure drop also results in a reduction in utilization from 0.5 for the 14 inch axial scenario with 0.015kg/s to 0.38. In order to compensate for this relatively low utilization, it is recommended that the column be modified to accommodate this. This modification could either take the form of baffles which could drive the flow to the unused portions of the adsorption column, or replacing the unused adsorbent region with inert and inexpensive pellets.

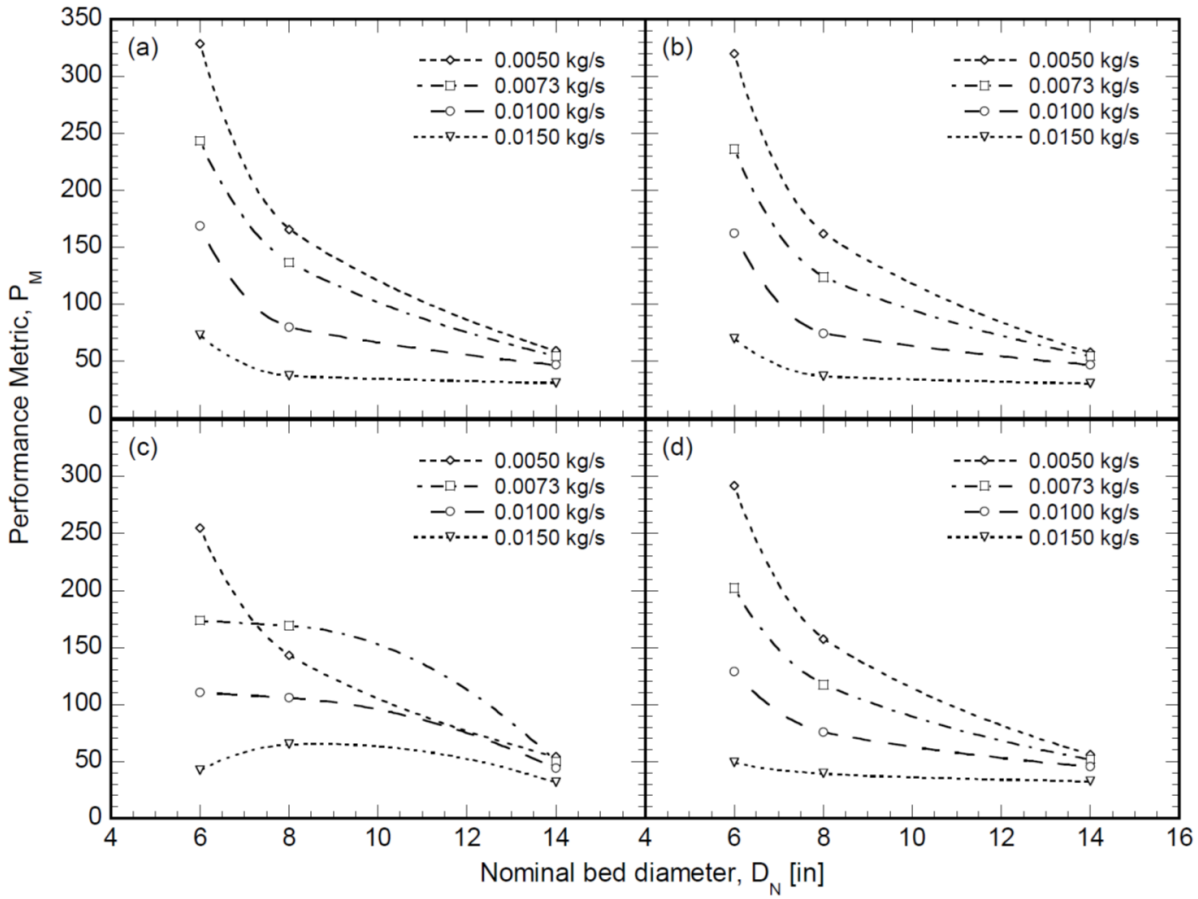

Figure 11: Performance metric as a function of bed diameter for radial-flow fixed bed reactors.

2.4 Conclusion

The operating performance of a fixed bed reactor is driven largely by three interdependent parameters: pressure drop, bed utilization, and working fluid flowrate. This paper has analyzed the effects of parametrically varying these parameters across an axial-flow reactor and four different styles of radial-flow reactors. Although axial flow reactors are more common in industry, there is significant potential to reduce pressure drop across fixed bed reactors—and thereby reduce the power consumption—by switching to radial flow reactors. This reduction in pressure drop is due to the shorter distance between the high pressure and low pressure side of the adsorption column for radial flow geometries when compared against comparable axial flow reactors. But this reduction in pressure drop comes at the price of a reduction in bed utilization. By accounting for all three driving parameters, it is possible to identify a bed geometry that is optimal for any given scenario.

Specifically, it was demonstrated that length to diameter ratio near unity provided the optimal axial flow geometry for a pressure vessel with elliptical dished tank heads. Beds with greater ratios saw unnecessary increases in pressure drop, and beds with lower ratios saw poor utilization. By switching from axial to radial flow reactors, it is possible to improve the overall performance, and the CF-Z flow configuration with the smallest possible diameter provided the best overall performance.

2.5 Nomenclature for Chapter 2

A_i = loading rate correlation for isotherm model coefficient [mol/kg]
B_i = loading rate correlation for isotherm model coefficient, K
C_i = loading rate correlation for isotherm model coefficient, kPa^{-1}
C_P = active gas heat capacity, kJ/kg K
$C_{P,c}$ = carrier gas heat capacity, kJ/kg K
$C_{P,p}$ = adsorbent pellet heat capacity, kJ/kg K
$C_{P,t}$ = average specific heat of bulk gas mixture, kJ/kg K
D = bulk diffusivity, m^2/s
D_c = diffusivity in adsorbed phase, m^2/s
D_i = loading rate correlation for isotherm model coefficient, K
D_p = diffusivity in intrapellet phase, m^2/s
h = external heat transfer coefficent for adsorption column, $\mathrm{W/m}^2$ K
ΔH = isosteric heat of adsorption, kJ/mol
k_f = mass transfer resistance, m/s
k_g = gas conductivity, $\frac{\mathrm{W}}{\mathrm{m}}\mathrm{K}$

$P =$ total pressure, kPa

$P_i =$ partial pressure, kPa

$\bar{q} =$ average adsorbed phase concentration per pellet mass, mol/kg

$\bar{q}_s =$ saturation limit of adsorbed phase concentration per pellet mass, mol/kg

$r =$ radial distance, m

$R =$ universal gas constant, J/mol K

$R_0 =$ radius of column, m

$r_c =$ adsorbent crystal radius, m

$r_p =$ pellet radius, m

$t =$ time, s

$T =$ temperature, K

$T_\infty =$ ambient temperature outside of adsorption column, K

$v_r =$ radial flow velocity, $\frac{\text{m}}{\text{s}}$

$v_z =$ axial flow velocity, m/s

$y_b =$ bulk mole fraction of active gas

$y_c =$ bulk mole fraction of carrier gas

$\bar{y}_p =$ average interphase mole fraction of active gas

$z =$ axial distance, m

$\varepsilon_b =$ bed porosity

$\varepsilon_p =$ pellet porosity

$\lambda =$ constitutive heat transfer coefficient, kJ/m K

$\mu =$ bulk phase viscosity, Pa s

$\rho_g =$ density of gas from source at adsorption pressure, kPa

$\rho_p =$ density of pellet, kg/m^3

$\chi_\text{i} =$ loading rate correlation for isotherm model coefficient

Chapter 3: Uncertainty Analysis of the Performance of Zeolite Adsorption Systems

Zeolites are widely used for commercial separation and catalysis, and many performance properties of zeolites are driven by the stochastic locations of aluminum atoms within the zeolite's crystalline framework. This inherent variability in molecular-level characteristics of zeolites can significantly affect the macroscale behavior of adsorption systems, and quantifying these effects is critical for the accurate prediction of system behavior. This paper quantifies the uncertainty in the performance properties of the adsorption of methane and propane on Zeolite X, and then presents the macroscale uncertainty which results.

3.1 Introduction

Zeolites are widely used in industry as adsorbents and catalysts due to their high surface area and—in cases where some silicon atoms have been substituted with aluminum atoms—the ability to capture cations [22, 23]. These crystals can be manufactured entirely from a lattice of silicon and oxygen, but it is far more common to replace a percentage of the silicon atoms with aluminum atoms. This replacement brings about an imbalance in charge—aluminum has one fewer valence electron than silicon—and necessitates the addition of a cation for each replaced silicon to balance the zeolite's overall charge. The location of these cations can have a substantial impact on the performance properties of the zeolite, such as equilibrium adsorption; but, due to the nature of zeolite manufacture, there is frequently significant variability in the specific location of aluminum atoms. This significant impact of aluminum locations on zeolite properties, combined with the inherent uncertainty, has made the study of aluminum locations an active area of research.

Determining the location of aluminum atoms with current experimental techniques is fraught with challenges [24, 25]. On account of the disordered and non-periodic distribution of zeolites with aluminum substitutes, crystallographic diffraction methods cannot accurately locate aluminum atoms [26-28]. Spectroscopic techniques, such as NMR spectroscopy, have also been unable to identify the specific aluminum distribution for all zeolites with certainty, but they have been able to accurately determine the ratio of silicon [25] and aluminum as well as to validate Löwenstein's rule [29], that describes limitations on the likely structure of a zeolite framework for the location of aluminum atoms: Löwenstein's rule requires that no oxygen atom be bonded to more than one aluminum atom, thereby prohibiting Al-O-Al linkages.

In response to these experimental difficulties, several computational approaches have been explored. The simplest of these methods is to replace all silicon and aluminum atoms in the zeolite

structure by "averaged" atoms that bear the mean partial charges of all of the silicon and aluminum atoms based on the Si/Al ratio [30, 31]. A more rigorous approach is to analyze zeolites with very high Si/Al ratios and, therefore, a very small number of aluminum atoms, such that the entire range of possible aluminum arrangements can be simulated [24, 25]. But since most industrial applications of zeolites rely on much smaller Si/Al ratios, a more practical approach for handling the uncertainty in aluminum locations has been to perform deterministic simulations on randomly assigned aluminum atom locations, with the only constraint being that the aluminum locations obey Löwenstein's rule [32, 33]. This rigorous technique has been shown to have success "matching" a specific batch of zeolite—where different combinations of locations were tested and compared against specific experimentally measured properties—but has not been used to predict the possible range of zeolite properties from all manufacturing batches of zeolite.

This paper—focused on one of the most commonly used commercial zeolite, Zeolite X—builds off of the rigorous technique of randomly assigning aluminum locations that obey Löwenstein's rule, as described in Refs. [32] and [33], but adds a stochastic approach to account for the variability in any batch of zeolite, making these results more general. Additionally, this paper then extends the molecular-level results for Zeolite X to the macroscale—simulating the separation of a methane/nitrogen mixture and a propane/nitrogen mixture through the use of a fixed bed scenario—and analyzes how this molecular-level uncertainty drives the overall system performance uncertainty.

The organization of this paper is as follows: the specific methodologies used, for molecular modeling, macro-scale modeling, and handling the uncertainty analysis, are presented in Section 2; validation of each of these methodologies and results are presented and discussed in Section 3; and the paper is brought to a conclusion in Section 5.

3.2 Methods

Zeolite X, represented by $Na_xAl_xSi_{192-x}O_{384}$ with Si/Al ratios between 1.0 and 1.5 [34], is one of the most common zeolite structure used in commercial separation and catalysis [33] and a representative unit cell of Zeolite X is shown in Figure 12. In this figure, oxygen atoms are shown as white spheres, and can be seen to be bonded to two nearby atoms; silicon is shown as light gray spheres, and can be seen to be bonded to four nearby atoms; aluminum is shown as black, and can be seen to be bonded to four nearby atoms; sodium cations are shown in dark gray, and can be seen to be unbonded. This figure highlights Löwenstein's rule, where Al-O-Al bond patterns are never present. And the difficulty in performing an experimental spectroscopic

analysis to determine the location of aluminum atoms due to the lack of a regular distribution of aluminum atoms is apparent. Lastly, the complexity of the zeolite structure prevents a complete analysis of all possible aluminum atom locations, and forces the reliance on stochastic methods.

In this study, 64 different Zeolite X structures were created and analyzed. The number of different scenarios was determined via validation against experimental data. These structures

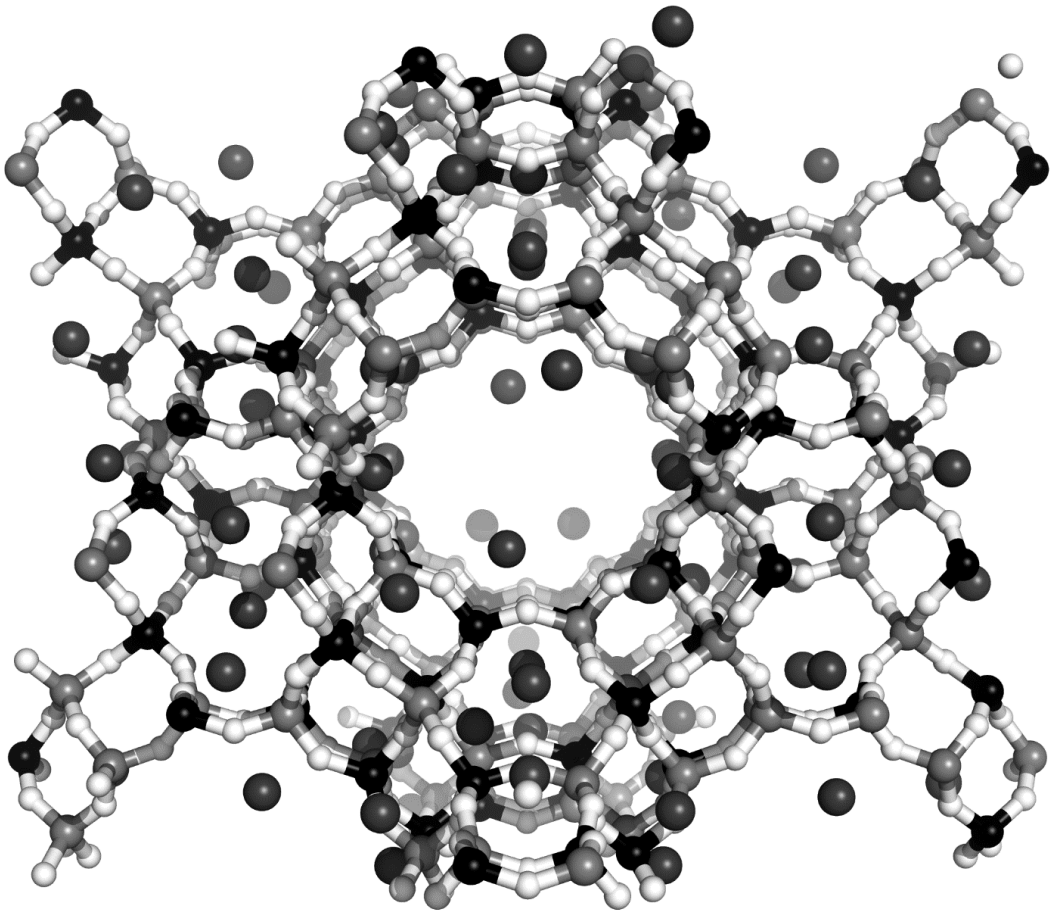

Figure 12: Molecular model of Zeolite 13X.

were created by starting with a zeolite comprised entirely of silicon and oxygen ($Si_{192}O_{354}$), as is shown schematically in Figure 13a, and then aluminum atoms were randomly substituted for silicon atoms in the crystalline structure. These aluminum atom substitutions were performed maintaining Löwenstein's rule [32, 33] as is shown schematically in Figure 13b, and the substitutions were repeated until a Si/Al ratio of 1.23 was achieved. Upon completion of the aluminum substitutions, sodium cations were dispersed throughout the structure to balance the overall charge, and the equilibrium location of these cations was determined via Monte Carlo

methods which are described later. Each of these 64 different Zeolite X structures were then used to simulate—also via Monte Carlo methods—the heat of adsorption and equilibrium adsorption

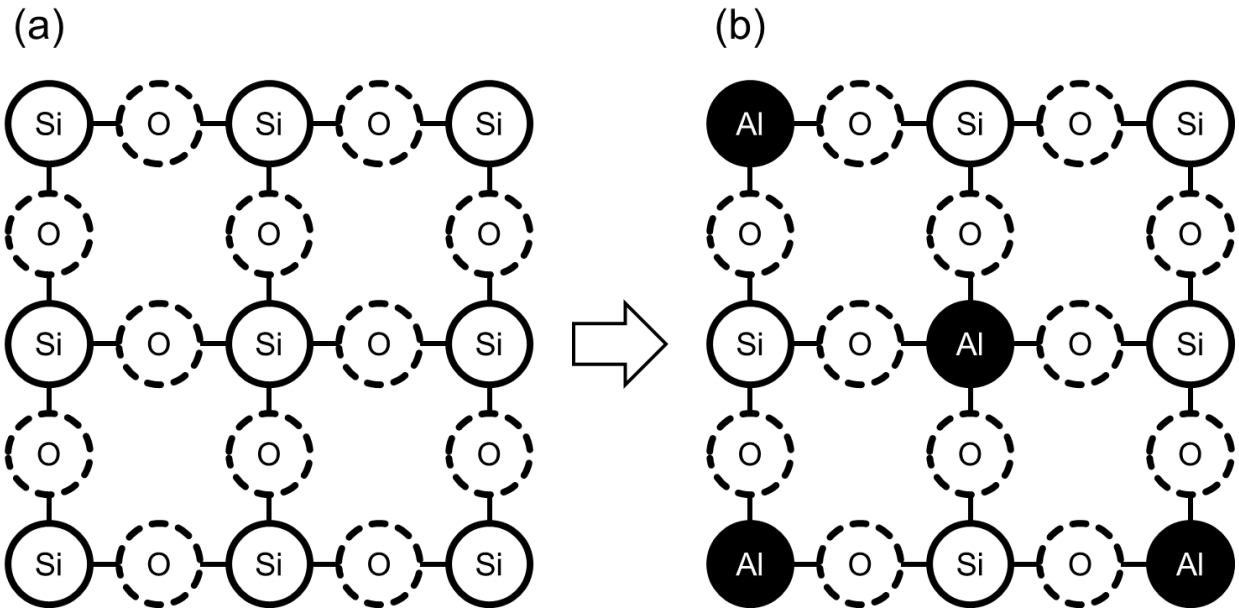

Figure 13: Schematic of aluminum replacement.

across typical pressure and temperature ranges for both methane and propane.

Once the performance properties of the 64 different Zeolite X structures were analyzed for methane and propane, each of the zeolite structures was utilized in a macro-scale adsorption column for the separation of a mixture of either nitrogen/methane or nitrogen/propane. This resulted in 128 different adsorption column simulations, as is shown schematically in Figure 14. For each of these scenarios, the exit mole fraction as a time is measured, and breakthrough curves are generated. Different aluminum distributions results in different adsorption properties, and these different adsorption properties translate into different breakthrough curves for the different adsorbents. These different breakthrough curves have then been compiled via an uncertainty analysis.

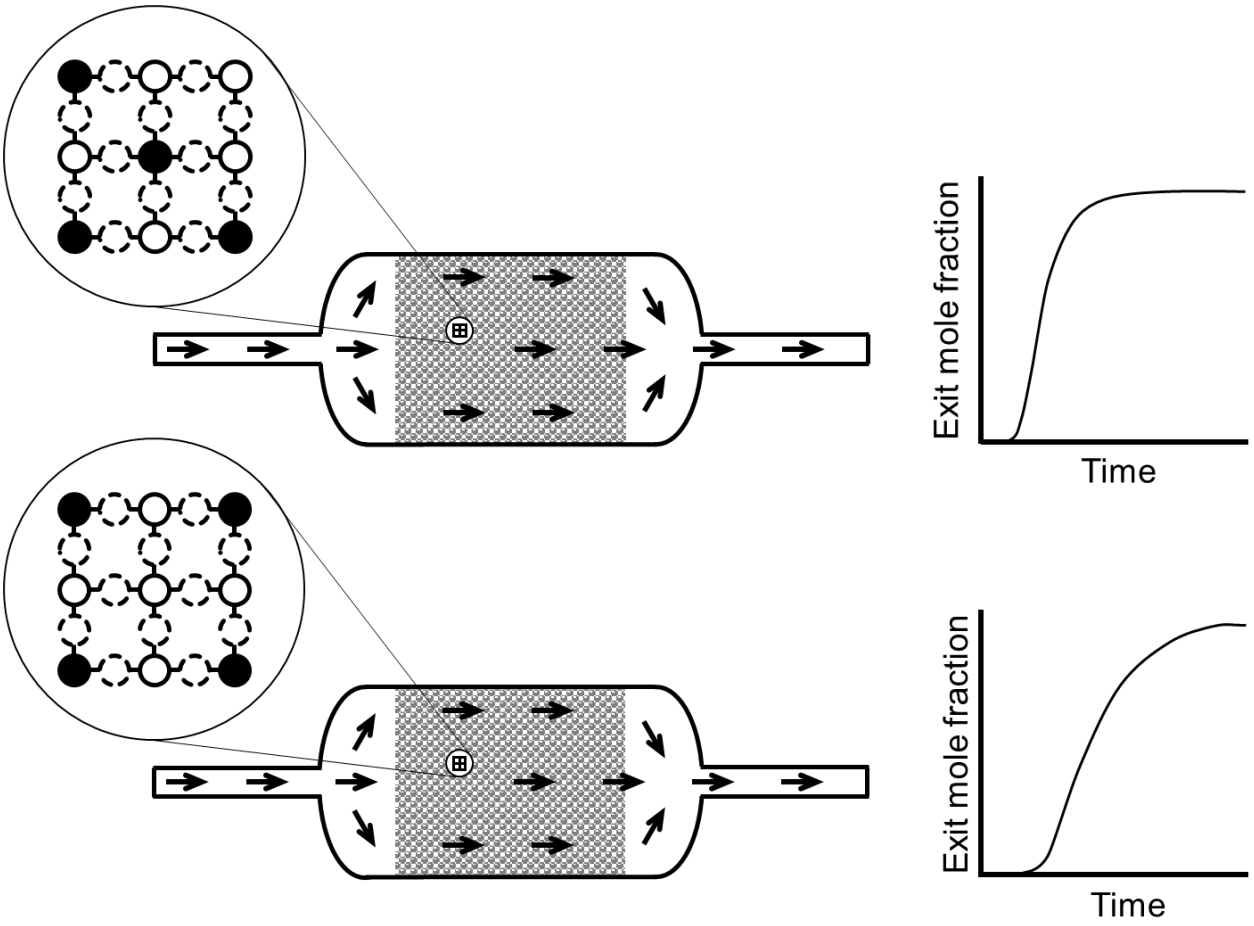

Figure 14: Diagram of stochastic simulations and resultant performance.

3.2.1 Molecular Modeling

For all molecular simulations in this work, the united atom force field for alkanes in zeolites with extra-framework sodium cations developed by Calero et al. [33] was used. This force field approximates hydrocarbon building blocks (i.e. CH_4, CH_3, and CH_2) as single atoms, thus greatly reducing the computational effort while still maintaining a high level of accuracy [35]. In simulating both the heats of adsorption and equilibrium adsorption isotherms, an NPT (where the Number of atoms, Pressure, and Temperature of the system are held constant) Gibbs ensemble was used for a configurational-bias Monte Carlo simulation. A Gibbs ensemble is used to study the interaction of two separate phases by using a separate simulation box for each phase [35]. In the present study, the phases are the bulk gas phase of unadsorbed alkane, and the adsorbed phase in a zeolite framework. A Monte Carlo simulation involves randomly relocating or rotating a molecule in a given system with the intention of minimizing the total system energy [35]. For a Gibbs ensemble, this relocation can either be constrained to a single box, such as a

translation move, or can involve both boxes, such as moving a molecule from one box to another, both with the intent of pushing the system towards equilibrium [36].

The zeolite frameworks were modeled via fixed silicon, oxygen, and aluminum atoms, and mobile sodium cations [33]. Before introducing alkanes into the system, sodium cations in each of the 64 frameworks were allowed to achieve equilibrium through 3×10^7 Monte Carlo steps. Once the zeolite systems had reached equilibrium, alkanes were introduced in the empty box of the Gibbs ensemble. Heat of adsorption was simulated via 5×10^9 additional Monte Carlo moves at very low alkane concentrations, and was calculated using the following relationship [37]:

$$Q = RT - \frac{\langle NU\rangle - \langle N\rangle\langle U\rangle}{\langle N^2\rangle - \langle N\rangle^2} \quad (2)$$

where Q is the heat of adsorption, R is the ideal gas constant, T is the system temperature, N is the number of molecules, U is the energy, and $\langle\,\rangle$ signifies an ensemble average over the simulation run. Equilibrium adsorption isotherms were determined in a similar manner, where 5×10^9 additional Monte Carlo steps were taken after the zeolite cations had reached equilibrium, except that the pressure was controlled by changing the volume of the alkane-only Gibbs ensemble box. Equilibrium adsorption was simulated across the range of temperatures and pressures seen in typical macroscale scenarios.

All Monte Carlo simulations (i.e. heats of adsorption and isotherms) were solved using the Monte Carlo for Complex Chemical Systems (MCCCS) Towhee [38] computational software, developed under the auspices of the U.S. Department of Energy's Office of Industrial Technologies.

3.2.2 Macroscale Modeling

Fixed bed reactors, comprising of vessels with a stationary reactant and moving fluid, are commonly used in adsorption processes. In these reactors, a mixture is introduced into a column full of adsorbent where one component of the mixture is more strongly adsorbed. As the mixture flows through the column, the more strongly adsorbed component is retained and the less strongly adsorbed component passes through the column. The separation process continues until the adsorbent becomes saturated. In this paper, 64 fixed bed adsorption columns—each with a different Zeolite X structure and identical bed geometry—are simulated. The separation of a methane/nitrogen mixture and a propane/nitrogen mixture are analyzed separately.

The computational fluid dynamic model used in this study is described in detail in Chapter 2. This model was chosen due to its rigorous inclusion of physical phenomena as well as its basis on commercially available pressure vessel geometry. Specifically, this model simulates the

reactive region of the fixed bed as a laminar, two-dimensional, nonadiabatic, nonisothermal, bidispersed, linear driving force adsorptive system, and models the open regions of the reactor via the re-normalization group (RNG) turbulence model. The reactive regions is treated as laminar due to the low Reynolds numbers seen in this porous flow, and two-dimensional due to the axisymmetric geometry of the adsorption column. The nonadiabatic and nonisothermal assumptions are necessary due to the fact that adsorption is an exothermic process. The bidispersed linear driving force adsorption modeling scheme accounts for the non-uniform composition of zeolite pellets: zeolite crystals are bound together with a porous, non-reactive binder. The open regions are modeled with the RNG turbulence model, as this model was shown in Chapter 2 to provide the best approximation of a Large Eddy Simulation of the identical scenario. For all simulations, an 8-inch axial flow reactor with a gas mass flowrate of 0.001 kg/s was used.

In these simulations, a mixture of methane/nitrogen or propane/nitrogen is introduced at the inlet of the column at time zero. Both inlet mixtures are comprised of an alkane mole fraction of 0.015. Initially, the column has no alkane present, either within or outside of the zeolite and is full of inert nitrogen. The simulation is performed from time zero—when the mixture is first introduced into the column—until the exit mole fraction is equal to the inlet mole fraction of alkane. All macroscale simulations are performed with ANSYS 12.1 Fluent, relying on user-defined functions for adsorption-related phenomena.

3.3 Results and Discussion

Multiscale simulations, incorporating molecular-level uncertainty, have been performed in an effort to quantify macroscale adsorption system uncertainty. At the molecular scale, a stochastic approach has been taken to simulating the heat of adsorption and the equilibrium adsorption loading of Zeolite X for methane and propane. Using these stochastic parameters, macroscale computational fluid dynamics (CFD) simulations have been performed for fixed bed adsorption systems, and properties at the exhaust of these beds have been measured. The results of these measurements have then been analyzed, and the macroscale system uncertainty has been quantified.

The first of the performance properties analyzed is the heat of adsorption for methane and propane on Zeolite X, and the results of this analysis are shown in Figure 13a and Figure 13b respectively. In both figures, the cumulative density function (CDF) of experimental results [39-58] are shown via a dashed line, and compilation of computational results, determined using Equation 2, are shown via a solid line. The experimental results have been collected from a diverse

range of sources, spanning labs across countries and experiments across decades. This range of experimental data is necessary to account for the wide range of crystalline structures possible in the zeolite manufacturing process.

As can be seen from Figure 15a, there is excellent agreement between the computational and experimental stochastic results for methane on Zeolite X. In contrast, the mean computational result for propane corresponds to the mean experimental, but the variance is far greater for the computational results. This disparity is due to the more limited experimental results available for propane: as would be expected from a limited sample, the variance is artificially small, and this is clearly demonstrated in Figure 15b. For a larger experimental sample, it would be expected that better agreement would be observed. This disparity between Figure 15a and Figure 15b highlight one of the chief benefits of a stochastic computational approach to quantifying uncertainty: it is time-consuming and expensive to run a sufficient number of experimental samples to capture the stochastic distribution of a given parameter, but relatively straightforward to do so via computational means.

Upon further consideration of Figure 15, it can be seen that the heat of adsorption of methane is lower than that of propane. As the heat of adsorption is closely related to the heat of vaporization—where an adsorbed gas has similar properties to a liquid—the heats of vaporization follow the same trend as the heats of vaporization: the heat of adsorption of propane is greater than that of methane. Additionally, it can be seen that the relative variance of the heat of adsorption for methane is greater. This is due to the fact that the adsorption of methane is more affected by the location of non-framework cations, and thus the location of aluminum atoms. At near-ambient temperatures and pressures—where these particular adsorption processes commonly take place—the van der Waals forces between propane molecules are far more substantial than that of methane. Therefore the intermolecular interactions of propane with other propane molecules play a significant role in adsorption, and the interactions between cations and propane molecules is not the only driving force. In contrast, the van der Waals forces between

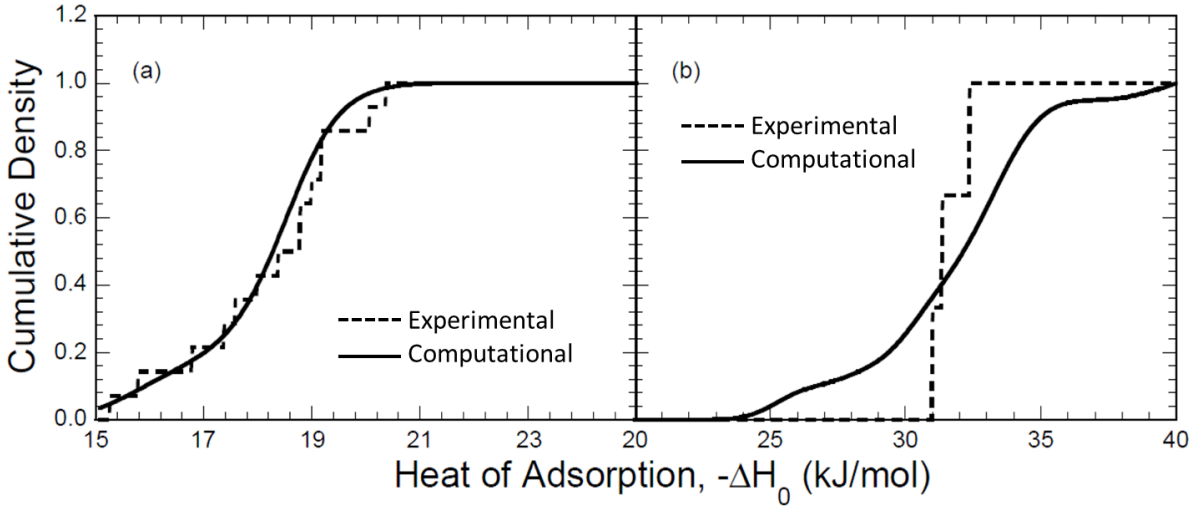

Figure 15: Stochastic heat of adsorption for (a) methane and (b) propane on Zeolite 13X.

methane molecules are relatively small, and nearly all of the intermolecular potential in methane/Zeolite X adsorption is the result of cation locations.

Figure 16 and Figure 17 present adsorption isotherms—the equilibrium adsorption loading at a constant temperature across a range of pressures. Although both methane and propane were simulated across a range of temperatures, the isotherm presented for methane, at 330 K, and for propane, at 293 K, have been chosen to correspond to the available experimental data. In both figures, the solid line represents the mean computational isotherm, and the dashed lines represent plus/minus three standard deviations. Experimental results are denoted by the markers labeled in each plot [43, 50, 53, 54, 59].

In both figures, it can be seen that adsorption loading—represented via the number of molecules per unit cell of adsorbent—increases with pressure, but asymptotically levels out at higher pressures. This increase follows intuition, similar to a pressure vessel holding a greater number of molecules at higher pressure, and the leveling is on account of the adsorbent becoming saturated. It can also be seen that the same quantity of adsorbed methane molecules requires a higher pressure that that for propane. This is due partially to the higher temperature, which decreases the equilibrium adsorption in a similar manner to how increased temperature reduces condensation. But temperature is not the primary source of this disparity, rather the trivial intermolecular forces between methane molecules compared against propane molecules drives

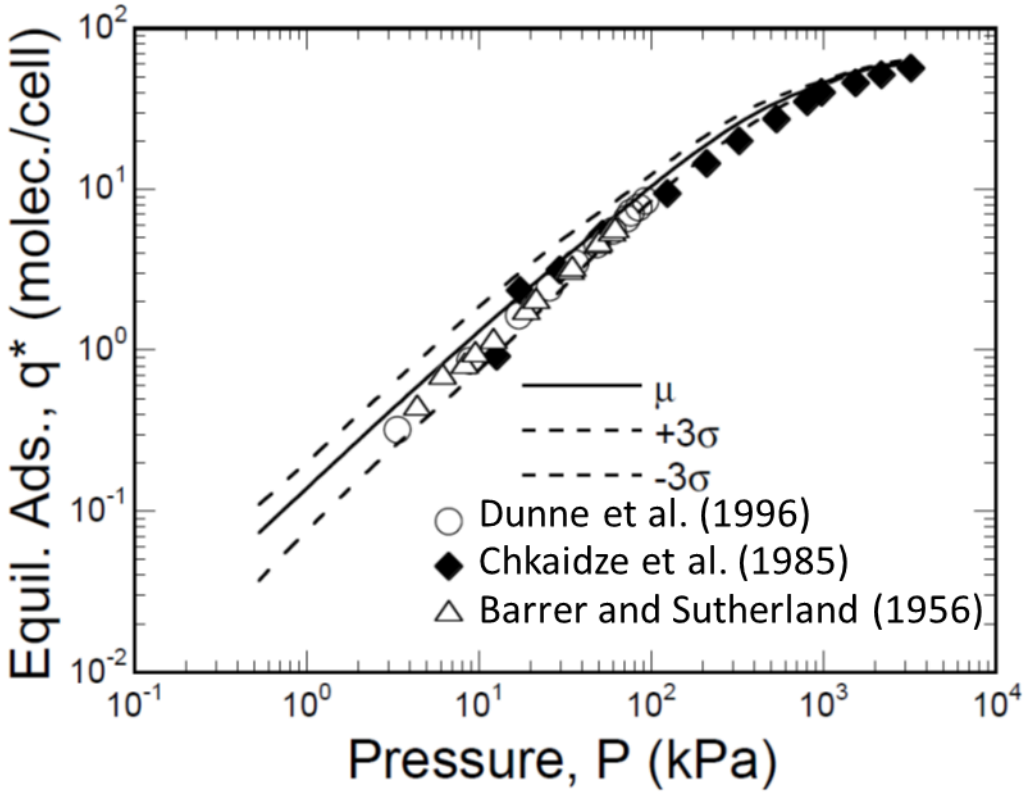

Figure 16: Stochastic adsorption isotherm for methane over Zeolite 13X.

this difference: because of the higher intermolecular forces between propane molecules, there are multiple sources of attraction at each adsorption site for propane (zeolite-propane attractions *and* propane-propane attractions). Additionally, as would be expected due to the size difference of methane and propane molecules, a slightly higher quantity of methane molecules can be adsorbed at saturation.

For both adsorption equilibrium scenarios, the computational results include a small amount of over-prediction at higher pressure. This is likely due to pore-blocking, where alkane molecules get overcrowded in bottlenecks within the zeolite structure, and prevent the zeolite from becoming fully saturated. By simulating adsorption via Monte Carlo methods, the specific trajectory of molecules is not tracked, and pore-blocking does not hinder adsorption. For Monte Carlo simulations, the positions of molecules are randomly assigned with each time step, so it is possible for molecules to "jump" past a bottleneck. In experiments, molecules follow trajectories, and can be hung up at constrictions within the crystalline framework.

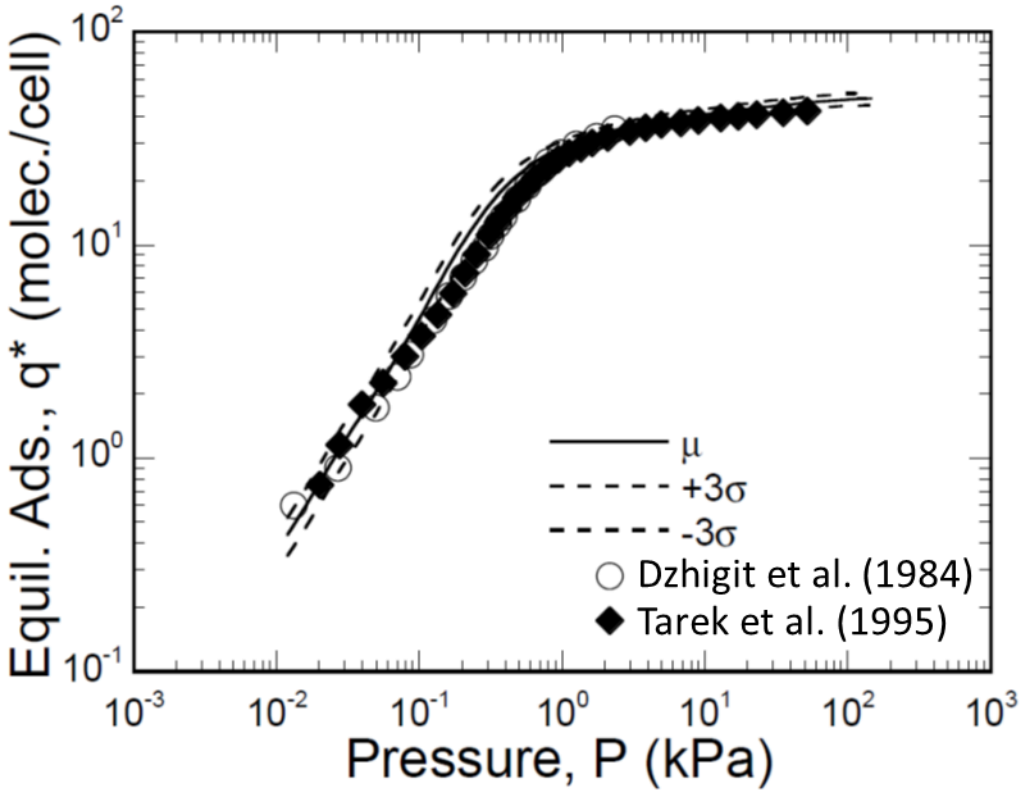

Figure 17: Stochastic adsorption isotherm for propane over Zeolite 13X.

The heat of adsorption and equilibrium loading both have effects on the macroscale performance of fixed bed zeolite systems. As the equilibrium adsorption is reduced at higher temperatures, the heat of adsorption—the amount of heat released upon a molecule being adsorbed—affects the overall amount of molecules that can be adsorbed. Variability in the equilibrium adsorption itself determines how much separation can actually be performed by a given adsorption column: a higher equilibrium adsorption results in greater adsorbent capacity and thus greater separation potential.

These effects of molecular variability on macroscale performance are presented for the methane/Zeolite X system in Figure 18. Breakthrough curves for all 64 methane scenarios are shown as solid black curves. The uncertainty in breakthrough times span hundreds of minutes, and could result in drastically different system throughputs depending on specifically what zeolite structure has been utilized. This significant uncertainty for the breakthrough curves is due primarily to the significant uncertainty in the equilibrium adsorption for methane. This enormous variability will have significant effects on the overall performance of a methane separation

system, and identifying a means of reducing this uncertainty—such as extensive testing and selection of zeolite batches—is desirable.

The impact of this uncertainty will manifest in a variety of different manners. For the leftmost curves in Figure 18, where the methane breaks through the fastest, the corresponding adsorption systems have the lowest adsorption capacity. Because of their lower capacity, they become saturated more rapidly, and methane breaks through in less time. On account of a lower capacity, it is necessary to purge these adsorption columns more frequently. The process of purging an adsorption column—and reducing the amount of methane adsorbed so that a fresh separation process can begin—requires time and energy, thereby increasing the cost of operation. Therefore,

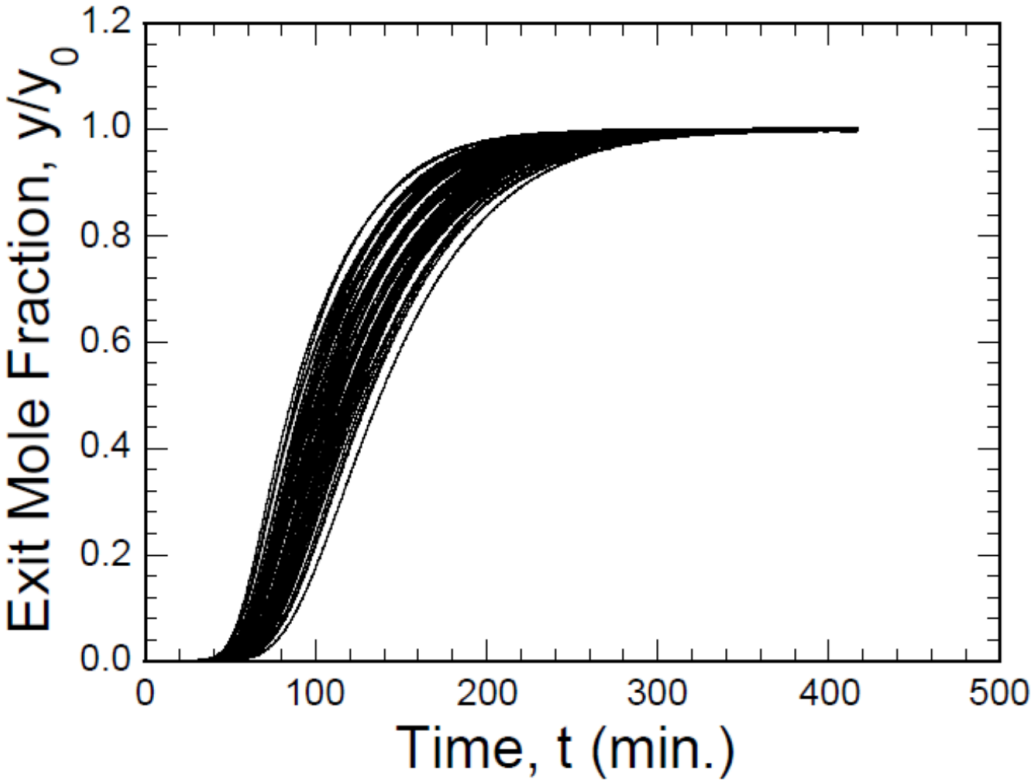

Figure 18: Breakthrough curve for methane over Zeolite 13X.

these columns and the specific zeolite structures could potentially be more expensive to operate than the columns corresponding to the rightmost curves in Figure 18.

But capacity is only one metric for evaluating a breakthrough curve. It is also desirable to have a sharp rise in exit mole fraction over a short time, with the ideal scenario comprising of a step change from no methane to the inlet fraction of methane. In contrast, a gradual increase in a breakthrough curve will result in unwanted methane exiting the column prior to the column

achieving saturation. For the scenarios shown in Figure 18, the leftmost curves have a sharper transition than the gradual curves in the rightmost scenarios. Therefore, the rightmost curves could potentially provide a lower purity than the leftmost curves.

The performance of propane separation is markedly different than that of methane. As can be seen in Figure 19, the disparity between the breakthrough curves for propane on different Zeolite 13X structures is negligible. This is to be expected, as the variance for propane equilibrium adsorption from Figure 17 was trivial. The source of this limited variability ultimately stems from the significant role that propane-propane intermolecular forces play, thereby mitigating the effects of the cations.

For both the methane and propane scenarios, the variability in adsorption isotherms played the most significant role in the macroscale variability of the corresponding adsorption columns. As both the heat of adsorption and macroscale computational analyses require a substantial amount of effort, particularly for generating stochastic results, it is recommended that future analyses focus primarily on the adsorption isotherms for determining whether macroscale performance variability is a concern.

Overall, this study illuminates the outcomes of uncertainty analysis for two similar scenarios, with one involving a substantial amount of uncertainty and one involving a relatively minor amount of uncertainty. Capturing this behavior is necessary to assure consistent and reliable performance of zeolite systems.

3.4 Conclusions

Zeolites are widely used in commercial separation and catalysis, and many of the performance properties of these adsorbent crystals are driven by the molecular-level distribution of aluminum atoms. As it is not currently feasible to ascertain the locations of these atoms for certain zeolite configurations, it is necessary to rely on computational methods. But, due to the inherent variability in aluminum locations, these computational methods need to rely on stochastic tools in order to accurately capture the performance properties of the zeolites.

This paper provides an approach to identifying molecular variability in Zeolite X, accounting for the effects of this variability on the adsorption of methane and propane, and propagates this uncertainty to the behavior of zeolites in macroscale fixed bed adsorption columns. The results of this study highlight the value of this uncertainty analysis: for methane, the uncertainty is significant and plays a role in the overall system performance, but for propane, the uncertainty is negligible. By highlighting scenarios where uncertainty is a dominant factor, it is possible for system performance to be more readily predicted and optimized.

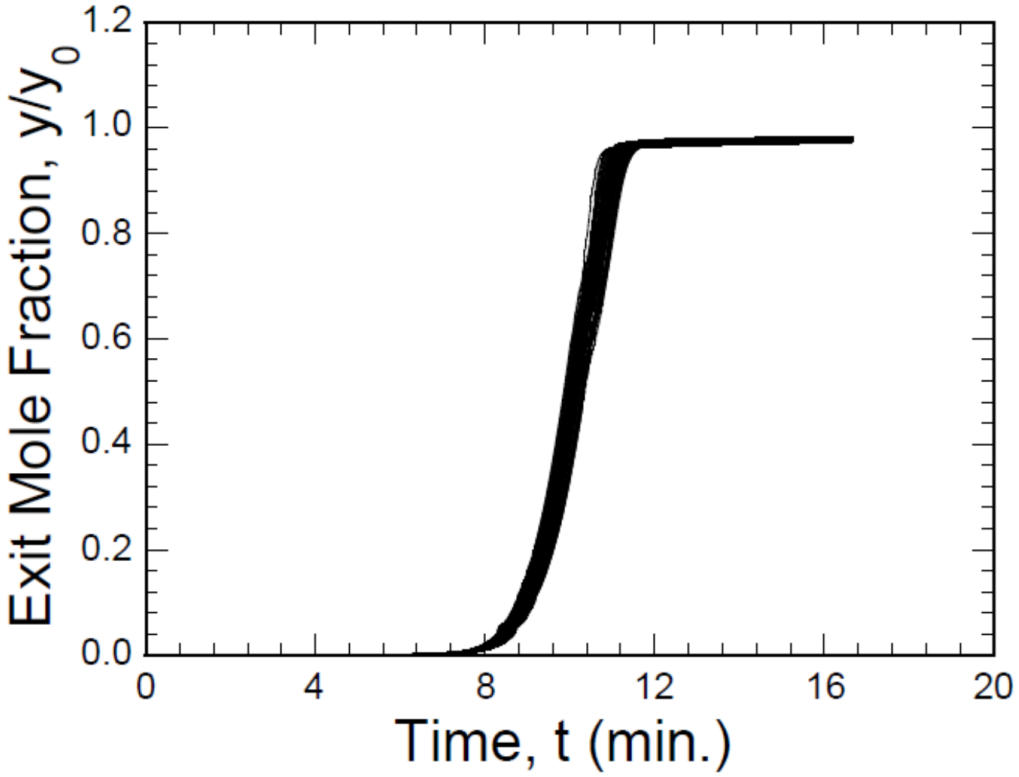

Figure 19: Breakthrough curve for propane over Zeolite 13X.

Chapter 4: QUICKER: Quantifying Uncertainty In Computational Knowledge Engineering Rapidly—A Rapid Methodology for Uncertainty Quantification

Most engineering systems have some degree of uncertainty in their input parameters, either of a stochastic nature or on account of a lack of complete information. The interaction of these uncertain input parameters, and the propagation of uncertainty through engineering systems, leads to the stochastic nature of the system performance and outputs. Quantifying the uncertainty in an experiment or computational simulation requires sampling over the uncertain range of input parameters and propagating the uncertainty through a computational model or experiment to quantify the stochastic output parameters. Conventional direct sampling methods for input uncertainty propagation, such as Monte Carlo Sampling or Latin Hypercube Sampling, require a large number of samples for convergence of the statistical parameters, such as mean and standard deviation, and can be prohibitively time-consuming. This computational tedium has been partially eliminated through the use of meta-models, which approximate a computational simulation or experiment via a response surface, but the computational time savings from these models often comes at the expense of accuracy. Toward addressing the challenge of input uncertainty propagation, this chapter presents a new sampling methodology, QUICKER: Quantifying Uncertainty In Computational Knowledge Engineering Rapidly, that can reduce sample sizes by orders of magnitude while still maintaining comparable accuracy to direct sampling methods. In this chapter, the QUICKER methodology is described and demonstrated with both analytical and computational scenarios.

4.1 Introduction

Some degree of uncertainty is inherent in most engineering systems [60-65] due to variability in environment, operating, or material parameters, or due to limited knowledge or lack of knowledge about some of the parameters. These uncertainties can propagate through the system, resulting in uncertainty in the performance of a system. In order to account for the uncertainty in computational models, it is necessary to simulate the entire range of possible uncertain inputs, often through a direct sampling technique.

Two of the most commonly used conventional direct sampling methodologies are Monte Carlo sampling and Latin Hypercube sampling [66, 67]. In a Monte Carlo sampling input values are randomly selected from the given input distributions with the probability that each value occurs equally. Although this method is simple, the purely random nature of the sampling does

not ensure covering the full distribution. As a result, it requires a relatively large number of samples to ensure that the entire design space has been captured. Thus, Monte Carlo sampling can be very costly in terms of computational time and effort due to the relatively large number of samples required for convergence.

The limitation on the poor convergence of the mean and variance of Monte Carlo sampling, arising from its purely random sampling of the uncertain input distributions, can be overcome with a stratified approach such as Latin Hypercube sampling [67, 68]. In this method, each input's statistical distribution is broken up into equiprobable intervals (strata), where the number of strata corresponds to the number of samples required, and then one sample point is randomly selected from within each interval. By virtue of the stratification of the input distribution, this method requires fewer samples than Monte Carlo sampling to cover the entire range of inputs [69]. Despite the improvement over Monte Carlo sampling, the Latin Hypercube sampling method still requires a relatively large number of samples for convergence of the mean and standard deviation of the output distribution [61, 70]. Therefore, for detailed computational multiphysics simulations that require days, weeks, or months to complete, both Monte Carlo and Latin Hypercube sampling methods are typically prohibitively expensive due to the number of simulations necessary to run.

Other, less common, direct sampling methodologies include the Halton and Hammersley methods, Centroidal Voronoi Tessellation sampling, and Importance and Umbrella sampling. The Halton and Hammersley methods rely on deterministic sequences to generate a set of points across a sample space that is roughly uniform, with the primary difference between the two methods being the specific sequence used [71]. For the Halton method, the deterministic sequence is defined by dividing the interval (0, 1) into fractions based on prime numbers. For example, for a sequence based on 2, the indices of the sequence are converted into binary—base two—to initially yield a sequence of 1.0, 10.0, 11.0, 100.0, 101.0… Then, these numbers are reversed about the decimal point to yield 0.1, 0.01, 0.11, 0.001, 0.101… Finally, the numbers are converted from base 2 back to base 10 to yield the sequence $\frac{1}{2}, \frac{1}{4}, \frac{3}{4}, \frac{1}{8}, \frac{5}{8}, \frac{3}{8}, \frac{7}{8}, \frac{1}{16}, \frac{9}{16}, \ldots$ For a sequence based on 3, the interval is divided via base 3, resulting in $\frac{1}{3}, \frac{2}{3}, \frac{1}{9}, \frac{4}{9}, \frac{7}{9}, \frac{2}{9}, \frac{5}{9}, \frac{8}{9}, \frac{1}{27}, \ldots$ To create a two-dimensional set of sampling points, the first two sequences are paired up to give $\left(\frac{1}{2}, \frac{1}{3}\right), \left(\frac{1}{4}, \frac{2}{3}\right), \ldots$ Hammersley sampling is similar, except that the first sequence is found by dividing the index of the sample point by the total number of sample points (e.g. for a variable with 100 samples $\frac{1}{100}, \frac{2}{100}, \frac{3}{100}, \frac{4}{100}, \frac{5}{100}, \ldots$). A Hammersley sample for additional dimensions simply uses the Halton

sequence, so a three-dimensional Hammersley sample, for 100 samples from each variable, would take the form $\left(\frac{1}{100}, \frac{1}{2}, \frac{1}{3}\right), \left(\frac{2}{100}, \frac{1}{4}, \frac{2}{3}\right), \ldots$

Voronoi Tessellation, another direct sampling method, starts with a predefined set of points in a given region, and then divides the region into volumes such that each volume consists of space that is closest to a given point. Centroidal Voronoi Tessellation is a variation on Voronoi Tessellation that requires each of the predefined points to be at the center of mass of the surrounding volume. As the name implies, Centroidal Voronoi Tessellation sampling relies on this concept to generate sample points [72]. Importance and Umbrella methods rely on sampling from a statistical distribution, other than the physically-determined distribution, that has been modified to put more weight on the samples of higher "importance" [73]. Although all these methods typically require far fewer samples than traditional Monte Carlo methods, they still require a significant number of samples to achieve convergence, and are still prohibitive for many computational simulations.

When direct sampling methods are too computationally intensive, another approach commonly used in uncertainty analysis is to create a meta-model, or surrogate, as an approximation of the full-scale computational simulation [74-77]. Meta-models are designed to be simpler, and thus faster to sample from, than the full-scale model. These models are built by collecting a relatively small number of samples, or "training data", from the full-scale model, and then using regression analysis to fit a response surface to the results.

The most popular regression technique is the use of least-squares regression to fit a low-order polynomial function to the sampled data [74, 76]. This technique is appealing on account of its simplicity, but is inherently limited by the assumption that the response surface can be accurately modeled by a low-order polynomial. This functional form limitation is shared by all parametric meta-modeling techniques [77]. In response to this limitation, a wide variety of non-parametric meta-modeling methods have been developed that make fewer assumptions about the shape of the response surface, including Multivariate Adaptive Regression Splines (MARS), Artificial Neural Networks (ANN), Gaussian Process (GP), and Radial Basis Function (RBF). MARS relies on an iterative method to fit splines to different regions of the response surface, effectively creating localized linear response fits [78]. Although MARS has been shown to be quite accurate, it requires a larger number of training data points than many other non-parametric methods [77]. Artificial Neural Networks involve a system of networked elements that are weighted based on training data [79]. This regression method also requires a large amount of training data, and work has been done in an effort to create a hybrid combination of neural networks and polynomial

functions that would reduce the amount of training data [80]. A Gaussian Process is analogous to a Gaussian distribution, except that instead of describing random variables, it describes functions [81]. Gaussian Process regression assumes that a Bayesian prior can be represented via a Gaussian process. This technique is quite versatile, but can be very computationally expensive for large training datasets [74]. Radial Basis Function regression relies on a linear combination of radially symmetric functions. RBF regression is typically one of the most accurate regression techniques for small sample sizes [77].

Although these meta-models have seen a great deal of success in the literature, they all have all two inherent limitations. The first is based on the assumption that the response surface is smooth [82]. In order to use a meta-model to interpolate the behavior of a system in between data sampled from the full-scale model, it is necessary to assume that there is a smooth transition between data points. For many situations, this is a valid assumption, but in scenarios involving phenomena such as phase changes, shock waves, buckling, etc., there will not be a smooth transition, and without a very large amount of training data, a meta-model will not provide a good approximation. The second limitation is that these methods scale poorly. Typically the required number of full-scale samples scales exponentially with the dimensionality of the problem (e.g. the number of uncertain inputs) in order to fill the entire design space [76]. This limits meta-models to relatively low-dimensional uncertainty analysis scenarios.

In response to the limitations of sampling from meta-models, Mawardi and Pitchumani developed a technique, known as Stochastic Analysis with Minimal Sampling (SAMS) [61]. This technique relies on using a very small number of training points to construct a low-order polynomial meta-model via least squares regression. Next, instead of sampling from the meta-model as the previously described techniques do, the meta-model is used to determine the location, shape, and shift parameters for a functional form of an assumed output distribution. This technique mitigates some aspects of the limitations of conventional meta-model sampling, but it requires an additional assumption be made about the output distribution *a priori*. It is also limited by the assumption that the response surface can be represented by a low-order polynomial.

Toward overcoming the drawbacks of existing uncertainty analysis approaches, while also requiring far fewer samples than direct sampling methods, a methodology termed QUICKER—Quantifying Uncertainty In Computational Knowledge Engineering Rapidly—is presented in this chapter to be generally applicable to both smooth and discontinuous scenarios and to scale as $O(n)$ where n is the number of uncertain input parameters (e.g. the dimensionality of the

problem). The QUICKER methodology does not rely on a meta-model; instead, it uses the full-scale simulation to generate the three parameters necessary for multiple superimposed modified-lognormal distributions. By superimposing multiple distributions, it is possible to account for discontinuities where meta-models would require a smooth surface. By relying on the full-scale simulation to generate output parameters, the need to generate a complete response surface across multiple dimensions has been removed, and it is possible to scale the methodology to large numbers of uncertain input parameters.

In this chapter, the QUICKER methodology is applied to models with simple functional relationships as well as computational models of particulate multiphase systems to illustrate the approach on a range of models. The QUICKER methodology is compared with existing methods for uncertainty analysis in the literature namely, Monte Carlo and Latin Hypercube direct sampling methods, a Gaussian Process with a squared exponential kernel, multiquadratic Radial Basis Function meta-models, and SAMS. It is shown that QUICKER reduces the number of samples—and computational times—by over 95% when compared with Latin Hypercube direct sampling methods, and while maintaining accuracy even when Gaussian Process and Radial Basis Function meta-models and SAMS cannot accurately capture the behavior of a system.

The chapter is organized as follows: the steps in the QUICKER methodology are explained in Section 4.2; the models considered in the analysis under uncertainty are introduced in Section 4.3; and the results of the study are presented and discussed in Section 4.4.

4.2 QUICKER Methodology

4.2.1 Overview of QUICKER methodology and comparison with other methods

A comparison of conventional meta-modeling, SAMS, and the QUICKER methodology are shown in Figure 20. All three techniques will be applied to the same scenario, and the advantages of each method will be discussed.

The steps for a conventional meta-model uncertainty analysis for a single uncertain input and output are shown schematically in Figure 20a, b, and c. Figure 20a presents an uncertain input distribution via a normally distributed histogram, representative of how meta-models are typically sampled from via a Monte Carlo sampling approach. The meta-model itself is shown in Figure 20b, where the "+" symbols represent training data that was directly sampled from the full-scale simulation. Typically meta-models are built from non-intrusive direct sampling, and the full-scale simulation is treated as a "black box". The dashed lines in Figure 20b are the meta-model that has been trained to the sampled data. Note that this particular scenario would be

challenging to approximate with a meta-model due to the large discontinuity. Lastly, Figure 20c presents the results of applying the meta-model to the input distribution.

There are multiple means of validating a meta-model, and the three most commonly used

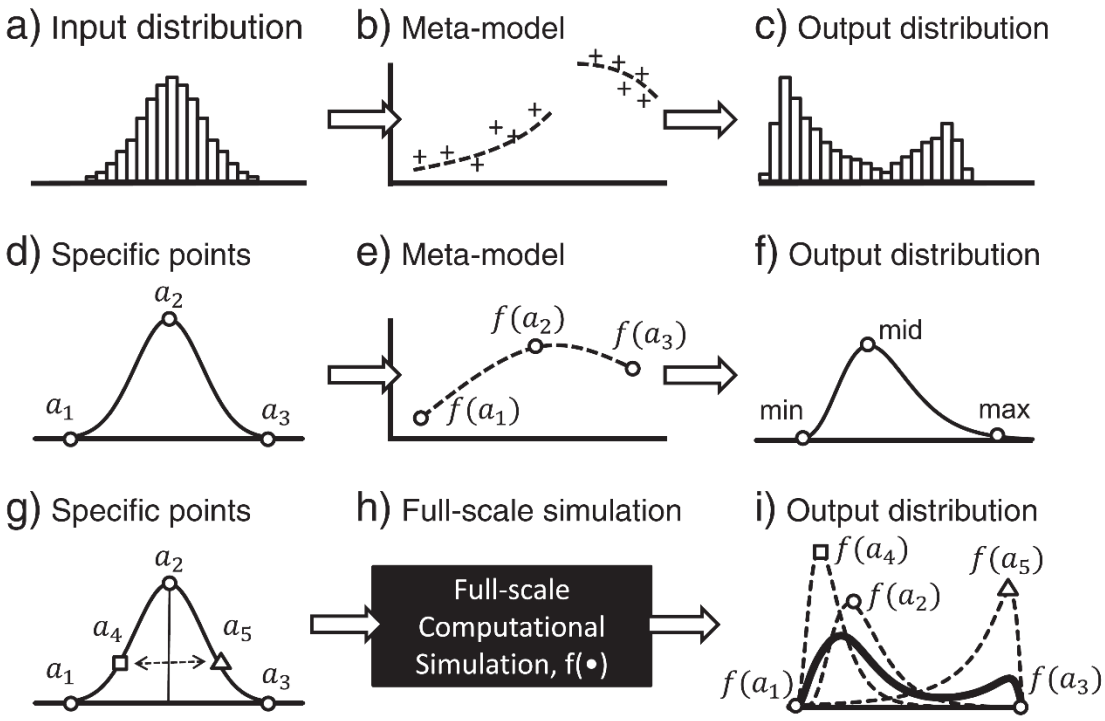

Figure 20: Schematic of the foundational steps of (a, b, c) meta-modeling methods (first row), (d, e, f) SAMS method (second row), and (g, h, i) the QUICKER methodology (third row).

methods are bootstrap, cross-validation, and holdout [83, 84]. In all three techniques, the objective is to use a meta-model to predict results not used in the creating of the meta-model. Bootstrapping and cross-validation both rely on using available data for both training and validation at different points in the process. Holdout validation reserves a portion of the data exclusively for validation, and while it is the most computationally expensive, it also provides the most accurate results [83, 84].

In Figure 20d, e, and f, the steps for the SAMS method are presented schematically. In meta-modeling, the shape of the input distribution is not typically used to determine training data points, but in SAMS it is. Figure 20d presents the three specified points, the mean and plus/minus 3 standard deviations from the mean (shown in Figure 20d as a_2, a_3, and a_1 respectively), which will be used to sample from the full-scale simulation and then used to build the meta-model. As with the meta-model approach in Figure 20b, the full-scale simulation is sampled non-intrusively,

and thus treated as a black box. The outputs of the three sample points identified in Figure 20d are used to build a meta-model, and the results of running these samples through the full-scale simulation are presented as $f(a_2)$, $f(a_3)$, and $f(a_1)$ for the results of the mean and plus/minus three standard deviations respectively. Note that this meta-model in Figure 20e is attempting to approximate the same scenario shown in Figure 20b, but has assumed that a meta-model could be accurately built with only three training points. For simpler scenarios, this would reduce the number of samples necessary, but for challenging scenarios, some aspects of the output distribution are lost. Lastly, the minimum, median, and maximum of the *meta-model* are used to determine the three parameters necessary to fully locate a given output distribution, assumed *a priori* to be lognormal in this scenario. As can be seen in Figure 20f, the second mode is not captured by the SAMS technique. No recommended for of validation for SAMS was provided in Ref. [61], but any of the three methods used for meta-models (bootstrap, cross-validation, or holdout) could be used to validate the meta-model used in SAMS.

The QUICKER methodology is a further deviation from meta-modeling methods, and builds off of some aspects of the SAMS methodology. As with SAMS, the first step in the QUICKER method is to identify specific sample points. In addition to the three points used in SAMS, two perturbations of the mean, a_5 and a_4, have been included at plus/minus 1.5 standard deviations in Figure 20g. By including these additional points, it is possible to explore localized system behavior as well as global behavior, which will allow the QUICKER method to capture both output modes. Once these five points are identified, they are run through the full-scale simulation, shown as a black box in Figure 20h. Note that no meta-model has been constructed. The results of running the specified input points through the full-scale model are shown in Figure 20i as $f(\cdot)$, and are used to determine parameters for three component modified-lognormal distributions (details of the modified-lognormal distribution will be presented in Step 5 of Section 4.2.2). Each of these component modified-lognormal distributions, shown as dashed lines in Figure 20i, are then averaged into a composite output distribution, shown as a bold line in Figure 20i.

The overall principle of validating the QUICKER methodology is slightly different than that of the meta-models methods. Because QUICKER only produces the likelihood of a given output value, not a response surface as a function of input values, it is necessary to use a "goodness of fit" test to evaluate the accuracy of the QUICKER output. Cross-validation, bootstrapping, and holdout validation methods will still work, but it is recommended that the Anderson-Darling

goodness of fit test [85] instead of metrics commonly used for meta-models, such as adjusted R^2 or Akaike's information criterion [86].

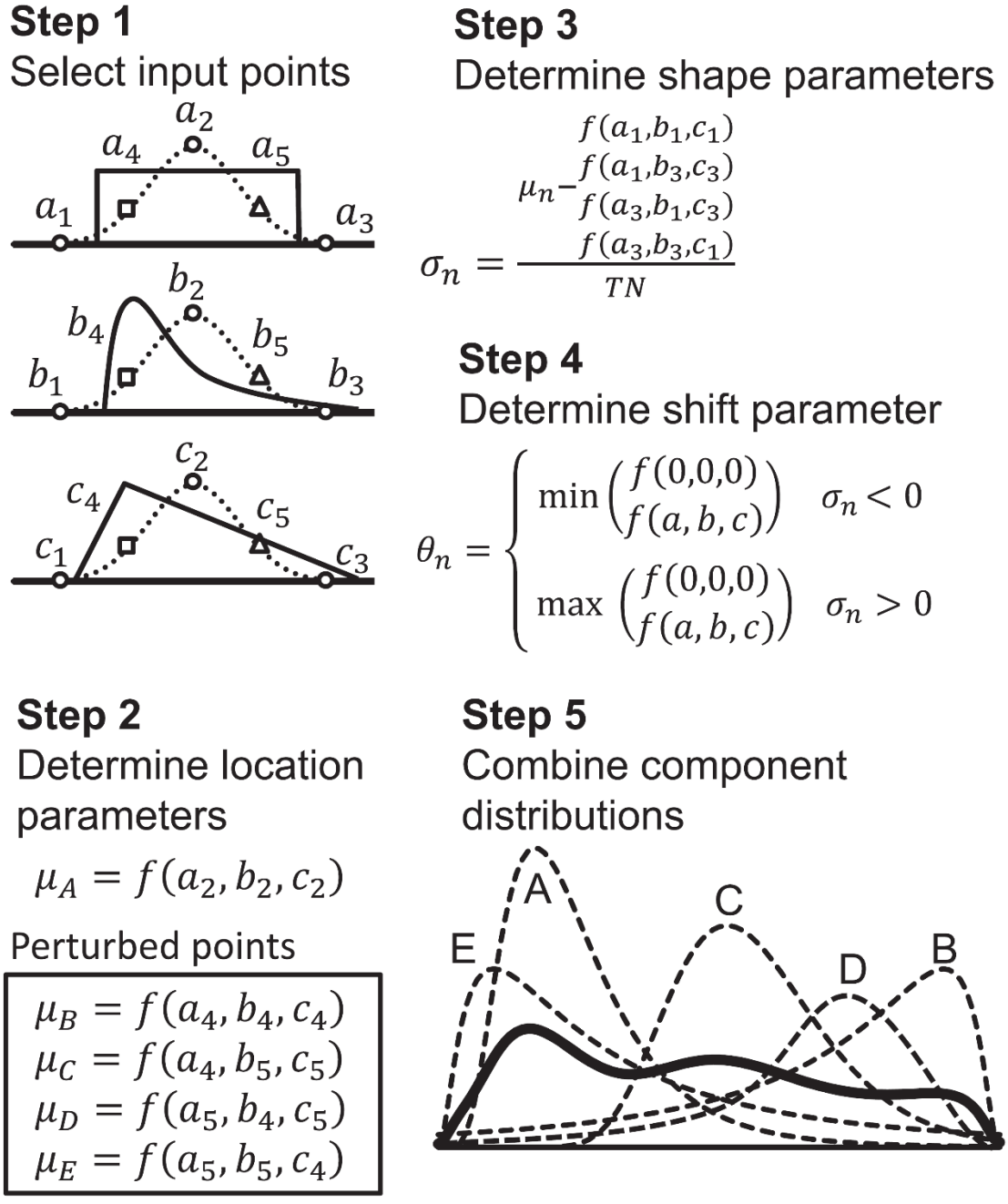

Figure 21: Schematic of the steps in the QUICKER procedure.

The primary difference between QUICKER other methods is the lack of a meta-model. Meta-models are inherently an approximation of a given system, and *a priori* assumptions must be

made about the nature of these models (e.g. assuming smoothness). In contrast, QUICKER makes assumptions about the nature of the output distribution. Both QUICKER and meta-models require assumptions at some point in the uncertainty analysis process, but since the meta-model surface is typically far more complicated than the output distribution (for instance, the output distribution is typically one-dimensional whereas meta-models are often multi-dimensional), it is often easier to generate an accurate approximation of the output distribution.

4.2.2 Implementation of the QUICKER methodology

The primary objective of the QUICKER methodology is to determine the three defining parameters (location, μ; shape, σ; and offset, θ) for each of the component distributions. The specific implementation of the QUICKER methodology is described in five steps as follows, and an example scenario is shown in Figure 21 and will be used for reference:

Step 1: *Select input points.*

The first step in the QUICKER methodology, as is shown in Step 1 of Figure 21, is the selection of five values for each of the input parameters. These values are the mean (regardless of whether the input distribution is Gaussian), shown as a_2 for the first parameter in Step 1 of Figure 21, lower and upper extremes at N standard deviations from the mean, a_1 and a_3 respectively, and two perturbations of the mean located at $\frac{N}{2}$ standard deviations from the mean, a_4 and a_5. This process is repeated for each of the input parameters (e.g. b and c).

Step 2: *Determine the location parameters.*

The second step, as is shown in Figure 21, is to determine the location parameters for each of the component curves of the output distribution. The first location parameter, listed as μ_A in Step 2 of Figure 21, is determined by running the mean value for all of the inputs through the full scale simulation, identified as $f(a_2, b_2, c_2)$ in the figure. This location parameter will be used to define curve "A" in the final step. An orthogonal array is then used in lieu of a full factorial analysis to reduce the number of samples necessary, while still covering the design space *evenly*, for determining the location parameters from the perturbed points. The location parameters determined from the perturbed points will be used to define curves "B", "C", "D", and "E" in the final step.

The example in Figure 21 employs an L4 orthogonal array [87] (where the 4 describes the number of rows in the array) with a strength of two, meaning that every

two-way combination of variables is represented (e.g. a_4 is paired with every b and c perturbed point). If the strength is increased to three, the number of training samples necessary doubles, but the set of two-way interactions is a subset of the three way interaction samples. Therefore, a strength two analysis can easily be scaled to strength three. If a larger number of interactions are expected, then a different partial factorial analysis should be employed.

Step 3: *Determine the shape parameters.*

Just as Step 2 required a location parameter for each of the final component curves, this step, shown as Step 3 in Figure 21, requires a shape parameter for each of the component curves. The shape parameter is defined as the average deviation of the extreme sample points from the location parameter. As with Step 2, an orthogonal array is used to combine the extreme values (as was described in Step 2, if an orthogonal array is not a satisfactory means of combining inputs, another partial factorial design of experiments should be used). The equation to define the shape parameters is given below:

$$\sigma_n = \frac{1}{TN}\sum_{i=1}^{T} \mu_n - F_i \quad (3)$$

where n is the component curve (e.g. curves "A", "B", "C", "D", or "E" in the example in Figure 21), T is the number of rows in the orthogonal array, N is the number of standard deviations used in Step 1, and F_i is the i^{th} sample point from the orthogonal array of extremes. In the example shown in Figure 21, four additional full-scale simulations are necessary for this step, bring the current total number of simulations to nine.

Step 4: *Determine the shift parameters.*

In this step, as is shown in Step 4 of Figure 21, the shift parameter is determined for each of the component curves based on the skew of the curves. If a curve has a positive skew, evidenced by a negative shape parameter, then the shift parameter is equal to the minimum result of all of the full-scale simulations or the result of the full-scale simulation with all inputs equal to zero, whichever is lower. If instead the curve has a negative skew, determined via a positive shape parameter, then the shift parameter is equal to the maximum result from all of the full-scale simulations. For the example shown in Figure 21, this step requires at most one additional simulation, bringing the total number of simulations for a scenario with three uncertain input parameters to ten simulations. Table 4 provides the number of simulations necessary for a given number of uncertain input parameters, assuming that an orthogonal array with a strength of two has been used.

Step 5: *Combine the component distributions*.

A three-parameter modified-lognormal distribution has been developed to approximate the output distribution. This distribution is similar to a textbook lognormal distribution [88], but adapted to account for an offset and the possibility of a negative skew. The probability density function of the modified-lognormal distribution is given by the following functional form:

$$g_z(\mu,\sigma,\theta,z) = \frac{1}{\frac{\sigma}{|\sigma|}(\theta-z)\sqrt{2\pi \ln\left(\frac{\mu-\theta+\sqrt{(\mu-\theta)^2+4\sigma^2}}{2(\mu-\theta)}\right)}} \exp\left(-\frac{\left(ln\left(\frac{\sigma}{|\sigma|}(\theta-z)\right)-\ln\left(\frac{\sigma}{|\sigma|}(\theta-\mu)\right)\right)^2}{2\ln\left(\frac{\mu-\theta+\sqrt{(\mu-\theta)^2+4\sigma^2}}{2(\mu-\theta)}\right)}\right) \quad (4)$$

and the cumulative density function is given by the form:

$$G_z(\mu,\sigma,\theta,z) = \frac{1}{2} + \frac{\sigma}{2|\sigma|}\mathrm{erf}\left(\frac{ln\left(\frac{\sigma}{|\sigma|}(\theta-z)\right)-\ln\left(\frac{\sigma}{|\sigma|}(\theta-\mu)\right)}{\sqrt{2\ln\left(\frac{\mu-\theta+\sqrt{(\mu-\theta)^2+4\sigma^2}}{2(\mu-\theta)}\right)}}\right) \quad (5)$$

in which z is the independent variable for the modified-lognormal distribution, μ is the location parameter determined from Step 2, σ is the shape parameter determined from Step 3, and θ is the shift parameter determined from Step 4.

Once all of the parameters for the component distributions have been determined via Steps 1-4, the parameters are plugged into Eq. 1 to determine the PDF for each component distribution or Eq. 2 to determine the CDF. The component distributions are then averaged, with the "A" component distribution being weighted equal to the weight of the perturbed distributions. For example, in the example shown in Figure 21, the "A" distribution will be weighted four times as heavily as any of the other distributions.

Table 4: Number of simulations necessary for a given number of uncertain inputs and order of composite curve.

Number of uncertain input parameters	Number of simulations necessary
2-3	10
4-7	18
8-11	26
12-15	34
16-31	66

4.3 Analytical and Computational Models

The QUICKER methodology is demonstrated by considering two analytical models and two computational models. The analytical models are a third order polynomial function and a discontinuous function so as to highlight key aspects of the methodology, and the computational models include a three-dimensional circulating fluidized bed and a one-dimensional two-phase turbulent flow. These models are described below and are used in the next section to demonstrate the utility of the QUICKER methodology to quantify uncertainty in highly nonlinear computations with significant time reductions and minimal loss of accuracy.

4.3.1 Analytical Models

Analytical Model 1: One of the analytical models considered is expressed by the function $f(a,b,c) = a^3 + b^3 + c^3 + a^2b + b^2a + a^2c + c^2a + b^2c + c^2b$ with Gaussian uncertainty in with a mean and standard deviation for x of 1 for both, a mean and standard deviation for b of 2 for both, and a mean and standard deviation for c of 3 and 1 respectively. This function was chosen to highlight the effects of a nonlinear system with multiple interactions between input parameters, and will be used to compare the QUICKER methodology against Gaussian Process and Radial Basis Function meta-models and the SAMS method. For the sake of consistency, QUICKER, Gaussian Process, and Radial Basis Function methods will all use the same ten training points: the points determined from Step 1 of Section 4.2.3. The SAMS methodology requires a specified number of training points: nine points for three uncertain input parameters.

This same function will then be used to demonstrate the QUICKER methodology with non-Gaussian input distributions. First, uniform distributions with a ranging from 0 to 2, b ranging from 1 to 3, and c ranging from 2 to 4 will be explored. Then, Weibull distributions with a shape parameter and scale parameter for a of 2 and 1 for respectively, a shape parameter and scale parameter for b of 1.5 and 1 respectively, and shape and scale parameters of 3 and 3.5 for c

respectively. Last, triangle functions with a min, max, and peak for a of 1, 2, and 1.5, a min, max, and peak for b of 1, 3, and 1.5 respectively, and a min, max, and peak for c of 2, 5, and 4.5 respectively. These inputs have been chosen to highlight the versatility of the QUICKER methodology by handling non-Gaussian input distributions.

Analytical Model 2: The second analytical model considered is aimed at illustrating the ability of the QUICKER methodology to handle discontinuities in the system, even when conventional meta-models cannot. This model is described by the step function $f(a,b,c) = H(a+b+c-4)$ where $H(a)$ is the unit step function such that $H(a) = 0, a < 0; H(a) = 1, a \geq 0$, and with Gaussian uncertainty in a with a mean and standard deviation both of 1, a mean of and standard deviation for b both of 2, and a mean and standard deviation for c of 3 and 1 respectively. As described in the description of the previous analytical model, QUICKER, Gaussian Process, and Radial Basis Function will all use the same ten training points, and SAMS will use the nine specified.

4.3.2 Computational Models

Computational Model 1: The first computational model considered is that of a three-dimensional circulating fluidized bed, in which solid particles are injected into the bottom of a cylindrical column with air flowing through it, as is shown in Figure 22a, with the particles and gas exiting at the top of the column. This isothermal simulation incorporates the gas and solids as two distinct phases, and includes the interactions between the phases. The governing equations for this process are summarized in Table 5, and the boundary conditions, initial conditions, and nominal parameters for this simulation are provided in Table 6. The model is solved using the Multiphase Flow with Interphase eXchanges (MFIX) computational software available from the National Energy and Technology Laboratory [89, 90].

This model has 3 uncertain input parameters: the particle-particle coefficient of restitution, the particle diameter, and the particle density. Two different representations of the uncertainty are considered for each of these parameters: (1) a Gaussian distribution of uncertainty on each parameter (denoted as CFB(G)) and (2) a uniform distribution of uncertainty on each parameter (denoted as CFB(U)). The standard deviation—or interval size for the uniform distributions—on each uncertain parameter is considered to be 10% of the nominal value subject to physical bounds (such as limiting the coefficient of restitution to be less than unity). Since this scenario has three uncertain input parameters, just as the two analytical scenarios did, it will also use ten training

points for QUICKER, Radial Basis Function, and Gaussian Process regression, and will use nine training points for SAMS.

The output parameter analyzed in this model is the time-averaged porosity at 4.125 m from the bottom of the column, sufficiently far from the inlet and outlet. The porosity is one of the primary output parameters in a non-reacting fluidized bed that generally has a minimal variance. This minimal variance allows for a demonstration of the QUICKER methodology in accurately quantifying uncertainty over a narrow range.

Table 5: Governing equations for the circulating fluidized bed.

Circulating Fluidized Bed Governing Equations	
Gas Continuity	$\frac{\partial}{\partial t}(\varepsilon_g \rho_g) + \frac{\partial}{\partial x_i}(\varepsilon_g \rho_g U_{gi}) = 0$
Solid Continuity	$\frac{\partial}{\partial t}(\varepsilon_s \rho_s) + \frac{\partial}{\partial x_i}(\varepsilon_s \rho_s U_{si}) = 0$
Gas Momentum	$\frac{\partial}{\partial t}(\varepsilon_g \rho_g U_{gi}) + \frac{\partial}{\partial x_j}(\varepsilon_g \rho_g U_{gj} U_{gi}) = -\varepsilon_g \frac{\partial P_g}{\partial x_i} + \frac{\partial \tau_{gij}}{\partial x_j} + \beta(U_{gi} - U_{si}) + \varepsilon_g \rho_g g_i$ $\tau_{gij} = \mu_g \left(\frac{\partial U_{gi}}{\partial x_j} + \frac{\partial U_{gj}}{\partial x_i}\right) - \frac{2}{3}\frac{\partial U_{gi}}{\partial x_i}\delta_{ij}$
Solid Momentum	$\frac{\partial}{\partial t}(\varepsilon_s \rho_s U_{si}) + \frac{\partial}{\partial x_j}(\varepsilon_s \rho_s U_{sj} U_{si}) = -\varepsilon_g \frac{\partial P_g}{\partial x_i} + \frac{\partial \tau_{sij}}{\partial x_j} - \beta(U_{gi} - U_{si}) + \varepsilon_s \rho_s g_i$ $\tau_{sij} = \left(-P_s + \lambda \frac{\partial U_{si}}{\partial x_i}\right)\delta_{ij} + \mu_s \left(\frac{\partial U_{si}}{\partial x_j} + \frac{\partial U_{sj}}{\partial x_i}\right) - \frac{2}{3}\frac{\partial U_{si}}{\partial x_i}\delta_{ij}$
Ideal Gas Law	$\rho_g = \frac{P_g M}{RT}$
Stress properties	$\mu_s = 1.6\left[\frac{\mu_s^*}{g_0 \eta(2-\eta)}\left(1 + \frac{8}{5}\eta \varepsilon_s g_0\right)\left(1 + \frac{8}{5}\eta(3\eta - 2)\varepsilon_s g_0\right) + \frac{3}{5}\eta \mu_b\right]$ $\lambda = \eta \mu_b$ $\mu_s^* = \frac{\rho_s \varepsilon_s g_0 \Theta \mu}{\rho_s \varepsilon_s g_0 \Theta + \frac{2\beta\mu}{\rho_s \varepsilon_s}}$ $P_s = \rho_s \varepsilon_s (1 + 4\eta \varepsilon_s g_0)\Theta$ $\mu = \frac{5}{96}\rho_s d_s \sqrt{\pi \Theta}$ $\mu_b = \frac{256}{5\pi}\mu \varepsilon_s^2 g_0$
Terminal Velocity Drag	$V_r = 0.5\left(A - 0.06 Re_s + \sqrt{(0.06 Re_s)^2 + 0.12 Re_s(2B - A) + A^2}\right)$ $\beta = \frac{3\varepsilon_s \varepsilon_g \rho_g}{4 V_r^2 d_s}\left(0.63 + 4.8\sqrt{\frac{V_r}{Re_s}}\right)^2 \left\|\overline{U}_s - \overline{U}_g\right\|$ $A = \varepsilon_g^{4.14}$ $Re_s = \frac{d_s \left\|\bar{v}_s - \bar{v}_g\right\| \rho_g}{\mu_g}$ $B = \begin{cases} 0.8\varepsilon_g^{1.28} & if \ \varepsilon_g \le 0.85 \\ \varepsilon_g^{2.65} & if \ \varepsilon_g > 0.85 \end{cases}$
Algebraic Granular Energy	$\Theta = \left\{\frac{-K_1 \varepsilon_s D_{sii} + \sqrt{K_1^2 D_{sii}^2 \varepsilon_s^2 + 4K_4 \varepsilon_s \left[K_2 D_{sii}^2 + 2K_3 D_{sij} D_{sij}\right]}}{2\varepsilon_s K_4}\right\}^2$ $K_3 = \left\{\frac{\sqrt{\pi}}{3(3-e_s)}[0.5(3e_s + 1) + 0.4(1 + e_s)(3e_s - 1)\varepsilon_s g_0] + \frac{8\varepsilon_s g_0 (1+e_s)}{5\sqrt{\pi}}\right\}$ $K_1 = 2(1 + e_s)\rho_s g_0$ $K_4 = \frac{12(1-e_s^2)\rho_s g_0}{d_s \sqrt{\pi}}$ $K_2 = \frac{4 d_s \rho_s (1+e_s)\varepsilon_s g_0}{3\sqrt{\pi}} - \frac{2}{3}K_3$
Additional Equations	$g_0 = \left[1 - \left(\frac{\varepsilon_s}{\varepsilon_{s,max}}\right)^{\frac{1}{3}}\right]^{-1}$ $\eta = \frac{1+e_s}{2}$ $D_{sij} = \frac{1}{2}\left(\frac{\partial U_{si}}{\partial x_j} + \frac{\partial U_{sj}}{\partial x_i}\right)$

Table 6: Boundary and initial conditions, and parameters for the circulating fluidized bed.

Circulating Fluidized Bed Boundary and Initial Conditions and Parameters		
Geometry	z_0 = 9.55 m	Solids inlet: z = [0.3, 0.5] m
	r_0 = 0.2 m	Solids inlet: r = 0.2 m
	Gas inlet: z = 0 m	Mixed exit: z = [8.9, 9.1] m
	Gas inlet: r = [0, 0.2] m	Mixed exit: r = 0.2 m
Nominal Properties	e_s = 0.8	d_s = 0.00012 m
	M = 0.029 kg/mol	ρ_s = 2,600 kg/m^3
	μ_g = 0.000018 kg/m·s	
Initial Conditions	ε_{g0} = 0.9	U_{sz0} = 0 m/s
	U_{gz0} = 4.2 m/s	U_{sr0} = 0 m/s
	U_{gr0} = 0 m/s	$U_{s\theta 0}$ = 0 m/s
	$U_{g\theta 0}$ = 0 m/s	
Gas Inlet	ε_g = 0.9	v_{gz} = 4.2 m/s
	P_g = 115.142 kPa	T = 294 K
Solids inlet	ε_g = 0.4	T =294 K
	P_g = 115.142 kPa	
Mixed exit	P = 115.142 kPa	

Computational Model 2: The second computational model is for a turbulent fluidized bed involving periodic flow between two walls, as is shown in Figure 22b. The governing equations are summarized in Table 5 and Table 7, in which turbulence in the bed is described using the model in Ref. [91] with the boundary conditions as in Ref. [92]. The boundary conditions, initial conditions, and nominal parameters for this model are provided in Table 8. Eleven uncertain input parameters—particle density, particle diameter, particle-particle coefficient of restitution, angle of internal friction, packed bed void fraction, particle-wall coefficient of restitution, angle of internal friction at walls, initial gas velocity, initial gas pressure, initial gas temperature, and initial solid velocity—are considered in the QUICKER uncertainty quantification analysis. As can be seen in Table 4, 11 uncertain input parameters requires 26 training data points for QUICKER, and the same number will be used for Radial Basis Function and Gaussian Process regression. SAMS methodology requires 27 points for 11 uncertain input parameters. As with the circulating fluidized bed, two different representations of uncertainty are considered for each of the input parameters: (1) a Gaussian distribution of uncertainty on each parameter (denoted as TFB(G)) and (2) a uniform distribution of uncertainty (denoted as TFB(U)). As in the uncertainty quantification involving Computational Model 1, a standard deviation of 10% of the nominal value was considered on each uncertain parameter, subject to its physical bounds. The output

parameter analyzed in the turbulent fluidized bed model is the time-averaged solid velocity, which, unlike the porosity in the case of the circulating fluidized bed, generally exhibits a large variance. The two computational models provide evidence of the effectiveness of the QUICKER methodology over a range of possible output variances.

Uncertainty quantification based on the four models presented in this section and using the QUICKER methodology outlined in Section 4.2 are presented and discussed in the following section.

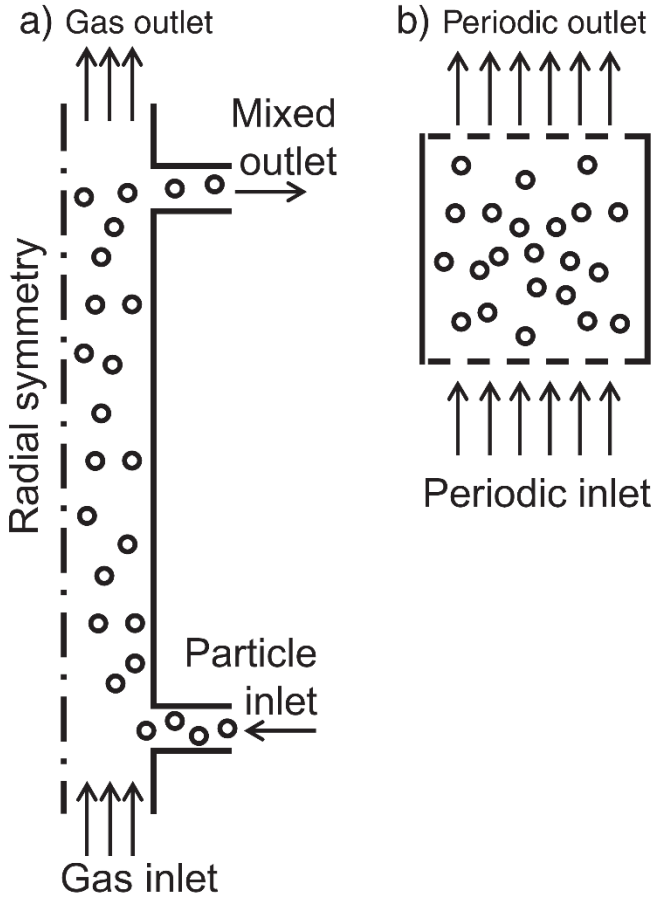

Figure 22: Schematic of the geometric domain for (a) the circulating fluidized bed and (b) the turbulent/periodic fluidized bed.

Table 7: Governing equations for the turbulent/periodic fluidized bed.

Turbulent/Periodic Fluidized Bed Governing Equations			
Gas Turbulence Modeling	$\varepsilon_g\rho_g\left[\frac{\partial k_g}{\partial t}+U_{gj}\frac{\partial k_g}{\partial x_j}\right]=\frac{\partial}{\partial x_i}\left(\varepsilon_g\mu_g^t\frac{\partial k_g}{\partial x_i}\right)+\varepsilon_g\tau_{gij}\frac{\partial U_{gi}}{\partial x_j}+\Pi_{kg}-\varepsilon_g\rho_g\varepsilon_g^t$ $\varepsilon_g\rho_g\left[\frac{\partial \varepsilon_g^t}{\partial t}+U_{gj}\frac{\partial \varepsilon_g^t}{\partial x_j}\right]=\frac{\partial}{\partial x_i}\left(\varepsilon_g\frac{\mu_g^t}{1.3}\frac{\partial \varepsilon_g^t}{\partial x_i}\right)+\varepsilon_g\frac{\varepsilon_g^t}{k_g}\left(1.44\tau_{gij}\frac{\partial U_{gi}}{\partial x_j}+1.92\rho_g\varepsilon_g^t\right)$		
	$\mu_g^t=0.09\rho_g\left[1+\left(\frac{\tau_L^x}{\tau_g^t}\right)\left(\frac{\varepsilon_s}{\varepsilon_{s,max}}\right)^3\right]^{-1}\frac{k_g^2}{\varepsilon_g^t}$ $\Pi_{kg}=\beta(3\Theta-2k_g)$	$\tau_L^x=\frac{\varepsilon_s\rho_s}{\beta}$ $\tau_g^t=0.135\frac{k_g}{\varepsilon_g^t}$	$k_g=\frac{1}{2}\langle u_g u_g\rangle$
Solids Turbulence Modeling	$\varepsilon_s\rho_s\left[\frac{\partial\Theta}{\partial t}+U_{sj}\frac{\partial\Theta}{\partial x_j}\right]=\frac{\partial}{\partial x_i}\left(\varepsilon_s\rho_s\kappa_s^t\frac{\partial\Theta}{\partial x_i}\right)+\varepsilon_s\rho_s\tau_{sij}\frac{\partial U_{si}}{\partial x_j}+\Pi_{ks}-\varepsilon_s\rho_s\varepsilon_s^t$ $\kappa_s^t=0.1306\rho_s d_s(1+e_s^2)\left(\frac{1}{g_0}+4.8\varepsilon_s+12.1184g_0\varepsilon_s^2\right)\sqrt{\Theta}$		
	$\varepsilon_s^t=12(1-e_s^2)\varepsilon_s^2\rho_s g_0\frac{\Theta^{\frac{3}{2}}}{d_s}$	$\Pi_{ks}=\beta\left(\frac{2k_g}{1+\frac{\tau_L^x}{\tau_g^t}}-3\Theta\right)$	$\Theta=\frac{1}{3}\langle u_s u_s\rangle$
Stress properties	**If $\boldsymbol{\varepsilon_g>\varepsilon_g^*}$:** $\mu_s=\left[1+\left(\frac{\tau_g^t}{\tau_L^x}\right)\left(\frac{\varepsilon_s}{\varepsilon_{s,max}}\right)^3\right]^{-1}\left[0.1045\left(\frac{1}{g_0}+3.2\varepsilon_s+12.1824g_0\varepsilon_s^2\right)d_s\rho_s\sqrt{\Theta}\right]$ $\lambda=\frac{5}{3}\left[1+\left(\frac{\tau_g^t}{\tau_L^x}\right)\left(\frac{\varepsilon_s}{\varepsilon_{s,max}}\right)^3\right]^{-1}\left[0.1045\left(12.1824g_0\varepsilon_g^2\right)d_s\rho_s\sqrt{\Theta}\right]$		
	$P_s=\varepsilon_s\rho_s\Theta\left[(1+4\varepsilon_s g_0)+\frac{1}{2}(1-e_s^2)\right]$	$\varepsilon_s^t=12(1-e_s^2)\varepsilon_s^2\rho_s g_0\frac{\Theta^{\frac{3}{2}}}{d_s}$	
	If $\boldsymbol{\varepsilon_g\le\varepsilon_g^*}$:		
	$\lambda=0$ $P_s=10^{20}\left(\varepsilon_g^*-\varepsilon_g\right)^{10}\ kPa$	$\mu_s=\frac{P_s\sin(\phi)}{2\sqrt{I_{2D}}}$	
	$I_{2D}=\frac{1}{6}[(D_{s11}-D_{s22})^2+(D_{s22}-D_{s33})^2+(D_{s33}-D_{s11})^2]+D_{s12}^2+D_{s23}^2+D_{s31}^2$ Turbulence Modeling for solids is not used		
Wall Functions	$\frac{\partial U_g}{\partial x}\|_w=\frac{0.23\rho_g U_g k_g^{\frac{1}{2}}}{(\mu_g+\mu_g^t)\ln(9.81x^*)}$ $x^*=\frac{0.5477\rho_g k_g^{\frac{1}{2}}\Delta x}{2\mu_g}$ $\quad$ $\varepsilon_g=\frac{0.3286k_g^{\frac{3}{2}}}{\kappa\Delta y}$	production of $k_g=0.3\varepsilon_g\rho_g k_g\frac{U_g}{\frac{\Delta x}{2}\ln(9.81x^*)}$ dissipation of $k_g=\varepsilon_g\rho_g\varepsilon_g^t$	
Blended Drag	$\beta=\begin{cases}\frac{3}{4}C_D\frac{\rho_g\varepsilon_g\varepsilon_s\lvert\bar{U}_g-\bar{U}_s\rvert}{d_s}\varepsilon_g^{-2.65}\ \text{if}\ \varepsilon_g\ge0.8\\ \frac{150\varepsilon_s(1-\varepsilon_g)\mu_g}{\varepsilon_g d_s^2}+\frac{1.75\rho_g\varepsilon_s\lvert\bar{U}_g-\bar{U}_s\rvert}{d_s}\ \text{if}\ \varepsilon_g<0.8\end{cases}$ $C_D=\begin{cases}\frac{24}{\varepsilon_g Re_s\left(1+0.15(\varepsilon_g Re_s)^{0.687}\right)}\ \text{if}\ \varepsilon_g Re_s<1{,}000\\ 0.44\ \text{if}\ \varepsilon_g Re_s\ge1{,}000\end{cases}$		

Table 8: Boundary and initial conditions, and parameters for the turbulent/periodic fluidized bed.

Turbulent/Periodic Fluidized Bed Boundary and Initial Conditions and Parameters		
Geometry	x_0 = 0.1 m	Periodic in y-direction
	y_0 =0.1 m	$\dot{m}_g$ = 0.0006 kg/s
	Inlet: x = 0 m	ΔP = 0.08 kPa
	Outlet: x =0.1 m	
Nominal Properties	μ_g = 0.000018 kg·m/s	ϕ = 30°
	M = 0.029 kg/mol	e_w = 0.7
	ρ_s = 2400 kg/m^3	ε_g^* = 0.36
	d_s = 0.00012 m	ϕ_w = 11.31°
	e_s = 0.95	
Nominal Initial Conditions	U_{gy0} = 5 m/s	Θ_0 = 0.1 m^2/s^2
	P_0 = 101.325 kPa	k_{g0} = 0.01 m^2/s^2
	T_0 = 298 K	ε_{g0}^t = 0.1 m^2/s^3
	U_{sy0} = 4.1 m/s	
Boundary Condition	$\mu_s \frac{\partial U_s}{\partial x}\|_w = P_s \tan(\phi_w)\, U_2/\|U_2\|$	$\kappa_s \frac{\partial \Theta}{\partial x}\|_w = P_s\sqrt{3\Theta}\frac{3}{8}[\frac{7}{2}(1+e_w)\tan^2\phi_w - (1-e_w)$

4.4 Results and Discussion

The QUICKER, Gaussian Process (GP), Radial Basis Function (RBF), and SAMS will all be used to predict the output distribution of both analytical and computational models. As a benchmark for comparison, a Monte Carlo direct sampling method will be applied to the analytical models, and a Latin Hypercube direct sampling will be applied to the computational models. Latin Hypercube sampling is used instead of Monte Carlo due to the significant computational cost of the computational models. In all four cases, the Monte Carlo or Latin Hypercube results will be assumed to be very close to the exact answer due to the rigorous sampling required by both methods.

4.4.1 Analytical Models

The ability of QUICKER, Gaussian Process (GP), Radial Basis Function (RBF), and SAMS to predict a system with interactions between input variables is explored by considering the system described by a third order polynomial function (Analytical Model 1). The performance of these four techniques is compared against a Monte Carlo direct sampling in Figure 23, with a probability density function (PDF) show in Figure 23a and a cumulative density function (CDF) shown in Figure 23b. In both parts of the figure, the Monte Carlo results are shown by histograms

and the other techniques by dashed or solid lines. In order to accurately compare the curves and histograms, both have been normalized so that the area under each is equal to unity.

The accuracy of each uncertainty analysis technique is determined by calculating the root mean squared error (RMSE) between the Monte Carlo CDF and the predicted CDF for each technique. As can be seen in Figure 23b, the QUICKER and Radial Basis Function methods both accurately predict the Monte Carlo output distribution. The Gaussian Process estimation is

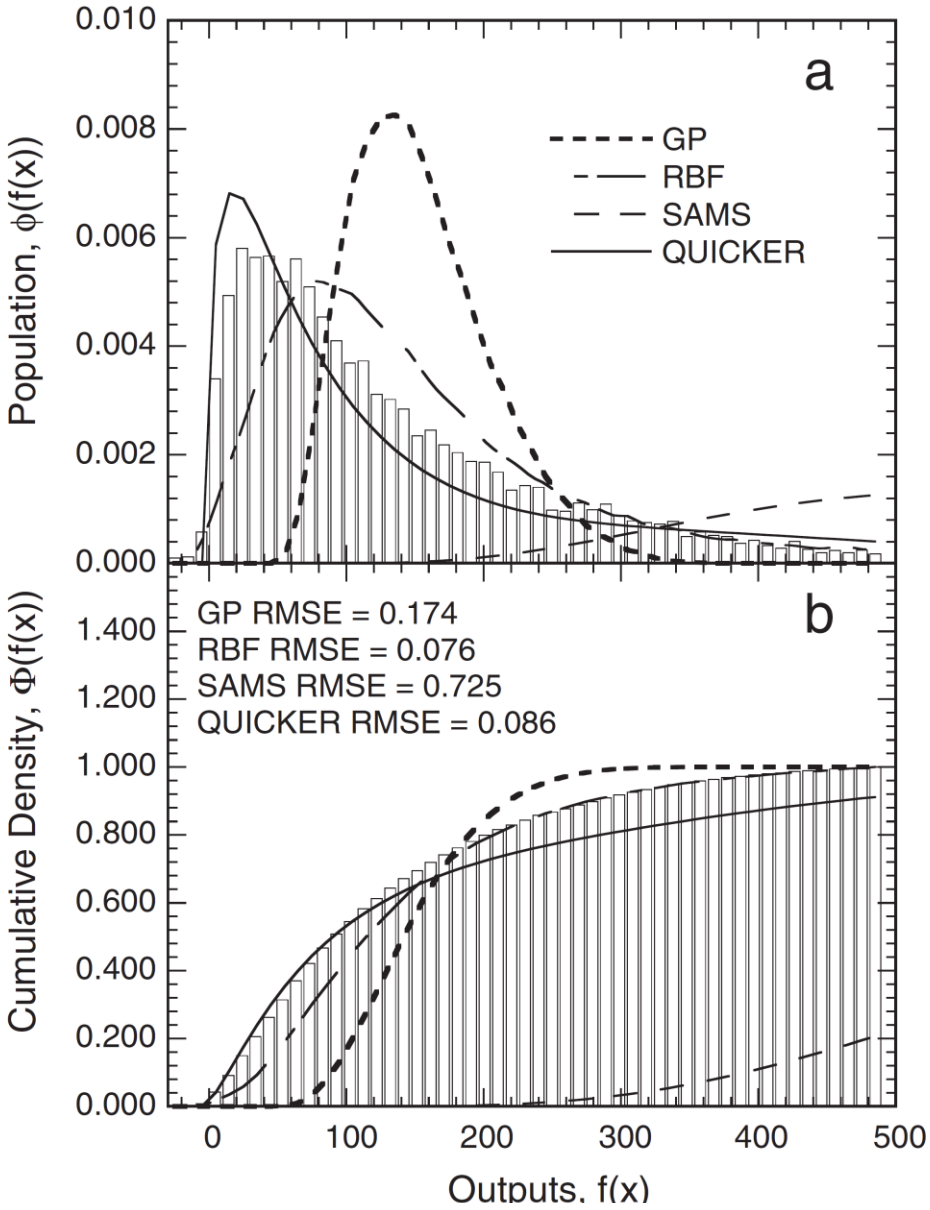

Figure 23: Comparison of the (a) probability density function and (b) cumulative density function obtained by using Monte Carlo sampling, Gaussian Process and Radial Basis Function meta-models, the SAMS methodology, and QUICKER methodology for a system described by a cubic function (Analytical Model 1)

noticeably worse than the Radial Basis function, as was also found in Refs. [77] and [93]. SAMS is built on a quadratic meta-model, and was not able to accurately capture the cubic nature of the given scenario, but it should be noted that the SAMS method utilized one fewer training point than the other three methods.

For the scenario shown in Figure 23, all uncertain inputs followed a Gaussian distribution, and the QUICKER method was able to capture the system behavior. In Figure 24, the results of using a variety of different input distributions into a third order polynomial (Analytical Model 1) is presented. As with Figure 23, the Monte Carlo results are shown with a histogram, and the QUICKER prediction is shown with a solid line. Figure 24a, b, and c present the PDF for uniform, triangle, and Weibull inputs distributions. The corresponding CDF is shown below each PDF. The root mean squared error has been calculated for the difference between each of the Monte Carlo CDFs and QUICKER CDFs, and in all cases the error is small, less than 6%. Due to the nature of the perturbed points, a_4 and a_5 in Figure 20g, QUICKER is able to capture the behavior of minimally constrained inputs, such as the uniform distribution, as well as asymmetric inputs, such as the triangle and Weibull distributions.

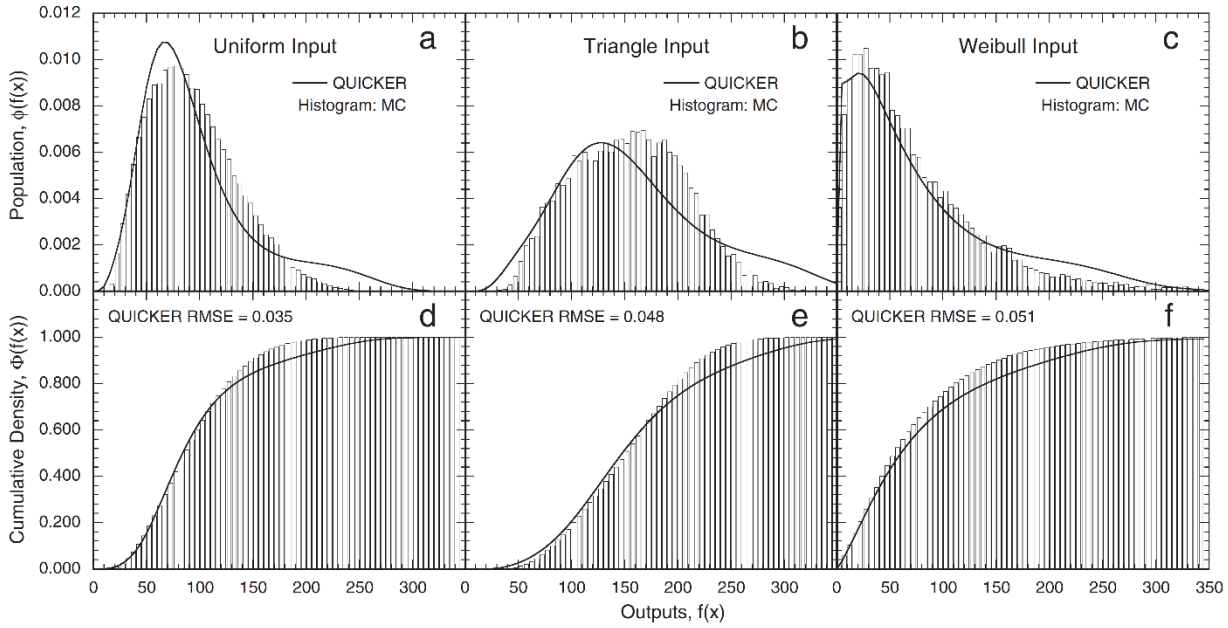

Figure 24: Comparison of the probability density function and cumulative density function obtained using Monte Carlo sampling and QUICKER for a system described by a cubic function using (a, d) uniform input distributions, (b, e) triangle input distributions, an

In Figure 25, the QUICKER, Gaussian Process, Radial Basis Function, and SAMS were used to predict the performance of a system with a discontinuity (Analytical Model 2). As with Figure

23, Figure 25 shows the Monte Carlo results via a histogram, and the four uncertainty analysis techniques are shown with dashed or solid lines. From the PDF shown in Figure 25a, it can be seen that the Monte Carlo result is split between results at 0 and results at 1. Both the Gaussian

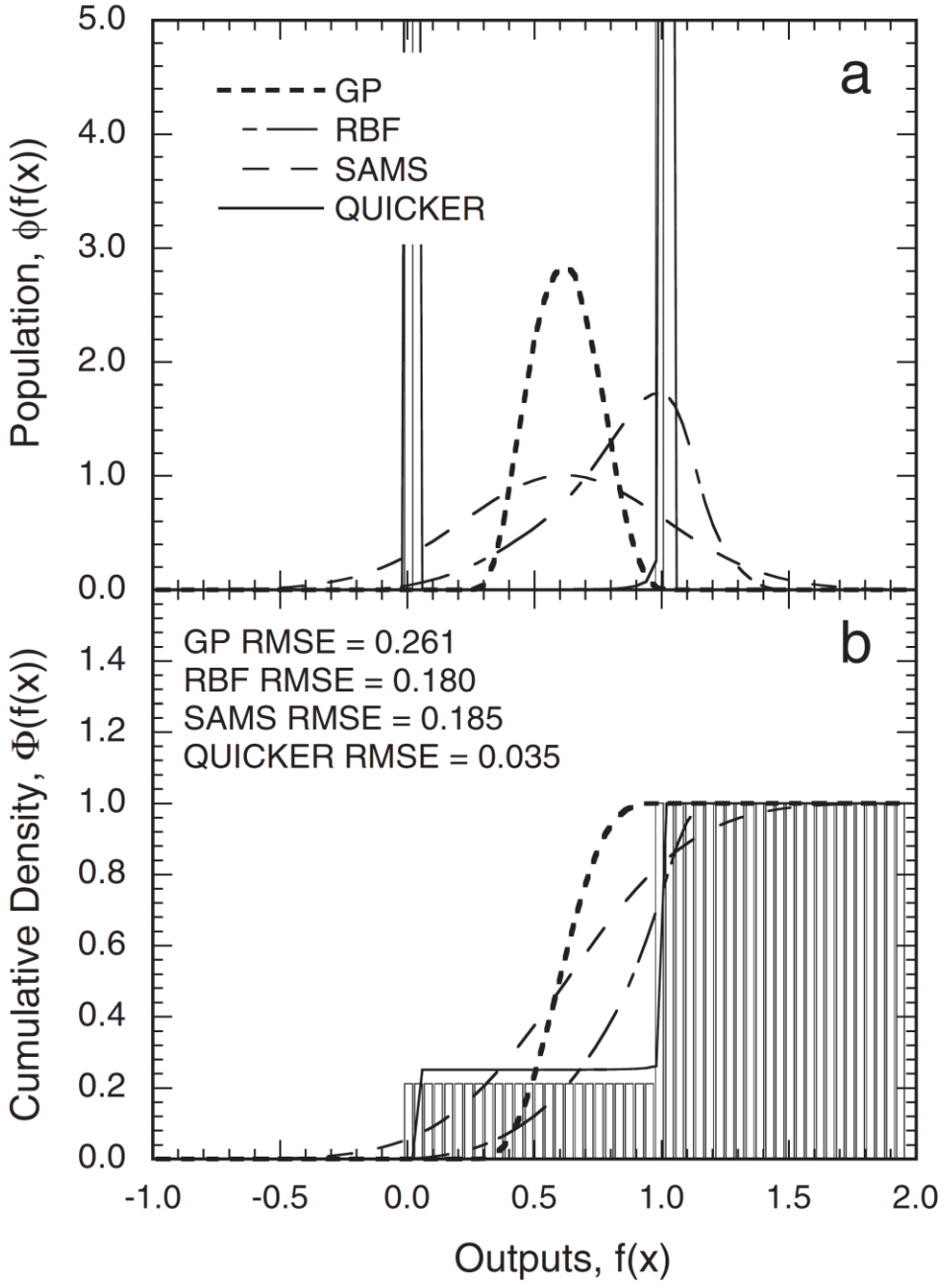

Figure 25: Comparison of the (a) probability density function and (b) cumulative density func-tion obtained using Monte Carlo sampling, Gaussian Process and Radial Basis Function meta-models, the SAMS method, and QUICKER methodology for a sys-tem described by a step function (Analytical Model 2).

Process meta-model and SAMS have predicted an average of these two, at a value of approximately 0.5. The Radial Basis function returned a result biased towards 1, where a larger percentage of the Monte Carlo results lie. These three conventional techniques were unable to capture the bimodality or the tight variance of each mode. This highlights the limited ability of meta-models to capture scenarios with discontinuities and SAMS's need for a scenario to be approximated via a quadratic response surface.

In contrast, QUICKER accurately predicted the discontinuous output of Analytical Model 2. By relying on multiple component distributions, as is shown in Figure 20i, QUICKER was able to capture the bimodal nature of the step function. The QUICKER result is accurate enough that it is difficult to distinguish from the Monte Carlo result. Since each component of the QUICKER prediction was only used to capture one of the output modes, it was able to portray the minimal uncertainty without being significantly biased by the second mode. The accuracy of the QUICKER result is particularly well-shown in Figure 25b, where the QUICKER CDF closely tracks the Monte Carlo CDF.

The two analytical models served to illustrate the benefits of QUICKER with regard to the accuracy and flexibility of the novel methodology. But being analytical models, the computational time for direct sampling is small and the time savings of using QUICKER are inconsequential for practical purposes. In contrast, the computational times requires for the numerical modeling of the circulating and turbulent fluidized beds are significantly large, requiring up to 125 hours of CPU time on a 2.53 GHz Intel Zeon processor for direct Latin Hypercube sampling.

4.4.2 Computational Models

Figure 26 presents the distributions of the time-averaged void fraction for a circulating fluidized bed with the input uncertainty corresponding to Gaussian inputs (Figure 26a and Figure 26c) as described in Section 4.3.2. The histograms in the plots denote the distributions obtained using a Latin Hypercube Sampling method and the solid and dashed lines represent the output of the QUICKER, Gaussian Process, Radial Basis Function, and SAMS methodologies. It is seen from Figure 26c that both meta-models (Gaussian Process and Radial Basis Function) and QUICKER accurately capture the behavior of the void fraction, with the Radial Basis Function outdoing QUICKER and Gaussian Process by about 4 percentage points. In this scenario the Radial Basis Function outperforms QUICKER, but the consistent accuracy of QUICKER when

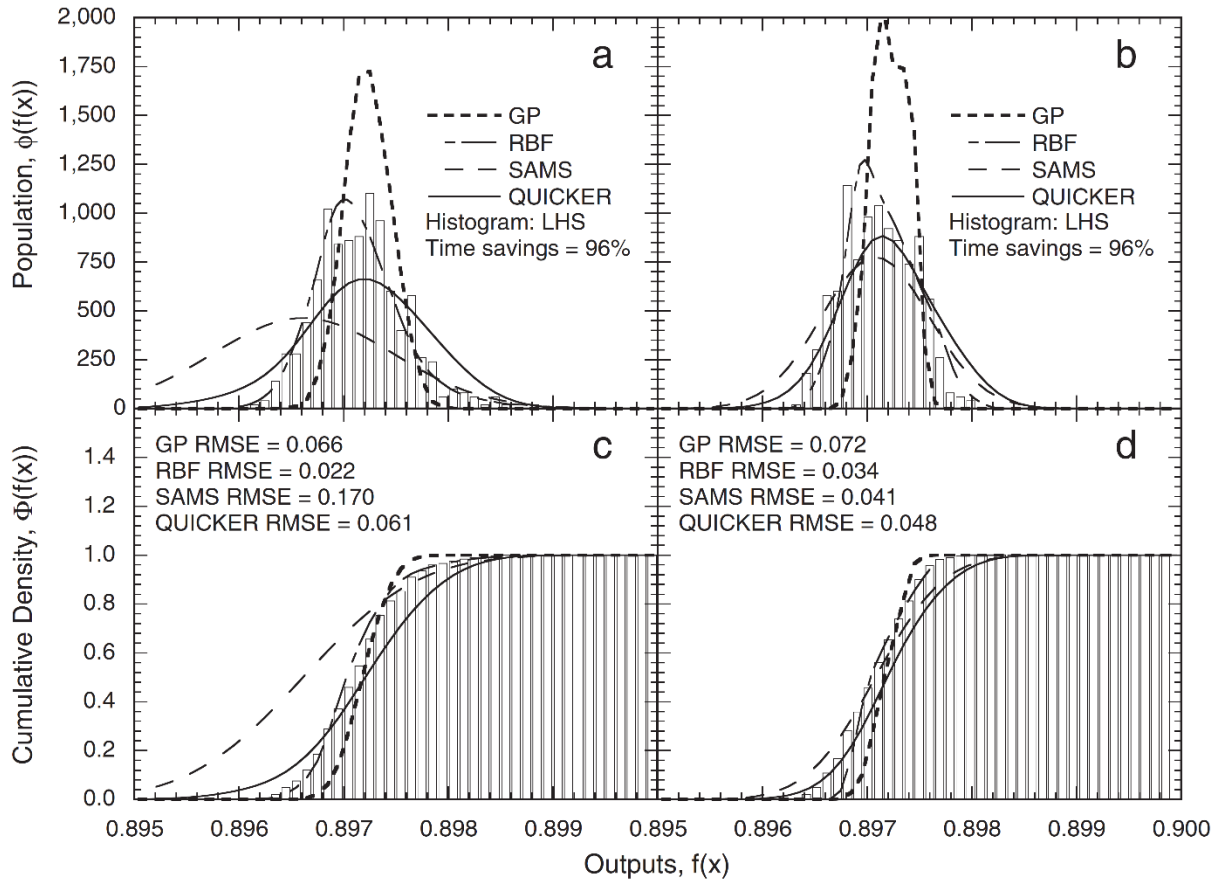

Figure 26: Comparison of the probability density function and cumulative density function obtained using Latin Hypercube Sampling, Gaussian Process and Radial Basis Function meta-models, the SAMS method, and QUICKER methodology for the circulating fluidized be

Radial Basis Function performs very poorly more than makes up for this small difference in accuracy. The SAMS methodology is less accurate.

An analysis of the same circulating fluidized bed model is shown with uniformly distributed inputs in Figure 26b and Figure 26d. As with Figure 24, where uniform, triangle, and Weibull distributions were analyzed with QUICKER, this figure demonstrates an ability for the QUICKER methodology to capture the behavior of non-Gaussian distributions. This figure also demonstrates a significant improvement in the performance of SAMS and a small loss of accuracy for the Gaussian Process.

The computational time for uncertainty quantification based on Latin Hypercube Sampling using 250 samples is approximately 125 CPU hours on a 2.53 GHz Intel Xeon processor. In contrast, the QUICKER and meta-model approaches required 10 samples and 5 hours of CPU

time, and the SAMS method required 9 samples and 4.5 hours. Overall, this represents time reductions of 96%, as indicated in Figure 26.

The population distributions of the time-averaged solid velocity for a turbulent fluidized bed with *eleven* uncertain input parameters are shown in Figure 27 with Gaussian inputs (Figure 27a and Figure 27c) and uniform inputs (Figure 27b and Figure 27d), as described in Section 4.3.2. The histograms in the plots represent the distributions obtained using a Latin Hypercube Sampling method and the solid and dashed lines represent the output of the QUICKER, Gaussian Process, Radial Basis Function, and SAMS methodologies. For both the Gaussian and uniform input scenarios, the Radial Basis Function results are too far below the range of the other results

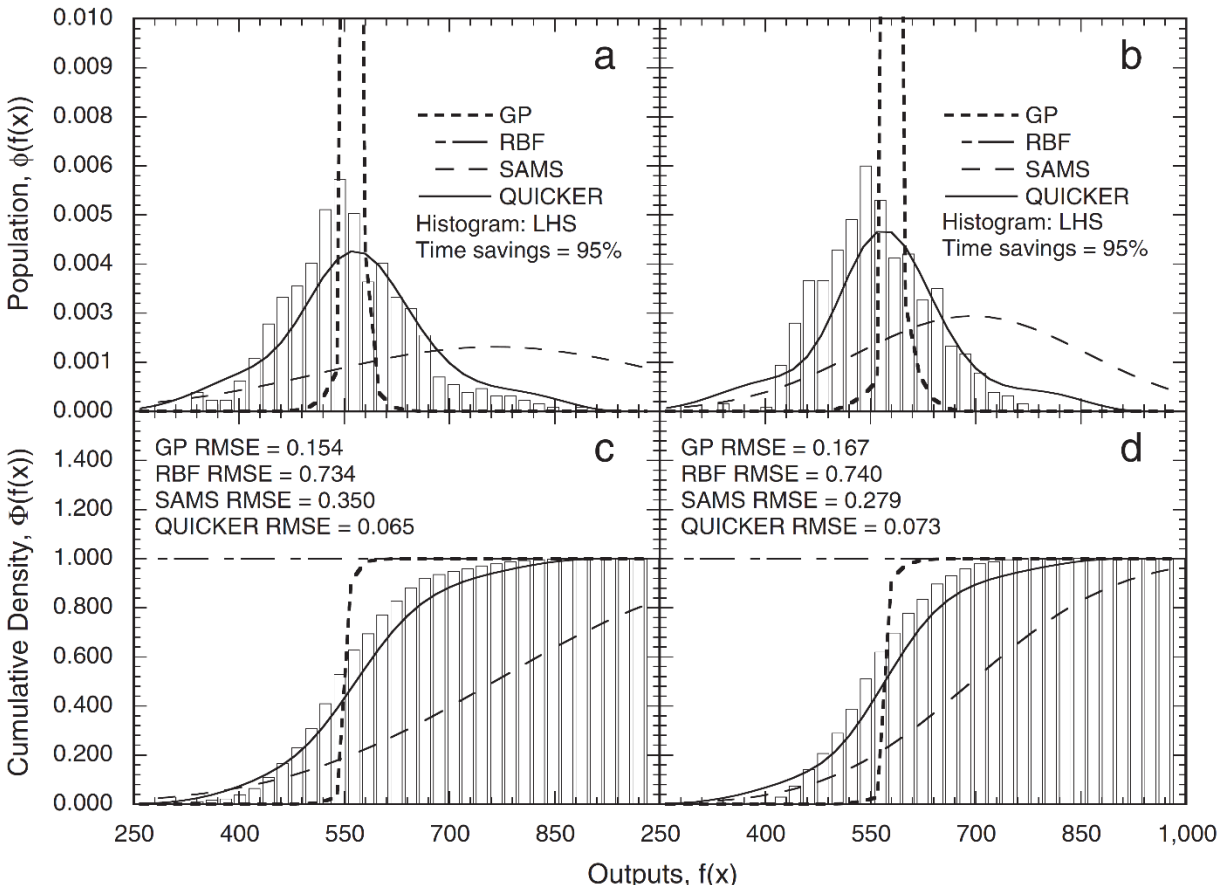

Figure 27: Comparison of the probability density function and cumulative density function obtained using Latin Hypercube Sampling, Gaussian Process and Radial Basis Function meta-models, the SAMS method, and QUICKER methodology for the turbulent fluidized bed (TFB): (a, c) Turbulent fluidized bed with Gaussian input distributions and (b, d) turbulent fluidized bed with uniform input distributions.

to show both on the same plot; and the large error shown in Figure 27c and Figure 27d reiterate this poor accuracy. The SAMS and Gaussian Process methods scale better, but are still not accurate. The Gaussian Process captures the location of the output distribution, but under

predicts the variance. In contrast, the SAMS methodology over predicts both the location and variance.

The turbulent fluidized bed model shows that of the four methods used to reduce the number of sample points, only QUICKER was able to return an accurate prediction. This is due to the fact that the QUICKER methodology does not require a meta-model. It is the poor scaling of meta-models that limit other conventional methodologies. Instead, QUICKER identifies the most critical sample points, and determines those directly from the full-scale model.

The computational time for uncertainty quantification based on Latin Hypercube Sampling using 500 samples is approximately 4.5 CPU hours on a 2.53 GHz Intel Xeon processor. On the other hand, the QUICKER and meta-model approaches required 26 samples and 0.2 hours of CPU time for this scenario, representing a 95% reduction in computation time. SAMS required 27 samples, also resulting in a time savings of approximately 95%. But this time savings came at a significant cost in accuracy for all methods except for QUICKER. Only QUICKER was able to return an accurate solution for this significant time savings.

Overall, the QUICKER approach was shown to yield accurate uncertainty quantification at a fraction of the computational time needed for an efficient direct sampling based method. This accuracy was consistently demonstrated across a range of different types of scenarios, including multiple scenarios where conventional meta-modeling tools and SAMS were unable to make accurate predictions, like with highly nonlinear scenarios or systems involving a large number of uncertain inputs.

The studies presented in this article considered inputs that are independent of one another. The extension of the methodology to handle correlated inputs is of interest in some practical applications, which will be addressed in a future work. This current chapter is focused on input uncertainties that can be well-defined by a given distribution (i.e. aleatory uncertainty). Future work will include techniques for handling inputs where the uncertainty is driven by a lack of information (i.e. epistemic uncertainty).

4.5 Conclusions

This chapter presents a novel methodology for uncertainty quantification, QUICKER, that can achieve comparable accuracy to direct sampling techniques, but with orders of magnitude less computational time and effort. This method was shown to be accurate, even in scenarios with a large number of uncertain input parameters or systems with significant nonlinearities, both of which cannot be accurately modeled via conventional meta-modeling techniques or SAMS. This new methodology relies on using a small number of training points to accurately determine

parameters for output distributions instead of building meta-models. The QUICKER methodology also relies on the average of multiple component distributions, thus including localized details of the output distribution. By requiring a small, well-defined number of sample points and making very few assumptions about the form of the output distribution, QUICKER is a faster technique for input uncertainty propagation than conventional methods, while providing more reliable accuracy across a wide range of problem types.

4.6 Nomenclature used in Chapter 4

a stochastic input parameter in Analytical Models 1 and 2 [—]

b stochastic input parameter in Analytical Models 1 and 2 [—]

c stochastic input parameter in Analytical Models 1 and 2 [—]

a_n example input point from Figure 20 and Figure 21 [—]

b_n example input point from Figure 20 and Figure 21 [—]

c_n example input point from Figure 20 and Figure 21 [—]

C_D drag coefficient [—]

d_s particle diameter [m]

D_s rate of strain tensor for solid phase [units]

e_s particle-particle coefficient of restitution [—]

e_w particle-wall coefficient of restitution [—]

F_i i^{th} sample point from orthogonal array in Step 3 [—]

g acceleration due to gravity [m^2/s]

g_0 radial distribution function at contact [—]

g_z PDF of modified-lognormal distribution as shown in Eq. 1 [—]

G_z CDF of modified-lognormal distribution as shown in Eq. 1 [—]

k_g turbulent kinetic energy of gas phase [m^2/s^2]

I_{2D} second invariant of the deviator of the strain rate tensor [s^{-2}]

N number of standard deviations separating mean from extremes [—]

P_{g0} initial gas pressure [kPa]

P_s solids pressure [kPa]

Q baseline output for a given scenario as is used in Eqs. 1 and 4 [—]

Re_s Reynolds number for solids phase [—]

t time [s]

T number of orthogonal array experiments in Steps 2 and 3 [—]

T_0 initial gas temperature [K]

u_g fluctuating gas velocity [m/s]

U_g gas velocity [m/s]

$\overline{U}_g$ gas velocity vector [m/s]

U_{gy0} initial y-component of gas velocity [m/s]

U_s solid velocity [m/s]

$\overline{U}_s$ solid velocity vector [m/s]

$\langle U_{sy} \rangle$ time averaged y-component of solid velocity [cm/s]

U_{sy0} initial solid velocity [m/s]

x coordinate direction [m]

x^* wall function parameter [−]

Δx width of computational cell next to wall [m]

Δy height of computational cell next to wall [m]

z independent variable used in Eqs. 1 and 2 [−]

Greek Symbols

β drag coefficient [kg/(s·m^3)]

ε_g^* packed bed void fraction [−]

ε_g gas void fraction [−]

$\langle \varepsilon_g \rangle$ time averaged void fraction [−]

ε_g^t turbulent energy dissipation in the gas phase [m^2/s^3]

ε_s solid volume fraction [−]

$\varepsilon_{s,max}$ maximum solid volume fraction [−]

ε_s^t dissipation of solid fluctuating energy due to inter-particle collisions [J/(m^3·s)]

η function of restitution coefficient [−]

θ_n shift parameter determined in Step 4 [−]

Θ granular temperature [m^2/s^2]

κ_s conductivity of solids turbulent energy [m^2/s]

κ_s^t granular conductivity [J/(m·K·s)]

λ second coefficient of solids viscosity [kg/(m·s)]

μ_n location parameter determined in Step 2 [−]

μ_g gas viscosity [kg/(m·s)]

μ_g^t turbulent eddy viscosity [kg/(s·m)]

μ_s solids viscosity [kg/(s·m)]

Π_{kg} gas phase turbulence exchange term [kg/(m·s^3)]

Π_{ks} solid phase turbulence exchange term [kg/(m·s^3)]

ρ_g gas density [kg/m^3]

ρ_s particle density [kg/m^3]

σ_n shape parameter determined in Step 3 [−]

τ_g gas phase stress tensor [kPa]

τ_g^t energetic turbulence eddy time scale [s]

τ_L^x particle relaxation time scale [s]

τ_s solid phase stress tensor [kPa]

ϕ angle of internal friction [−]

ϕ_w angle of internal friction at walls [−]

Chapter 5: Future Work

Uncertainty analysis is a tool that has applications across disciplines. The tools and techniques presented here could easily be applied elsewhere. Future work for both uncertainty analysis contributions clearly includes an exploration into other adsorption scenarios as well as other uncertain scenarios.

In addition to expanding the breadth of application of the multiscale uncertainty analysis, there is work to be done in reducing the computational burden of the stochastic molecular-level modeling. For the molecular results alone from Chapter 3, months of computational time were necessary. And QUICKER is of limited use in reducing this effort: QUICKER will reduce the effort for scenarios with large numbers of uncertain inputs, but these molecular scenarios had only a single uncertain input. Future work should include the development of a methodology analogous to QUICKER, but focused on reducing the computational burden of scenarios with only a single uncertain input parameter.

For the field of uncertainty quantification, in addition to analyzing the effects of how input uncertainty propagates through a system, it is also of interest to determine the sensitivity of outputs to each input parameter. Currently, QUICKER is focused exclusively on input uncertainty propagation, and extending it into sensitivity analysis would greatly improve its usability.

Bibliography

[1] F. Sefidvash, January 2012. [Online]. Available: http://www.sefidvash.net/fbnr/.

[2] A. Malek and S. Farooq, "Determination of Equilibrium Isotherms Using Dynamic Column Breakthrough and Constant Flow Equilibrium Desorption," *Journal of Chemical and Engineering Data,* no. 41, pp. 25-32, 1996.

[3] M. F. Edwards and J. F. Richardson, "Gas Dispersion in Packed Beds," *Chemical Engineering Science,* no. 23, pp. 109-123, 1968.

[4] L. Bastin, P. S. Barcia, E. J. Hurtado, J. A. C. Silva, A. E. Rodrigues and B. Chen, "A Microporous Metal-Organic Framework for Separation of CO2/N2 and CO2/CH4 by Fixed-Bed Adsorption," *Journal of Physical Chemistry C,* pp. 1575-1581, 2008.

[5] S. Cavenati, C. A. Grande and A. E. Rodrigues, "Layerd Pressure Swing Adsorption for Methane Recovery from CH4/CO2/N2 Streams," *Adsorption 11,* pp. 549-554, 2005.

[6] M. J. Ahmed, A. H. A. K. Mohammed and A. A. H. Kadhum, "Modeling of Breakthrough Curves for Adsorption of Propane, n-Butane, and Iso-Butane Mixture on 5A Molecular Sieve Zeolite," *Transport in Porous Media,* 2010.

[7] H. Järvelin and J. R. Fair, "Adsorptive Separation of Propylene-Propane Mixtures," *Industrial Engineering and Chemical Research,* pp. 2201-2207, 1993.

[8] J. D. Pesanksy, N. A. Majiros, C. M. Sorensen and D. L. Thomas, "The Effect of Three-way Catalyst Selection on Component Pressure Drop and System Performance," *SAE International,* 2009.

[9] F. A. Da Silva, J. A. Silva and A. E. Rodrigues, "A General Package for the Simulation of Cyclic Adsorption Processes," *Adsorption 5,* pp. 229-244, 1999.

[10] S. P. Knaebel, D. Ko and L. T. Biegler, "Simulation and Optimization of a Pressure Swing Adsorption System: Recovering Hydrogen from Methane," *Adsorption,* pp. 615-620, 2005.

[11] S. Cavenati, C. A. Grande and A. E. Rodrigues, "Separation of CH4/CO2/N2 mixtures by layered pressure swing adsorption for upgrade of natural gas," *Chemical Engineering Science 61,* pp. 3893-3906, 2006.

[12] X. Zheng, Y. Liu and W. Liu, "Two-Dimensional Modeling of the Transport Phenomena in the Adsorber During Pressure Swing Adsorption Process," *Industrial and Engineering Chemistry Research,* no. 49, pp. 11814-11824, 2010.

[13] T. Aida and P. L. Silveston, Cyclic Separating Reactors, Ames: Blackwell Publishing Ltd., 2005.

[14] D. M. Ruthven, S. Farooq and K. S. Knaebel, Pressure Swing Adsorption, New York: VCH Publishers, Inc., 1994.

[15] C. Tien, Adsorption Calculations and Modeling, Boston: Butterworth-Heinemann, 1994.

[16] A. A. Kareeri, H. D. Zughbi and H. H. Al-Ali, "Simulation of Flow Distribution in Radial Flow Reactors," *Industrial and Engineering Chemical Research,* no. 45, pp. 2862-2874, 2006.

[17] P. J. Heggs, D. I. Ellis and M. S. Ismail, "Prediction of flow distributions and pressure changes in multi-layered annular packed beds," *Gas Separation and Purification,* vol. 9, no. 4, pp. 243-252, 1995.

[18] R. Li and Z. Zhu, "Investigations on hydrodynamics of multilayer Pi-Type radial flow reactors," *Asia-Pacific Journal of Chemical Engineering,* 2011.

[19] A. K. Singh, "Modeling of Radial Flow Dynamics for Fixed Bed Reactor," 2005.

[20] R. W. Fahien and J. M. Smith, "Mass Transfer in Packed Beds," *American Institute of Chemical Engineering Journal,* pp. 328-337, 1955.

[21] H. Järvelin, "Adsorption of Propane and Propylene," 1990.

[22] P. Demontis and G. B. Suffritti, "Structure and Dynamics of Zeolites Investigated by Molecular Dynamics," *Chemical Reviews,* pp. 2845-2878, 1997.

[23] B. Smit and T. L. M. Maesen, "Molecular Simulations of Zeolites: Adsorption, Diffusion, and Shape Selectivity," *Chemical Reviews,* pp. 4125-4184, 2008.

[24] E. Garcia-Perez, D. Dubbeldam, B. Liu, B. Smit and S. Calero, "A Computational Method to Characterize Framework Aluminum in Aluminosilicates," *Angewandte Chemie International Edition,* pp. 280-282, 2007.

[25] B. Liu, E. Garcia-Perez, D. Dubbeldam, B. Smit and S. Calero, "Understanding Aluminum Location and Non-framework Ions Effects on Alkane Adsorption in Aluminosilicates: A Molecular Simulation Study," *Journal of Physical Chemistry,* pp. 10419-10426, 2007.

[26] L. B. McCusker and C. Baerlocher, "Solving Complex Zeolite Structures--How Far Can We Go?," *Studies in Surface Science and Catalysis,* pp. 3-12, 2008.

[27] R. E. Morris and P. S. Wheatley, "Diffraction Techniques Applied to Zeolites," *Studies in Surface Science and Catalysis,* pp. 375-401, 2007.

[28] R. J. Accardi and R. F. Lobo, "Accessibility of Litium Cations in High-silica Zeolites Investigated Using the NMR Paramagnetic Shift Effect of Adsorbed Oxygen," *Microporous and Mesoporous Materials,* pp. 25-34, 2000.

[29] E. Yildirim and R. Dupree, "Investigation of Al-O-Al Sites in an Na-aluminosilicate Glass," *Bulletin of Material Science,* pp. 269-272, 2004.

[30] S. M. Auerbach, L. M. Bull, N. J. Henson, H. I. Metiu and A. K. Cheetham, "Behavior of Benzene in Na-X and Na-Y Zeolites: Comparative Study by 2H NMR and Molecular Mechanics," *Journal of Physical Chemistry,* pp. 5923-5930, 1996.

[31] S. Buttefey, A. Boutin, C. Mellot-Dranicks and A. H. Fuchs, "Simple Model for Predicting the Na+ Distribution in Anhydrous NaY and NaX Zeolites," *Journal of Physical Chemistry,* pp. 9569-9575, 2001.

[32] E. Jaramillo and S. M. Auerbach, "New Force Field for Na Cations in Faujasite-Type Zeolites," *Journal of Physical Chemistry,* pp. 9589-9594, 1999.

[33] S. Calero, D. Dubbeldam, R. Krishna, B. Smit, T. J. H. Vlugt, J. F. M. Denayer, J. A. Martens and T. L. M. Maesen, "Understanding the Role of Sodium during Adsorption: A Force Field for Alkanes in Sodium-Exchanged Faujasites," *Journal of the American Chemical Society,* pp. 11377-11386, 2004.

[34] R. W. Broach, "Zeolite Types and Structures," in *Zeolites in Industrial Separation and Catalysis*, Wiley-VCH, 2010, pp. 27-59.

[35] D. Frenkel and B. Smit, Understanding Molecular Simulation from Algorithms to Applications, New York: Academic Press, 2002.

[36] A. Z. Panagiotopoulos, "Adsorption and Capillary Condensation of Fluids in Cylindrical Pores by Monte Carlo Simulation in the Gibbs Ensemble," *Molecular Physics,* vol. 62, no. 3, pp. 701-719, 1987.

[37] V. Lachet, A. Boutin, B. Tavitian and A. H. Fuchs, "Grand Canonical Monte Carlo Simulations of Adsorption of Mixtures of Xylene Molecules in Faujasite Zeolites," *Faraday Discussions,* pp. 307-323, 1997.

[38] M. G. Martin, B. Chen, C. D. Wick, J. J. Potoff, J. M. Stubbs and J. I. Siepmann, *MCCCS Towhee.*

[39] R. M. Barrer and P. J. Cram, "Heats of Immersion of Outgassed Ion-Exchanged Zeolites," in *Molecular Sieve Zeolites II*, American Chemical Society, 1971, pp. 105-131.

[40] H. W. Habgood, "Adsorptive and Gas Chromatographic Properties of Various Cationic Forms of Zeolite X," *Canadian Journal of Chemistry,* pp. 2340-2350, 1964.

[41] G. V. Tsitsishvili and T. G. Andronikashvili, "Intermolecular Interactions in Gaschromatographic Separations on Zeolites," *Journal of Chromatography,* pp. 39-45, 1971.

[42] R. J. Neddenriep, "Sodium Cation Adsorption Sites in Zeolite Types X and Y," *Journal of Colloid and Interface Science,* pp. 293-304, 1968.

[43] E. V. Chkhaidze, A. A. Fomkin, V. V. Serpinskii and G. V. Tsitsishvili, "Adsorption of Methane on NaX Zeolite in the Subcritical and Supercritical Regions," *Russian Chemical Bulletin,* pp. 886-890, 1985.

[44] T. F. Ding, S. Ozawa, T. Yamazaki, I. Watanuki and Y. Ogino, "A Generalized Treatment of Adsorption of Methane onto Various Zeolites," *Langmuir,* pp. 392-396, 1988.

[45] K. F. Loughlin, M. A. Hasanain and H. B. Abdul-Reham, "Quaternary, Ternary, Binary, and Pure Component Sorption on Zeolites. 2. Light Alkanes on Linde 5A and 13X Zeolites at Moderate to High Pressure," *Industrial and Engineering Chemistry Research,* pp. 1535-1546, 1990.

[46] L. G. Shekhovtsova and A. A. Fomkin, "Discrete Site Model for Methane Adsorption on Microporous Adsorbents," *Russian Chemical Bulletin,* pp. 867-870, 1990.

[47] S. Y. Zhang, O. Talu and D. T. Hayhurst, "High-pressure Adsorption of Methane in Zeolites NaX, MgX, CaX, SrX, and BaX," *Journal of Physical Chemistry,* pp. 1722-1726, 1991.

[48] V. R. Choudhary, S. Mayadevi and A. P. Singh, "Simple Aparatus for the Gravimetric Adsorption of Liquid Vapors on Solid Catalysts/Adsorbents," *Industrial and Engineering Chemistry Research,* pp. 413-415, 1995.

[49] R. W. Triebe, F. H. Tezel and K. C. Khulbe, "Adsorption of Methane, Ethane and Ethylene on Molecular Sieve Zeolites," *Gas Separation and Purification,* pp. 81-84, 1996.

[50] J. A. Dunne, M. Rao, S. Sircar, R. J. Gorte and A. L. Myers, "Calorimetric Heats of Adsorption and Adsorption Isotherms. 2. O2, N2, Ar, CO2, CH4, C2H6, and SF6 on NaX, H-ZSM-5, and Na-ZSM-5 Zeolites," *Langmuir,* pp. 5896-5904, 1996.

[51] S. Cavenati, C. A. Grande and A. E. Rodrigues, "Adsorption Equilibrium of Methane, Carbon Dioxide, and Nitrogen on Zeolite 13X at High Pressures," *Journal of Chemical and Engineering Data,* pp. 1095-1101, 2004.

[52] M. Llano-Restrepo, "Accurate Correlation, Structural Interpretation, and Thermochemistry of Equilibrium Adsorption Isotherms of Carbon Dioxide in Zeolite NaX by Means of the GSTA Model," *Fluid Phase Equilibria,* pp. 225-236, 2010.

[53] M. Tarek, R. Kahn and E. C. de Lara, "Modelization of Experimental Isotherms of n-Alkanes in NaX Zeolite," *Zeolites,* pp. 67-72, 1995.

[54] O. M. Dzhigit, A. V. Kiselev and T. A. Rachmanova, "Henry's Constants, Isotherms and Heats of Adsorption of Some Hydrocarbons in Zeolites of Faujasite Type with Different Content of Sodium Cations," *Zeolites,* pp. 389-397, 1984.

[55] F. A. Da Silva and A. E. Rodrigues, "Adsorption Equilibria and Kinetics for Propylene and Propane Over 13X and 4A Zeolite Pellets," *Industrial and Engineering Chemistry Research,* pp. 2051-2057, 1999.

[56] M. C. Campo, A. M. Ribeiro, A. Ferreira, J. C. Santos, C. Lutz, J. M. Loureiro and A. E. Rodrigues, "New 13X Zeolite for Propylene/Propane Separation by Vacuum Swing Adsorption," *Separation and Purification Technology,* pp. 60-70, 2013.

[57] A. van Miltenburg, J. Gascon, W. Zhu, F. Kapteijn and J. A. Moulijn, "Propylene/Propane Mixture Adsorption on Faujasite Sorbents," *Adsorption,* pp. 309-321, 2008.

[58] F. R. Siperstein and A. L. Myers, "Mixed-Gas Adsorption," *AIChE Journal,* pp. 1141-1159, 2001.

[59] R. M. Barrer and J. W. Sutherland, "Inclusion Complexes of Faujasite with Paraffins and Permanent Gases," *Proceedings of the Royal Society A,* vol. 237, no. 1211, pp. 439-463, 1956.

[60] C. J. Roy and W. L. Oberkampf, "A Complete Framework for Verification, Validation, and Uncertainty Quantification in Scientific Computing," American Institute of Aeronautics and Astronautics, Orlando, 2010.

[61] A. Mawardi and R. Pitchumani, "SAMS: Stochastic Analysis With Minimal Sampling--A Fast Algorithm for Analysis and Design Under Uncertainty," *Journal of Mechanical Design,* vol. 127, pp. 558-571, 2005.

[62] H.-R. Bae, R. V. Grandhi and R. A. Canfield, "An Approximation Approach for Uncertainty Quantification Using Evidence Theory," *Reliability Engineering and System Safety,* vol. 86, pp. 215-225, 2004.

[63] B. DeVolder, J. Glimm, J. W. Grove, Y. Kang, Y. Lee, K. Pao, D. H. Sharp and K. Ye, "Uncertainty Quantification for Multiscale Simulations," *Journal of Fluids Engineering,* vol. 124, pp. 29-41, 2002.

[64] H.-R. Bae, R. V. Grandhi and R. A. Canfield, "Epistemic Uncertainty Quantification Techniques Including Evidence Theory for Large-Scale Structures," *Computers and Structures,* no. 82, pp. 1101-1112, 2004.

[65] H. Agarwal, J. E. Renaud, E. L. Preston and D. Padmanabhan, "Uncertainty quantification using evidence theory in multidisciplinary design optimization," *Reliability Engineering and System Safety,* vol. 85, pp. 281-294, 2004.

[66] C. J. Sallaberry, J. C. Helton and S. C. Hora, "Extension of Latin Hypercube Samples with Correlated Variables," Sandia National Laboratories, Albuquerque, 2006.

[67] J. C. Helton and F. J. Davis, "Latin hypercube sampling and the propagation of uncertainty in analyses of complex systems," *Reliability Engineering and System Safety,* no. 81, pp. 23-69, 2003.

[68] B. M. Adams, W. J. Bohnoff, K. R. Dalbey, J. P. Eddy, M. S. Eldred, D. M. Gay, K. Haskell, P. D. Hough and L. P. Swiler, "DAKOTA, A Multilevel Parallel Object-Oriented Framework for Design Optimization, Parameter Estimation, Uncertainty Quantification, and Sensitivity Analysis: Version 5.0 User's Manual," Sandia National Laboratory, Albuquerque, 2011.

[69] L. P. Swiler and G. D. Wyss, "A User's Guide to Sandia's Latin Hypercube Sampling Software: LHS UNIX Library/Standalone Version," Sandia National Laboratories, Albuquerque, 2004.

[70] S. F. Wojtkiewicz, M. S. Eldred, R. V. Field, A. Urbina and J. R. Red-Horse, "Uncertainty Quantification In Large Computational Engineering Models," in *AIAA-2001*, Albuquerque, 2001.

[71] L. P. Swiler, R. Slepoy and A. A. Giunta, "Evaluation of Sampling Methods in Constructing Response," Sandia National Laboratories, Albuquerque, 2006.

[72] V. J. Romero, J. V. Burkardt, M. D. Gunzburger and J. S. Peterson, "Comparison of pure and ''Latinized'' centroidal Voronoi tessellation," *Reliability Engineering and System Safety,* vol. 91, pp. 1266-1280, 2006.

[73] R. E. Caflisch, "Monte Carlo and quasi-Monte Carlo methods," in *Acta Numerica*, Cambridge, Cambridge University Press, 1998, pp. 1-49.

[74] G. G. Wang and S. Shan, "Review of Metamodeling Techniques in Support of Engineering Design Optimization," *Journal of Mechanical Design,* vol. 129, pp. 370-380, 2007.

[75] C. B. Storlie, L. P. Swiler, J. C. Helton and C. J. Sallaberry, "Implementation and Evaluation of Nonparametric Regression Procedures for Sensitivity Analysis of Computationally Demanding Models," *Reliability Engineering and System Safety,* vol. 94, no. 11, pp. 1735-1763, 2009.

[76] T. W. Simpson, J. D. Peplinski and J. K. Allen, "Metamodels for Computer-based Engineering Design: Survey and Recommendations," *Engineering with Computers,* pp. 129-150, 2001.

[77] L. Wang, D. Beeson, G. Wiggs and M. Rayasam, "A Comparison of Meta-modeling Methods Using Practical Industry Requirements," in *Structures, Structural Dyanmics, and Materials Conference*, Newport, 2006.

[78] J. H. Friedman, "Multivariate Adaptive Regression Splines," *The Annals of Statistics,* vol. 19, no. 1, pp. 1-141, 1991.

[79] M. Papadrakakis, N. D. Lagaros and Y. Tsompanakis, "Structural Optimization Using Evolution Strategies and Neural Networks," *Computer Methods in Applied Mechanics and Engineering*, no. 156, pp. 309-333, 1998.

[80] S. Varadarajan, W. Chen and C. J. Pelka, "Robust Concept Exploration of Propulsion Systems with Enhanced Model Approximation Capabilities," *Engineering Optimization,* vol. 32, no. 3, pp. 309-334, 2000.

[81] C. E. Rasmussen and C. K. I. Williams, Gaussian Processes for Machine Learning, Cambridge: MIT Press, 2006.

[82] D. Barber, Bayesian Reasoning and Machine Learning, Cambridge University Press, 2013.

[83] R. Kohavi, "A study of cross-validation and bootstrap for accuracy estimation and model selection," in *IJCAI'95 Proceedings of the 14th international joint conference on Artificial intelligence*, San Francisco, 1995.

[84] P. Krizek, J. Kittler and V. Hlavac, "Improving Stability of Feature Selection Methods," in *CAIP'07 Proceedings of the 12th international conference on Computer analysis of images and patterns*, Berlin, 2007.

[85] T. W. Anderson and D. A. Darling, "Asymptotic Theory of Certain "Goodness of Fit" Criteria Based on Stochastic Processes," *Institute of Mathematical Statistics,* vol. 23, no. 2, pp. 193-212, 1952.

[86] A. Gel, T. Li, B. Gopalan, M. Shahnam and M. Syamlal, "Validation and Uncertainty Quantification of a Multiphase Computational Fluid Dynamics Model," *Industrial and Engineering Chemistry Research,* 2013.

[87] G. Taguchi, System of Experimental Design, White Plains: Quality Resources, 1991.

[88] N. Balakrishnan and W. S. Chen, Handbook of Tables for Order Statistics from Lognormal Distributions with Applications, Norwell: Kluwer Academic Publishers, 1999.

[89] M. Syamlal, W. Rogers and T. O'Brien, "MFIX Documentation Theory Guide," U.S. Department of Energy Office of Fossil Energy, Morgantown, 1993.

[90] M. Syamlal, "MFIX Documentation Numerical Technique," Department of Energy, Morgantown, 1998.

[91] J. Cao and G. Ahmadi, "Gas-particle two-phase turbulent flow in a vertical duct," *International Journal of Multiphase Flow,* vol. 21, no. 6, pp. 1203-1228, 1995.

[92] J. T. Jenkins and M. Y. Louge, "On the Flux of Fluctuating Energy in a Collisional Grain Flow at a Flat Frictional Wall," *Physics of Fluids,* vol. 9, no. 10, pp. 2835-2840, 1997.

[93] R. Jin, W. Chen and T. W. Simpson, "Comparative studies of metamodelling techniques under multiple modelling criteria," *Structural and Multidisciplinary Optimization,* vol. 23, no. 1, pp. 1-13, 2001.